NONR 4222 (01)
ARPA ORDER #125, AMEND #8

AD644814

TECHNICAL REPORT # 20

TO

ADVANCED RESEARCH PROJECTS AGENCY

SPECTRAL ANALYSIS OF MECHANISMS AND KINETICS OF THERMAL ENERGY REACTIONS OF LONG-LIVED ENERGETIC HELIUM SPECIES WITH SIMPLE MOLECULES

Principal Investigator: H. P. Broida

University of California
Santa Barbara
Physics Department

DDC
1966

CLEARINGHOUSE
FOR FEDERAL SCIENTIFIC AND TECHNICAL INFORMATION

Hardcopy	Microfiche		
$3.00	$ .65	153 pp	as

ARCHIVE COPY

December 1, 1966

Reproduction In Whole Or In Part Is Permitted
For Any Purpose Of The United States Government

BEST
AVAILABLE COPY

UNIVERSITY OF CALIFORNIA
Santa Barbara

SPECTRAL ANALYSIS OF MECHANISMS AND KINETICS OF THERMAL ENERGY REACTIONS OF LONG-LIVED ENERGETIC HELIUM SPECIES WITH SIMPLE MOLECULES

A Dissertation submitted in partial satisfaction
of the requirements for the degree of

Doctor of Philosophy

in

Chemical Physics

by

Jerry L. Dunn

Committee in charge:

Professor Herbert P. Broida, Chairman
Professor Clifford A. Hopson
Associate Professor Jorge R. Fontana
Associate Professor Glyn O. Pritchard
Assistant Professor Henry W. Offen

November 1966

ACKNOWLEDGEMENTS

It is my pleasure to acknowledge the assistance of several individuals during the development of the present work. I would particularly like to thank my thesis advisor, Professor H. P. Broida, for his guidance, financial support, and seemingly endless encouragement in all phases of my education. The assistance of Professors G. O. Pritchard, H. W. Offen, and B. F. Rickborn in directing my acedemic program is greatly appreciated.

The assistance of J. A. Bartley and H. Nickel in constructing and maintaining the experimental apparatus was invaluable. I would like to thank Mrs. L. Hoadley and Mrs. H. B. M. Keynes for their help in preparing this manuscript.

I would particularly like to indicate the debt of gratitude to my wife, Geraldine, for her encouragement, patience, and faith throughout the years of graduate school.

The financial support of the General Motors Corporation, Advanced Research Projects Agency, and the Office of Naval Research is gratefully acknowledged.

ABSTRACT

Spectral Analysis of Mechanisms and Kinetics of Thermal Energy Reactions of Long-Lived Energetic Helium Species with Simple Molecules

by

Jerry L. Dunn

Low energy inelastic collision processes have been studied in a flowing steady state helium afterglow. Rate coefficients for thermal energy reactions of Ar, Kr, N_2, O_2, H_2, NO, CO, and CO_2 reactants with long-lived energetic helium species have been measured. The (2^3S) metastable atom, He^m, the ($a^3\Sigma$) metastable molecule, He_2^m, the ground state atomic ion, He^+, and the ground state molecular ion, He_2^+, were the helium reactants. An optical spectroscopic technique for determining rate coefficients has been developed and utilized for measuring the decrease in energetic helium as a function of added reactant concentration. Relative concentration measurements of the helium species were made by introducing a "second reactant" to the afterglow and monitoring relative intensities of the resulting spectra. Individual reactions involving single helium species were studied by observing transitions of the second reactant whose upper states were preferentially excited

by the energetic helium species to be measured. Rate coefficients were limited to the range of 10^{-9} to 10^{-13} cm^3 sec^{-1}. Penning ionization reactions with He^m and ion-neutral reactions with He^+ have been compared to published values. Overall agreement of the rates reported in these experiments and published values measured by optical absorption and mass spectrometric techniques gives confidence in the general method.

In addition, nitrogen spectra selectively excited in a helium afterglow were studied in order to understand details of the excitation processes. Photographic spectra of the nitrogen emission in the 2300 to 8700Å wavelength region contained band systems originating in the A $^2\Pi$, B $^2\Sigma$, and D $^2\Pi$ electronic states of N_2^+, the C $^3\Pi$, and B $^3\Pi$ states of N_2, and atomic nitrogen lines. Distributions of population over the rotational and vibrational levels of the excited electronic states were obtained by measuring relative intensities of the resulting transitions. Relative changes in population distributions were observed for a variety of experimental conditions designed to change concentrations of the energetic helium species relative to one another. A low power microwave field applied to the afterglow removed atomic and molecular helium ions by ambipolar diffusion loss to the walls. Hydrogen added to the afterglow preferentially removed He^m since its rate of reaction with He^m is significantly larger than with the other

energetic helium species. Correlations of the observed excited states of nitrogen with the energetic helium species were made by using Franck's resonance rule, Massey's adiabatic hypothesis, and the Franck-Condon principle for excitation from the ground state. Mechanisms for reactions of He_2^+ and He_2^m with N_2 are discussed in terms of the available energy of the molecule which undergoes dissociation upon reacting. The observed pressure dependence for intensities of the perturbed rotational levels in the (1,0) band of the $B\ ^2\Sigma$ - $X\ ^2\Sigma$ first negative system is discussed in terms of the excited state populations and subsequent collisional energy transfer.

TABLE OF CONTENTS

Chapter

I. INTRODUCTION 1

1.1 Properties and Origin of the Afterglow in Pure Helium 2
1.2 Impurity Spectra Excited in a Helium Afterglow 6
1.3 Reaction Kinetics in a Flowing Steady State Afterglow 9
1.4 Description of Present Experiments 11

II. EXPERIMENTAL APPARATUS AND TECHNIQUE 18

2.1 General Description 18
2.2 Gas Flow Apparatus and Technique 24
2.3 Spectroscopic Apparatus and Technique 31
2.4 Helium Purity 34

III. ANALYSIS OF THE NITROGEN SPECTRUM 45

3.1 Photographic Spectra for Helium and Helium-Nitrogen Afterglow Emissions from 2300 to 8700A 46
3.2 Rotational Structure of (0,0) and (1,0) Bands of the B $^2\Sigma$ - X $^2\Sigma$ First Negative Transition in N_2^+. 50
3.3 Vibrational Population Distribution in the N_2^+ Emission Spectra 57
3.4 Summary and Model for Excitation of N_2 by Energetic Helium 60

IV. REACTION KINETICS OF EXCITED STATES 91

4.1 General Rate Equations 91
4.2 Reactions Involving Energetic Helium and Nitrogen 102
4.3 General Method for Energetic Helium-Reactant Reactions 107

V. EXPERIMENTAL RATE COEFFICIENTS 117

5.1 Reactions with He^m 120
5.2 Reactions with He^+ 124
5.3 Reactions with He_2^+ 125
5.4 Reactions with He_2^m 126

I. INTRODUCTION

During the last two decades theoretical and experimental studies in atomic collision processes have been stimulated by interest in such fields as gas scintillation counters, aeronomy of the upper atmosphere, astrophysics, radiation damage, reentry physics, controlled thermonuclear fusion, and gas lasers. Inelastic collisions involving electrons, ions, excited atoms and molecules at near-thermal energies make up an area of particular interest to spectroscopists studying atomic and molecular structure as well as the kinetics of collision processes and chemical reactions. Gas discharges, afterglows, shock tubes, flames, and molecular beams are but some of accessible laboratory techniques. The following effort has been dedicated to the investigation of inelastic collision processes occurring in a helium afterglow. This is, essentially, the study of excited helium in the time following the removal of the electrical source of excitation. This particular method lends itself to studies of thermal-energy collisions since the electrons, ions, and excited species have been allowed to relax to a kinetic temperature near to that of the ambient gas (~300°K corresponding to an average energy of 0.04 eV.) before the measurements are performed.

1.1 Properties and Origin of the Afterglow in Pure Helium

A considerable number of studies of atomic and molecular collision processes occurring in afterglows of discharges through helium have been reported in the literature. Various methods have been used to study properties of this afterglow determined by the thermal-energy collision processes to be investigated. The principle experimental techniques include[1]: (1) Langmuir probes; (2) radio and microwave frequency methods; (3) mass spectroscopy; (4) optical absorption; and (5) emission spectroscopy and interferometry.

Langmuir probes have been used to measure electron and ion densities as well as mean electron energies in afterglows and plasmas[2]. Numerous problems have been encountered in the interpretation of experimental probe data and considerable work is required to obtain meaningful measurements.

A microwave probing technique has been developed by Biondi and Brown[3] to measure the spatially averaged electron densities in the afterglow. Resonant frequency shifts of a microwave cavity caused by presence of an afterglow are interpreted in terms of a complex dielectric constant of the ionized gas from which the average electron density and electron collision frequency can be calculated. Because the microwave signal is sufficiently weak not to disturb the electron energy, this method has found wide use in determining the removal processes of free electrons in the afterglow.

Mass spectroscopy recently has become one of the most important methods used in the identification and concentration measurements of the ion species in the afterglow[5,6]. The differentially pumped radio-frequency mass spectrometer has sufficiently fast response to follow ion decay as a function of time[6]. Analysis of ion products and intermediates of charge transfer and other ionization reactions gives quantitative information concerning the mechanism and paths of the reactions studied.

Afterglow optical absorption method refers specifically to the detection and concentration measurements of metastable and in some cases ground state species[7]. Fractional absorption of external radiation traversing the afterglow region by metastable atoms or molecules raising them to higher radiating states can be interpreted in terms of a concentration of the absorbing species.

Emission spectroscopic and interferometric techniques refer to the considerable amount of information available from an analysis of optical radiation emitted from afterglows[8]. Intensities of atomic and molecular radiation can be interpreted in terms of relative concentrations of emitting species. The time development and decay of excited state populations can be generally analyzed in connection with other afterglow measurements such as electron, ion, and metastable concentrations to determine the histories of the species and their decay and formation rates. The kinetic energy of radiating species can be calculated from the observed widths of the Doppler broadened emission lines[9]. In ionized gases in which

the radiating species are subject to strong electric fields, the emission line profiles are broadened by the Stark effect from which information about the electron density can be obtained[10]. High resolution measurements of the line profiles are generally made with Fabry-Perot interferometers.

As each method yields measurements of the afterglow parameters, the investigation of a particular atomic or molecular collision process generally requires a selected combination of various techniques. Recently, Mosburg[11] determined the helium atomic ion-electron recombination coefficient as a function of electron density and temperature by applying several of the previously mentioned techniques to study the afterglow in helium. Measurements of the atomic line intensities and their project brightness profiles, the electron density and temperature, and the optical absorption by metastables were made as a function of time after cessation of the discharge.

In afterglows of an electrical discharge thru helium, the problems of the origin of atomic and molecular emissions and their relation to electron-ion recombination processes have received a considerable amount of attention in the literature. Early measurements of the electron-ion recombination coefficient were made by observing the decay of electron density as a function of time by the microwave cavity method[3,4,12]. These results were complicated by failure to take into account the electron decay due to diffusion in higher order modes[13]. It was the opinion of several investigators[12,14] that only the experiment of Chen, Leiby, and Goldstein[4] had produced an afterglow which was recombination controlled.

Until recently the observed decay of electron density in the helium afterglow was interpreted to proceed primarily by dissociative recombination of He_2^+ [12]. Development of the theory of collisional-radiative recombination by Bates, Kingston, and McWhirter[15] suggests a collisional radiative mechanism for the electron-ion recombination process. Moreover, the newly revised molecular helium potential curves by Mulliken[16] predict small rate constants for the dissociative-recombination reaction except in the case where the molecular helium is vibrationally excited. The mechanism of collisional-radiative recombination has the form of a three-body reaction where the third body is usually an electron which can absorb the energy defect of the reaction as kinetic energy, i.e.

$$He^+ + e + e \rightarrow He^* + e \qquad (1.1)$$

and

$$He_2^+ + e + e \rightarrow He_2^* + e \qquad (1.2)$$

where He^* and He_2^* represent the excited upper states of the transitions producing the afterglow emission.

Results obtained from spectroscopic studies of the helium afterglow occurring in a flow system have been interpreted to support the collisional-radiative recombination mechanism[17]. Hinnov and Hirschberg[18] who investigated the recombination rate and characteristics of the atomic emission in a magnetically confined afterglow of the B-1 stellarator discharge, attributed the atomic emission to a three-body recombination process of the type (1.1). The critical investigation by Mosburg[11] of the time dependence of atomic and

molecular emission intensities, electron density and temperature, and metastable helium density gives values for the atomic ion-electron recombination coefficient in reasonable agreement with collisional-radiative recombination theory. Recently, Gerber, Sauter, and Oskam[19] made simultaneous optical and mass spectroscopic measurements of the atomic and molecular radiation and of the corresponding ion densities as a function of time after the discharge. Analysis of the two sets of measurements strongly indicate that the three-body reactions predicted by the collisional radiative recombination theory are responsible for the observed results. Ferguson, Fehsenfeld, and Schmeltekopf[14] give a comprehensive discussion of the new theoretical developments as well as experimental measurements associated with the molecular helium ion-electron recombination problem.

1.2 Impurity Spectra Excited in a Helium Afterglow

An electric discharge maintained through a mixture of rare gas with trace quantities of a second gas has been used by spectroscopists for many years as a source of radiation of the trace gas. This source has proved to be useful as a method to study normally occurring weak band systems or those strongly overlapped in discharges through the pure gas[20].

Early investigations of the selective-excitation of impurities in helium discharges were carried out by Duffendack and Smith[21], Takahashi[22], Richardson[23], and others[24]. The resulting spectra

were first attributed to inelastic collisions with the helium atomic ion and metastable atoms in the 2^1S and 2^3S states. There was a considerable amount of difficulty in interpreting the selectively-excited spectra in terms of energy conservation and Franck's resonance rule applied to collisions of the second kind with the predicted energetic helium species. Meyerott[25] surveyed the literature on spectra excited in a helium discharge and suggested inelastic collisions with molecular helium ions and metastable molecules in the $a^3\Sigma$ state to be responsible for the discrepancies observed in the resulting spectra. Moreover, he deduced energies of the metastable molecule and molecular ion from levels of the observed spectrum. Meyerott's calculated values for repulsive energy of the ground state molecule upon deexcitation of the metastable molecule and ion suffered from uncertainties in the known helium molecular energies. A definite correlation of the selectively-excited spectra with energetic helium species was undoubtedly complicated by appearance of emission spectra excited by collisions with high energy electrons in the discharge.

Herman, Felenbok, and Herman[26] investigated population distributions over vibrational levels of the $B^2\Sigma$ state of N_2^+ excited in the afterglow of a helium-nitrogen discharge. The distribution was compared to that observed for excitation of CO by inelastic collisions with metastable Xe[27]. The effect of energy resonance on population distributions was found to be much sharper for collisions without ionization.

To avoid many difficulties in interpreting selectively-excited spectra occurring in a discharge, Collins and Robertson[28] investigated excitation of several gases added to a flowing, steady state helium afterglow. Excitation of the added gases was attributed exclusively to collisions of the second kind with energetic helium species normally occurring in the afterglow. Excitation by collisions with high energy electrons common to discharges was considered negligible due to low electron temperatures present in the afterglow[29]. A study of excitation processes responsible for the impurity spectra was presented in which a correlation of the excited levels with energetic helium species was made. Several techniques were developed which produced afterglow conditions favoring an individual excitation mechanism. The relative occurrence of reactions involving $He(2^3S)$ or He^m, He^+, and He_2^+ was found to depend on downstream pressure. A microwave field applied to the afterglow quenched ion reactions relative to the metastable. A third difference in the observed spectra was the rate of decay of energetic species as a function of time or axial distance downstream from the discharge.

Recently, Robertson[30] analyzed the distributions of population over the vibrational levels of the $A^2\Pi$ - $X^2\Pi$ and $b^4\Sigma$ - $a^4\Pi$ systems of O_2^+ and the $B^2\Sigma$ - $X^2\Sigma$ system of N_2^+ selectively excited in a helium afterglow. For each band system studied, no enhancement of population was observed for those levels of close energy resonance with the exciting species but the population distributions approximately

followed that predicted by the Franck-Condon principle for excitation from the ground state.

1.3 Reaction Kinetics in a Flowing Steady State Afterglow

Within the last decade, thermal or near thermal energy reactions have received considerable attention in the literature with particular emphasis or reactions of interest in aeronomy. Improved methods for detecting and identifying reactants and products such as development of mass spectroscopic techniques have resulted in a considerable amount of data on rate constants of thermal energy reactions. Present experimental techniques for studying low energy reactions have been discussed by Paulson[31] which include; (1) internal ionization, (2) pulsed source, (3) drift tube, (4) ion and neutral beam, and (5) afterglow methods. In addition to the electron-ion recombination problem discussed briefly in Section 1.1, ion-molecule, charge transfer, and Penning ionization reactions are studied in afterglows.

Numerous recent reviews of experimental and theoretical investigations of low energy collision processes are available. Particular attention is directed to the work of Giese[32] for ion-molecule reactions with an emphasis on mass spectrometric measurements. Ferguson, Fehsenfeld, and Schmeltekopf[33] have summarized the theoretical studies of thermal energy ion-molecule reactions and have compared available experimental data with the various theoretical models. In another recent study, Stebbings[34] reviewed

many theoretical and experimental areas of charge transfer reactions and gives references of important work in the field. Penning ionization reactions and general collisions of electronically excited atoms and molecules are discussed in the works of Hasted[35], McDaniel[36], and Muschlitz[37].

The technique of using afterglows of gas discharge for studying thermal energy reactions gained considerable interest with improvements in ion detection methods brought about by mass spectrometric techniques. Steady-state concentrations of ion, electron, and metastable species in an afterglow are governed by rates of processes such as electron-ion recombination, ion-molecule reactions, charge transfer, radiation, Penning ionization reactions, and diffusion. The technique of measuring rate coefficients for thermal energy reactions by observing the temporal and spatial dependence of reactant concentrations requires detailed description of other processes affecting the reactants. Fite et al[5], Langstroth and Hasted[38], and Sayers and co-workers[39] studied thermal energy reactions between ions and neutrals in afterglows of gas discharges where reactant and product concentrations were monitored by high speed mass spectrometric methods.

As an extension to the static afterglow technique, Ferguson and his colleagues[40] developed a flowing steady-state afterglow system in which a wide variety of thermal energy reaction rates have been measured. Reactants and products are detected with a radio frequency mass spectrometer located downstream from the

reaction. A fast pumping system capable of producing flow velocities on the order of 10^4 cm sec^{-1} enable fast reactions on the order of 10^{-9} cm^3 sec^{-1} to be measured with uncertainties less than ± 30%.

1.4 Description of Present Experiments

Rate coefficients for thermal energy reactions involving several reactant gases with long-lived energetic helium species are measured in a flowing steady state helium afterglow. The helium reactants include the (2^3S) metastable atom, He^m, the $(a^3\Sigma)$ metastable molecule, He_2^m, the ground state atomic ion, He^+, and the ground state molecular ion, He_2^+. Reactant gases added to the helium afterglow include the species Ar, Kr, N_2, O_2, H_2, NO, CO, and CO_2.

A general technique is developed for measuring rates of reactions of energetic helium species with neutral reactants added to the afterglow. The observed rate constants are compared to values measured by other techniques when available. Decrease in helium concentration as a function of added reactant flow rate is interpreted in terms of a rate constant for the reaction. Relative concentration measurements of the helium species are made by introducing a "second reactant" to the afterglow and monitoring relative intensities of the resulting spectrum. Individual reactions involving a single helium species are studied by observing those transitions of the "second reactant" whose upper states are preferentially excited by the energetic helium species to be measured.

In the search for emission spectra of various reactants selectively excited by a single helium species, nitrogen was found to produce a number of strong band systems of N_2^+ which merit further study. Particular attention is given to the analysis of rotational and vibrational population distributions of the $B^2\Sigma$ - $X^2\Sigma$ first negative system for the following reasons; (1) it is the most readily observed band system of N_2^+ in different sources including impurity excitation in helium afterglows, (2) the vibrational levels are in close energy resonance with the energetic helium species, He^m and He_2^+, (3) Franck-Condon factors are known for excitation from the ground state of N_2, and (4) relative population distributions over the rotational levels of the (1,0) band which are perturbed by the close-lying levels of the $A^2\Pi$ state, contain additional information about formation and relaxation mechanisms for the $B^2\Sigma$ and $A^2\Pi$ states.

A study of population distributions over the vibrational levels of the excited $A^2\Pi$ $B^2\Sigma$, and $D^2\Pi$ states of N_2^+ is made under different experimental conditions designed to change the concentrations of exciting helium species relative to one another. Rotational population distributions are measured in the (0,0) and (1,0) bands of the $B^2\Sigma$ - $X^2\Sigma$ first negative system for the same set of conditions. Relative intensities of perturbed and unperturbed lines in the (1,0) band are analyzed in an effort to give insight into mechanisms of formation of excited levels and mechanisms of collisional energy transfer. In addition to the selectively-excited

nitrogen spectra, the short-lived "pink" afterglow[41] of an electrical discharge through pure nitrogen was studied as a source of N_2^+ emission.

A model consisting of the reaction mechanisms involving energetic helium and nitrogen is presented to account for the observed excited state nitrogen products.

I. REFERENCES

1. M. A. Biondi, Proc. 3rd Int. Conf. Phys. Electronic and Atomic Collisions, London (1963) p. 491.
2. C. Kenty, Phys. Rev. 32, 624 (1928), G. R. Court, Ph. D. Thesis Univ. of Birmingham, England, 1959.
3. M. A. Biondi and S. C. Brown, Phys. Rev. 76, 1697 (1949).
4. C. L. Chen, C. C. Leiby and L. Goldstein, Phys. Rev. 121, 1391 (1961); V. E. Golant, Soviet Phys. J. E. T. P. 5, 1197 (1961); E. Hinnov and J. G. Hirschberg, Phys. Rev. 125, 795 (1962); R. Hackam and J. J. Lennon, Proc. Phys. Soc. 84, 133 (1964); W. A. Rogers and M. A. Biondi, Phys. Rev. 134, A1215 (1964).
5. W. L. Fite, J. A. Rutherford, W. R. Snow and V. A. J. Van Lint, Dis. Far. Soc. 33, 264 (1962); P. G. Dickinson and J. Sayers, Proc. Phys. Soc. 76, 137 (1960).
6. F. C. Fehsenfeld, A. L. Schmeltekopf, P. D. Goldan, H. I. Schiff, and E. E. Ferguson, J. Chem. Phys. 44, 4087 (1966); R. A. Gerber, G. F. Sauter, and H. J. Oskam, Phys. Letters 19, 656 (1966).
7. A. V. Phelps and J. L. Pack, Rev. Sci. Inst. 26, 45 (1955); A. L. Schmeltekopf and H. P. Broida, J. Chem. Phys. 39, 1261 (1963).
8. J. M. Anderson, General Electric Res. Lab. Report No. 61-RL-2871G (1961).
9. M. A. Biondi, Rev. Sci. Inst. 27, 36 (1956); W. S. Bickel and C. R. Burnett J. O. S. A. 55, 1504 (1965).

10. H. R. Griem, M. Baranger, A. C. Kolb, and G. Oertel, Phys. Rev. 125, 177 (1962).

11. E. R. Mosburg, Jr. to be published.

12. W. A. Rogers and M. A. Biondi, Phys. Rev. 134, A1215 (1964).

13. K. B. Persson and S. C. Brown, Phys. Rev. 100, 729 (1955); E. P. Gray and D. E. Kerr, Ann. Phys. 17, 276 (1962).

14. E. E. Ferguson, F. C. Fehsenfeld, and A. L. Schmeltekopf, Phys. Rev. 138, A381 (1965).

15. D. R. Bates, A. E. Kingston, and R. W. P. McWhirter, Proc. Roy. Soc. A267, 297 (1962); A270, 155 (1962).

16. R. S. Mulliken, Phys. Rev. 136, A962 (1964).

17. C. B. Collins and W. W. Robertson, J. Chem. Phys. 40, 2202, 2208 (1964); F. E. Niles and W. W. Robertson, J. Chem. Phys. 40, 2909 (1964).

18. E. Hinnov and J. G. Hirschberg, Phys. Rev. 125, 795 (1962).

19. R. A. Gerber, F. G. Sauter, and H. J. Oskam, Phys. Letters 19, 656 (1966).

20. J. J. Hopfield, Phys. Rev. 36, 789 (1930); J. Janin and J. d'Incan, C. R. Acad. Sci. Paris 246, 3436 (1958); A. E. Douglas, Astrophys. J. 117, 380 (1953); K. C. Joshi, Proc. Phys. Soc. 87, 285 (1966).

21. O. S. Duffendack and H. L. Smith, Phys. Rev. 34, 68 (1929).

22. Y. Takahashi, Ann. Physik 3, 49 (1929).

23. Richardson, Molecular Hydrogen and Its Spectrum, Yale University Press, New Haven, Conn (1934) p. 194.

24. L. S. Headrick and O. S. Duffendack, Phys. Rev. 37, 736 (1939); N. D. Smith, Phys. Rev. 49, 345 (1936).

25. R. Meyerott, Phys. Rev. 66, 242 (1944), Phys. Rev. 70, 671 (1946).

26. L. Herman, P. Felenbok, and R. Herman, J. Phys. Radium 23, 979 (1962).

27. L. Herman and D. Rakotoarijimy, J. Phys. Radium 21, 629 (1960).

28. C. B. Collins and W. W. Robertson, J. Chem. Phys. 40, 701 (1964).

29. C. B. Collins and W. W. Robertson, 6th Int. Conf. on Ionization Phenomena in Gases, Paris (1963).

30. W. W. Roberston, J. Chem. Phys. 44, 2456 (1966).

31. J. F. Paulson, Ann. de Geophys. 20, 75 (1964).

32. C. F. Geise, Advances in Chemical Physics Vol 10, Interscience, New York (1966) p. 247.

33. E. E. Ferguson, F. C. Fehsenfeld, and A. L. Schmeltekopf, to be published.

34. R. F. Stebbings, Advances in Chemical Physics. Vol 10, Interscience, New York (1966) p. 195.

35. J. B. Hasted, Physics of Atomic Collisions, Butterworths, Washington (1964).

36. E. W. McDaniel, Collision Phenomena in Ionized Gases, Wiley, New York (1964).

37. E. E. Muschlitz, Jr., Advances in Chemical Phys. Vol 10, Interscience, New York (1966) p. 171.

38. G. F. O. Langstroth and J. B. Hasted, Dis. Far. Soc. 33, 298 (1962).

39. P. G. Dickinson and J. Sayers, Proc. Phys. Soc. 76, 137 (1960); J. Sayers and D. Smith, 3rd Int. Conf. on Phys. Electronic and Atomic Collisions, London (1963); P. H. Batey, G. R. Court, and J. Sayers, Planet. Space Sci. 13, 911 (1965).

40. F. C. Fehsenfeld, A. L. Schmeltekopf, P. D. Goldan, H. I. Schiff, and E. E. Ferguson, J. Chem. Phys. 44, 4087 (1966); 44, 4095 (1966).

41. G. E. Beale, Jr., and H. P. Broida, J. Chem. Phys. 31, 1030 (1959).

II EXPERIMENTAL APPARATUS AND TECHNIQUE

2.1 General Description

The experimental apparatus consisted of three separate flow systems in which thermal-energy reactions and the corresponding emission were studied in a steady-state afterglow of helium with added reactant gases.[1] The basic differences between the three arrangements were the mode of excitation of the gas, the flow rate, and the pressure range.

The lower pressure-larger diameter system is shown in Fig. 2.1. The discharge-afterglow reaction vessel was a pyrex tube of 900 mm length and 59 mm diameter. Pure helium (less than 10 ppm total impurities) was introduced into the system as the carrier gas. Impurities such as nitrogen, oxygen, hydrogen, and water vapor were decreased by another order of magnitude by passing the helium through an activated charcoal trap cooled to liquid nitrogen temperature.

Prior to the discharge region, the gas flow was interrupted by a medium fritted disk which was used to establish a uniform flow over the diameter of the tube at that point in the flow. When the pumping parameters were adjusted to give laminar flow with no turbulence, the velocity profile of the carrier gas was known as a function of distance down the tube. With such a parabolic velocity distribution, average velocities on the order of 2×10^4 cm-sec^{-1} were obtained with a flow rate of 185 atmosphere-cm^3 sec^{-1} and a downstream pressure of 0.6 torr.

Excitation of helium was produced in a continuous d.c. discharge maintained between a stainless steel hollow cylindrical cathode 65 mm diameter by 80 mm long and a 65 mm grounded-ring anode. Voltage was applied to the discharge through a resistor of 3000 ohms and incident power varied from 5 to 80 watts. Except when the dependence of discharge power was studied, the kinetic and spectroscopic measurements were performed with an incident power of 20 watts. This typical operating condition was chosen as a compromise between maximum afterglow intensity and a minimum of electrode sputtering. It is now known that aluminum electrodes cause much less sputtering than stainless steel or molybdenum.

To determine the effect of photoionization of reactant gases by helium resonance radiation, the discharge was operated in a single-pulse manner. Breakdown of the flowing helium was accomplished by charging a 105 microfarad 2500 volt capacitor to a value (~350 volts) slightly below breakdown and then initiating the discharge with a trigger pulse from a trigger transformer. From the transformer circuit, a pulse of about 1 volt was used to trigger the horizontal sweep of a cathode ray oscilloscope whose vertical deflection was connected to the photomultiplier of a grating monochrometer.

Downstream from the discharge in the afterglow region, two ports were provided for adding reactant gases at distances of 3 and 14 cm from the anode. With an average flow velocity of 10^4 cm sec^{-1}, these distances corresponded respectively to times of 0.3 and 1.4 milliseconds after the discharge. In the region of each reactant

gas input port, fused quartz windows transmitting up to 50% at 1700Å were provided for spectroscopic measurements. The reactant gases were added with flow rates small compared to the helium flow.

Pressure was measured with a capacitance manometer connected to the reaction tube by an on-off valve. A pressure range from 0.2 to 5.0 torr was used. In addition to the factory calibration, the manometer was calibrated against a McLeod gauge with a liquid nitrogen cold trap. Helium was used because it was the carrier gas in the experiment and with the added advantage that the systematic McLeod gauge error due to mercury streaming to the cold trap was expected to be minimum for helium. The manometer had a full scale sensitivity of 30 torr on the maximum scale and eight scale steps to a minimum full scale sensitivity of .01 torr. The overall accuracy of the pressure measurements in the range 0.2 to 5.0 torr was better than 5%. This calibration was good for other non-condensible gases since the manometer was insensitive to the type of gas measured.

The vacuum pump used to obtain high flow rates of helium was a Roots blower high speed pump backed by a mechanical rotary pump capable of speeds of better than 500 liters-sec^{-1}. The actual pumping speed at the end of the reaction tube was reduced by impedance due to the connecting lines and valves. Kinetic and spectroscopic measurements were performed with the pump valve open since the faster flow rates were normally required to spatially resolve the afterglow times down the reaction tube. The pressure could be

changed for a given mass flow rate by control of a valve at the exhaust of the reaction tube

A second flow system designed to operate with a downstream pressure range of 1 to 20 torr was a scaled-down model of the d.c. discharge-afterglow system shown in Fig. 2.1. The reaction vessel was a pyrex tube of 500 mm length and 19 mm diameter. The pumping system, mode of excitation of helium, method of adding reactant gases, and observation of afterglow emissions was similar to the first system described previously.

The higher pressure flow system in Fig. 2.2 was used primarily for spectroscopic studies of nitrogen excited in the helium afterglow, the "pink" afterglow of a pure nitrogen discharge, and the pressure dependence of rotational perturbations in the nitrogen emission spectra. The entire system shown in the figure was made of pyrex with separate components for greater flexibility. The discharge part of the tube was connected to the main reaction vessel with a standard taper ball and socket joint vacuum sealed with Apiezon hard wax. The charcoal trap was similarly connected to the discharge tube by a standard taper joint. In this manner, both the discharge tube and trap could be changed for various experiments.

Pure helium from the liquid nitrogen-active charcoal trap flows through a deLaval nozzle to the main reaction chamber[2]. One type of discharge nozzle used was a pyrex tube of 11 mm I.D. which was constricted abruptly to a 0.5 mm diameter opening and then formed a gradually diverging taper to 11 mm I.D. again. Variations on this

design were used. High pressure operation required a smaller diameter discharge tube of 7 mm I.D. A similar quartz nozzle was available for use with continuous high power operation because of the large amounts of heat generated.

The discharge was maintained in the region of the nozzle by a high frequency field of 2450 Mc sec^{-1} coupled to the gas by a 1/4-wave cavity of a special design[3]. The source of microwave power was a fixed-frequency magnetron and power supply capable of 125 watts maximum power. The position and tuning of the cavity was optimized by maximizing the helium afterglow intensity. This condition corresponded closely to a minimum in the reflected power from the cavity. Since the experiment was suspected to depend upon the presence of microwave fields in the afterglow and reaction region, the microwave cavity was shielded with aluminum foil. The presence of stray fields in the afterglow region have the effect of increasing the electron temperature which increases the ambipolar diffusion of electrons and positive ions loss to the walls.

Reactant gases were added to the helium flow 10 to 15 cm downstream from the discharge at flow rates small compared to those of helium. Mixing was accomplished by adding the reactants in the form of a concentric sheath as shown by the insert in Fig. 2.2. In the same region, an additional port was provided for adding a second reactant gas. With this configuration, the two reactants were added to the helium afterglow approximately in the same region and differentiation between the resulting emission for each reactant was not attempted.

A fused quartz window was provided at the region of mixing for spectroscopic investigations. The axis of the reaction tube was supported in a vertical direction since the spatial extent of the emission region could more easily be focused to fill the vertical spectrometer slits.

Pressure was measure by a Bourdon tube gauge with a maximum reading of 100 torr. Downstream pressures of 1 to 40 torr were used with pressure upstream of the nozzle estimated to be at least one order of magnitude larger. A mechanical rotary pump was used with a capacity of 65 liters-sec^{-1} since high flow rates were not necessary with the relatively high pressures used. A valve at the exit of the reaction tube was used to change the downstream pressure for a given helium flow rate.

The glassware in both systems was cleaned by washing with soap and hot distilled water, rinsing with distilled water, etching with a 12% hydrofluoric acid solution, and then rinsing again with distilled water. The individual pieces of glassware were vacuum connected to each other either by welding or by standard taper ground glass joints. Each joint was sealed by Apiezon hard wax with a softening temperature of 80° C which provided a rigid joint at room temperatures. This method generally gave fewer leaks than lower temperature vacuum greases. The glass reaction tube was connected to the pump and flow control valve by vacuum tight epoxy seals to metal flanges. The remaining vacuum connections to the discharge-afterglow tubes were made interchangeable by using 1/4 inch O.D.

tubing. In this manner, standard 1/4 inch plumbing fixtures, tubing, and valves could easily be used. Polyethylene tubing was used for interconnecting the various components. When the tubing was used on the high vacuum side of the valves, the length was kept at a minimum to lessen the possibility for leaks and outgassing.

As optical spectrometers were the primary diagnostic tool used in the experiment, their interchangeability and optical alignment were made easier by placing the reaction regions and the corresponding fused quartz windows at a height of 1 meter from the floor. In a similar manner, the various spectrometers were mounted 1 meter from the floor on casters and could easily be moved to the different systems and aligned.

Whenever a discharge-afterglow system was initially constructed or brought to atmostpheric pressure, the entire system including the interconnecting tubing was pumped for about 24 hours before an experiment was started.

2.2 Gas Flow Apparatus and Techniques

The quantitative study of reaction kinetics in a fast flow system requires careful consideration of the gas flow in the reaction tube and the method of mixing of the reactant gases. The flow rate, Q, is defined as the product of the volumetric flow thru a plane normal to flow and the pressure at that point,

$$Q = P\,dV/dt \qquad (2.1)$$

where units are torr-cm^3 sec^{-1}. Flow in a cylindrical tube is

classified as laminar when the ratio of the mean-free-path, L_a, to the radius, a, of the tube satisfies the inequality[4].

$$L_a/a < 0.01 \tag{2.2}$$

In the present experiment, the mean-free-path for helium at a temperature, T = 300°K, and an average pressure, P = 0.6 torr, was given to be $L_a = 2.5 \times 10^{-2}$ cm[4]. With the radius of the cylindrical reaction tube, a = 2.95 cm, the condition for laminar flow is satisfied since Eq. (2.2) gives the value, $L_a/a = 0.009$.

It has been experimentally shown for the laminar flow region, the flow can be described by by Poiseuille's equation,

$$Q = \frac{\pi a^4}{8\eta l} P_a(P_2-P_1) \tag{2.3}$$

where l is the tube length, η is the viscosity of the gas, P_1 and P_2 are the upstream and downstream pressures measured a distance l apart and P_a is their arithmetic mean value. The average velocity across a plane normal to the axis of the tube at a pressure, P, is defined by

$$\bar{u} = Q/\pi a^2 P \tag{2.4}$$

As the radial pressure gradient of the gas flow is rendered uniform by the location of the fritted disk in the flow pattern, the radial velocity distribution downstream is best described by a parabola. The velocity at the center of the tube is then two times the average while the velocity at the walls is zero. Under this assumption, the velocity at a given distance, r, from the axis of the tube is given

by[5]

$$u = 2\,\bar{u}(1 - 4r^2/d^2) \qquad (2.5)$$

Kaufman[6] has pointed out that serious errors can arise for kinetic experiments in fast flow systems if certain limitations, such as volume and surface recombination, diffusion, and viscous pressure drop down the tube, are not accounted for. Helium ion recombination and diffusion will be considered in the formulation of the reaction rate equations in Section 5.1. The magnitude of the viscous pressure change down the tube can be calculated from Poiseuille's equation. Following the discussion of Kaufman, Eq. (2.3) reduces to the following expression for small ΔP.

$$\Delta P/_l = 1.15 \times 10^{-6}\,\bar{u}_o/\,a^2 \qquad (2.6)$$

in which the helium viscosity was $\eta = 1.9 \times 10^{-4}$ g cm^{-1}sec^{-1} at a temperature, $T = 300^oK$[4]. For an average downstream pressure, $P = 0.6$ torr, the corresponding flow rate with the high speed pump open was $Q = 1.4 \times 10^5$ torr-cm^3 sec^{-1}. Taking the average velocity, $\bar{u} = 8.5 \times 10^3$ cm sec^{-1} calculated from Eq. (2.4) and substituting in Eq. (2.6), the viscous pressure drop over an axial distance of about $l = 14$ cm becomes $\Delta P = 0.015$ torr. The relative pressure change, $\Delta P/P$, is then below 5% and a distance of approximately 50 cm would be necessary to record a 10% change in pressure.

The application of kinetic equations for chemical reactions in flow systems is directly dependent upon the velocity distribution in the form of the reaction time, τ, defined as

$$\tau = l/\bar{u} \qquad (2.7)$$

where l is a reaction distance determined by the location of the

reactant gas input and the detection region. For a parabolic velocity distribution represented by Eq. (2.5), there is a distribution of reaction times with the average being twice the minimum. The question then arises as to whether the average reaction time should be used in the kinetic equations or a different time determined from the characteristics of the reaction such as flow and reactant mixing considerations.

Ferguson, et. al.[7] have used the visible helium afterglow to obtain a number for the average velocity. This was accomplished by pulsing the discharge and then detecting the onset of the afterglow downstream with a photomultiplier which could be moved the length and width of the reaction tube. The time between the discharge pulse and the afterglow arrival was interpreted as the flow time to that point.

A somewhat different method was used in the present experiment to measure the reaction times because of the different diagnostic methods used. The volumetric flow rate, dV/dt, was determined from the linear portion of the pressure increase in a calibrated volume into which the helium flow was introduced. Then, in the reaction tube, the flow rate was calculated from the expression.

$$Q = P\,{}^{dV}/_{dt} \qquad (2.1)$$

By operating in the laminar flow region, the average velocity was calculated from Eq. (2.4). However, a correction to the average velocity must be made as follows. The spatial extent of the nitrogen and carbon monoxide emission region used in the detection of

the excited helium species depended upon the flow and mixing parameters. Since the emission was used as a source for the spectrometer and at the same time was clearly visible, the estimated source height corresponding to the diameter of the emission was interpreted as a "effective" diameter of the flow pattern. For example, if the emission intensity was monitored for reactions occurring in a sufficiently narrow region along the axis of the tube, the maximum velocity or twice the average velocity would be used to calculate the reaction time. The average velocity for an imaginary cylinder concentric with the axis of the reaction tube and with a diamter given by the emission source height was calculated. From Eq. (2.5), the velocity component at a distance r from the axis is,

$$u = 2\bar{u}_o(1-{}^{4r^2}/_{d_o{}^2}) \qquad (2.5)$$

where $\bar{u}_o$ is the average velocity corresponding to the actual diameter of the tube, $d_o = 5.9$ cm. The volume of gas flowing through a concentric cylindrical tube of diameter, d, is then,

$$q = \int_0^{d/2} 2\pi r\, u\, dr \quad \text{cm sec}^{-1} \qquad (2.8)$$

Substituting Eq. (2.5) for u and integrating,

$$q = \frac{\pi\bar{u}_o d^2}{2}\left(1 - \frac{d^2}{2d_o{}^2}\right) \qquad (2.9)$$

As in Eq. (2.4), we can define an average velocity for the imaginary cylinder to be,

$$\bar{u} = \frac{q}{\pi(\frac{d}{2})^2} \qquad (2.10)$$

and obtain the following table for use in the kinetic studies.

TABLE 2.1

Source Diameter d cm	Average Velocity $\bar{u}$ cm sec^{-1}
1	$1.97\bar{u}_o$
2	1.89
3	1.74
4	1.54
5	1.28
5.9	1.00

A schematic diagram of the flow apparatus is given in Fig. 2.3. In addition, a fully developed velocity profile as described by Eq. (2.4) is shown downstream as would be expected for the laminar flow region. A large number of reactant gases added to the helium afterglow react with the energetic helium and cause visible emission. The extent of the emission region as a function of reactant flow rate can yield qualitative information about the method of mixing and the rapidity of mixing. When reactant gas is added in large excess, the downstream edge of the emission region appears to form a parabola. Although no quantitative measurements were made, this edge approximately fits the calculated velocity profile for the experimental flow conditions. Reactant gases were added to the helium afterglow at flow rates small compared to the carrier gas, and are assumed to diffusive mix with the helium to yield a uniform concentration.

Each input reactant line is provided with an on-off valve used in conjunction with a fine metering valve labeled "M" in Fig. 2.3. Fine-metering valves were used to set the gas flow with a relatively fine adjustment.

Volumetric flow rates were measured from the resulting pressure increase in a calibrated volume. The capacitive manometer described in Section 2.1 occupies two places in the figure for clarity. Two on-off valves were provided such that pressure could be measured in either the reaction tube or the calibrated volume, V_o. A recorder was driven by the output of the manometer in order to give a permanent record of the changing pressure as a function of time. The calibrated volume was a steel cylinder connected to an auxiliary pump through a gate valve. The volume of the cylinder was carefully measured to be, $V_o = 5955\ cm^3$. In order to measure volumetric flow rates using the calibrated volume, the gas flow was first set with the fine metering valves. With the volume evacuated and closed to the auxiliary pump, the flow was redirected into the volume with the appropriate on-off valves. With a record of the change in pressure as a function of time, the differential, dP/dt, could be measured from the graph for the linear portion of the change. For the kinetic experiments, the flow rate was measured both before and after a measurement. The estimated accuracy of this method was better than 10%.

In addition to the calibrated volume technique, a floating-ball type flowmeter was used to measure the reactant gas flows. The

float was an 1/16 inch sapphire ball and the flowmeter was capable of measuring nitrogen flow rates up to 1.6 cm^3 sec^{-1} at NTP. In the flowmeter line, a 100 psi full-scale Bourdon type pressure meter was connected such that the upstream pressure could be set accurately at the calibration value. The estimated accuracy of the floating-ball type meter was 10%.

2.3 Spectroscopic Apparatus and Technique

Several spectrometers were used in this research including a Fastie-Ebert monochromator[8] with photoelectric detection, a low resolution Bass-Kessler grating spectrograph[9], a Huet double quartz prism spectrograph. The photographic spectrometers were used to obtain spectra of the helium afterglow and nitrogen emission in the wavelength region 2260 to 8500Å. The grating monochromator was used for the high resolution spectra, helium absorption and other relative intensity measurements.

Low resolution photographic spectra in the wavelength region 3900 to 8500 Å was obtained in the first order with the Bass-Kessler spectrograph with a grating of 1200 lines per mm ruled over a 65 mm width and blazed for 5000 Å. The instrument has a focal ratio of f/5.6 and the camera accepts a 3 1/4 x 4 1/4 glass plate. Eastman Kodak 103a-F and hypersensitized I-N plates were used in the 3900 to 6000 Å and 6000 to 8500 Å wavelength regions respectively. The hypersensitization process carried out in total darkness involved washing the I-N plates in 12% ammonium hydroxide bath for 3 minutes,

rinsing in methyl alcohol for 2 minutes, and then rapid drying in a flow of dry air for 5 minutes. Using 100 micron slit widths, exposure times varied from about 5 seconds for the strong nitrogen band systems to 90 minutes for some weaker systems in the near infrared region.

A second Bass-Kessler spectrometer with quartz optics having a grating with 1200 lines per mm and blazed at 3000 Å in the first order was used for the wavelength region 2300 to 3900 Å. Eastman 103a-O spectroscopic plates were used. With 100 micron slits, 90 minutes was the longest exposure time used.

In addition to the quartz Bass-Kessler, the Huet quartz prism spectrometer with a f/3.5 focal ratio was used in the region 2260 to 3000 Å where its resolution was comparable or better than the grating instrument.

The grating monochromator was a double pass, 0.8 meter Fastie-Ebert mount with a focal ratio of f/10 and employed photoelectric detection. The grating with 1200 lines per mm ruled over 65 mm width was blazed for 5000 Å in the first order. Measurements of the rotational structure in the excited nitrogen band spectra were made in the second order of the grating and with 6 and 10 micron wide curved slits giving a resolution of about 100,000 and 80,000 respectively. Observations of the relative vibrational and electronic populations were usually made in the first order with 200 and 500 micron curved slits. The photomultiplier was an EMI 9558Q with a S-20 response and a quartz window. With this arrangement,

the wavelength range capability of the monochromator was 2000 to 8250 Å. To improve the signal to noise, the tube was operated in a cooled manner with dry ice. The photomultiplier was connected to a fast response picoammeter whose output drove a 10 millivolt recorder with a 1 second response.

The relative intensity response as a function of wavelength was calibrated for the complete spectrometer including filters with a special factory calibrated irradiance standard composed of a high temperature quartz-iodine lamp and power supply. The determination of the spectral response of the monochromator was made for the wavelength region from 2500 to 8250 Å.

When the source height does not fill the collimator of the spectrometer with light, a common practice is to use a condensing lens to form an image of the source at the slit position in order to increase the illumination of the spectrometer. With this optical arrangement, each point on the slit and hence each point on the exit slit was illuminated by a different point of the source. The nitrogen emission excited in a helium afterglow appears inhomogeneous to the eye and the method of quenching of the nitrogen band systems relative to one another changes the emission source in a nonuniform way. Therefore, a different method of illumination was used in the present experiment to reduce the difficulty of the nonuniform illumination. The condensing lens was placed near and in front of the spectrometer slit such that the source was reimaged on the collimator mirror. The source distance and focal length of the

condensing lens could be adjusted to either magnify or demagnify the source such that its image just filled the collimator. Uniform illumination of the slit was obtained since each point on the source sends light to each point on the slit.

For absorption measurements by the metastable helium, a second d.c. discharge with flowing helium was set up behind the reaction tube along the axis of the grating monochromator. The flow and power applied to the discharge could be varied to give a steady bright atomic helium light source for the HeI 3889 Å line.

In order to measure the afterglow emission intensity as a function of time for pulsed operation of the discharge, the grating monochromator was used with 200 micron slits. The output of the photomultiplier was connected directly to a cathode ray oscilloscope through a high gain differential amplifier with a sensitivity range of 1 millivolt to 50 volts and a band width for the 1 millivolt range corresponding to 0.3 Mc/sec. The output of the photomultiplier was recorded on Polaroid film.

2.4 Helium Purity

It is a well known problem that small concentrations (~10 ppm) of impurities such as nitrogen, oxygen, hydrogen, and water vapor have a large quenching effect on the afterglow intensity in a helium flow system[2,10]. In many cases, the impurity concentration is approximately the same order of magnitude as that of the helium ion and metastable atom. Energetic helium species responsible for the

afterglow emission are removed from the flow by charge transfer and inelastic collisions with the impurities.

A significant part of this experiment is concerned with the excitation of nitrogen in the helium afterglow and the description of the detailed reaction mechanisms. Nitrogen impurity in the helium could easily be excited in the discharge region and give erroneous results. A somewhat different problem would occur if significant amounts of neon were present in the helium. Collisions with metastable helium excited in the discharge excite energy levels of the neon atom, some of which are metastable. Then in the reaction tube, the neon metastables could excite nitrogen downstream and compete with the helium.

There exists several methods for obtaining very pure helium although for the most part they are used in static systems. Cataphoresis[11] is one of the best methods for removing impurity gases, but could not be used for the present experiments because of the high flow rates needed. Another purification method allows helium to leak through a heated quartz wall[12], but again the method is not easily useful for large flow rates. Helium obtained by carefully evaporating the liquid was found to remove neon but to contain significant amounts of hydrogen[10]. The sorption of gases by finely divided solids such as active charcoal and alumina has found widespread use in high-vacuum technique[4]. This last method was used in conjunction with high purity commercially available helium in the present experiments primarily because the method can be used for high helium flow rates.

There is a large amount of information on the sorption data for activated coconut charcoal and the atmospheric gases. Dushman[4] gives extensive tables for the volume of gas adsorbed as a function of gas pressure and charcoal temperature. In the present experiments, it would be instructive to know the relative amounts of impurity gases adsorbed by the activated charcoal when they are present in concentrations on the order of 10 ppm in the helium flow system. Two grades of helium were used; one commercial cylinder was rated as 99.97% pure and the other was provided with an impurity analysis having a total concentration of 4.9 ppm. The relative concentrations of selected impurities were recorded by measuring the relative intensity of their characteristic emission in the afterglow region. The grating monochromator fitted with 200 micron slits was used to record the relative intensities of Ne, H, O, OH, O_2^+, and N_2^+ as well as the atomic and molecular helium emission spectra.

Intensities were recorded to compare the two grades of helium and to determine the effect of the activated charcoal trap operated at room temperature and at liquid nitrogen temperature. The ratio of the impurity intensity to the atomic helium intensity was used for comparison because of the difficulty in exactly reproducing the same experimental conditions for the different gases and trap situations. Changes in the ratio of the measured intensities was not a direct measure of the impurity concentration because the helium

emission intensity itself depends on the type and amount of impurity, but gave qualitative estimates.

Whenever the flow system was opened to the atmosphere, the system was evacuated overnight after the charcoal had been heated under vacuum. The high pressure flow system in Fig. 2.2 was used with the reactant gas input ports sealed near the tube to lessen the change of outgassing.

The microwave discharge was operated with an input power level of 20 watts to the cavity. Downstream pressure was maintained at 2 torr except for the neon impurity measurements where a pressure of 32.5 torr was required.

In Table 2.2, the results are given for the particular impurities that could be identified. The intensity ratios preceded with an inequality indicate possible overlapping systems and the actual impurity intensity may well be less than the stated values. It has been assumed that the relative concentrations of the impurities were proportional to their corresponding intensities. Relative values quoted in the table should be taken to show order of magnitude changes, since several of the intensity measurements, particularly those quoted in columns C and F, were made with signal to noise ratios of about one. Mass spectral analysis of the type A helium by the Bureau of Mines contain the following impurity concentration (in ppm): H_2 (0.0); CH_4 (0.0); H_2O (2.8); Ne (0.7); N_2 (1.1); O_2 (0.3); Ar (0.0); and CO_2 (0.0). Type B helium is stated to be of 99.97% purity by the supplier.

TABLE 2.2

I (impurity)/I (He 4921.9Å)

	A	B	C	D	E	F
H_β (4861)	.42	.42	<.004	.110	.093	.012
OH (3078)	.023	.027	.001	.068	.062	.001
N_2^+ (4600)	.053	.055	.001	.278	.276	<.003
O (4969)	.026	.030	<.002	.042	.034	.004
O_2^+ (5632)	.006	.069	.003	.069	.057	.003
He_2(4650)	.057	.051	.125	<.01	.012	.127
*He_2(4650)	----	.216	1.83	----	.081	.450
*Ne (5401)	.065	.031	.285	.030	.038	2.13

* Measured at a pressure of 32.5 torr

A--Type A helium, no trap
B--Type A helium, room temperature trap
C--Type A helium, liquid nitrogen temperature trap
D--Type B helium, no trap
E--Type B helium, room temperature trap
F--Type B helium, liquid nitrogen temperature trap

For the impurity gases, nitrogen, oxygen, and water vapor, it is evident that the use of the activated charcoal trap at room temperatures has no particular advantage over the no-trap condition. On the other hand, cooling the trap to liquid nitrogen temperature decreased the impurity concentration by one to two orders of magnitude. The relative increase of the molecular helium emission compared to the atomic upon cooling of the trap could be related to a complex excitation mechanism depending upon the metastable helium species. As the charcoal trap removes the impurities responsible

for quenching the energetic helium, the relative production of molecular helium is increased. If the assumption that the primary excitation of the neon is due to the molecular helium ion, then the relative change in neon should follow the molecular helium emission, which it does.

II References

1. F. C. Fehsenfeld, A. L. Schmeltekopf, P. D. Goldan, H. I. Schiff, and E. E. Ferguson, J. Chem. Phys. 44, 4087, (1966).
2. A. L. Schmeltekopf and H. P. Broida, J. Chem. Phys. 39, 1261 (1963).
3. F. C. Fehsenfeld, K. M. Evenson, and H. P. Broida, Rev. Sci. Inst. 36, 294 (1965).
4. S. Dushman, Scientific Foundations of Vacuum Technique, John Wiley and Sons, Inc., New York (1962).
5. Sir H. Melville and B. G. Gowenlock, Experimental Methods in Gas Reactions, Macmillan and Co., Ltd., London (1964).
6. F. Kaufman, Prog. in Reaction Kinetics, 1, 3 (1961).
7. P. D. Goldan, A. L. Schmeltekopf, F. C. Fehsenfeld, H. I. Schiff, and E. E. Ferguson, J. Chem. Phys. 44, 4095 (1966).
8. W. G. Fastie, J. Opt. Soc. Am. 42, 641 (1952).
9. A. M. Bass and K. G. Kessler, J. Opt. Soc. Am. 49, 1223 (1959).
10. C. B. Collins and W. W. Robertson, J. Chem. Phys. 40, 701 (1964).
11. A. L. Schmeltekopf, dissertation, Univ. of Texas, Austin, Texas (1962).
12. F. J. Norton, J. Am. Ceramic Soc. 36, 90 (1953).

II Figure Legend

2.1 Low pressure d.c. discharge-afterglow flow system.

2.2 High pressure microwave discharge-afterglow flow system showing cross section view of deLaval nozzle and reactant gas input.

2.3 Schematic diagram of low pressure d.c. discharge-afterglow flow system and gas handling apparatus.

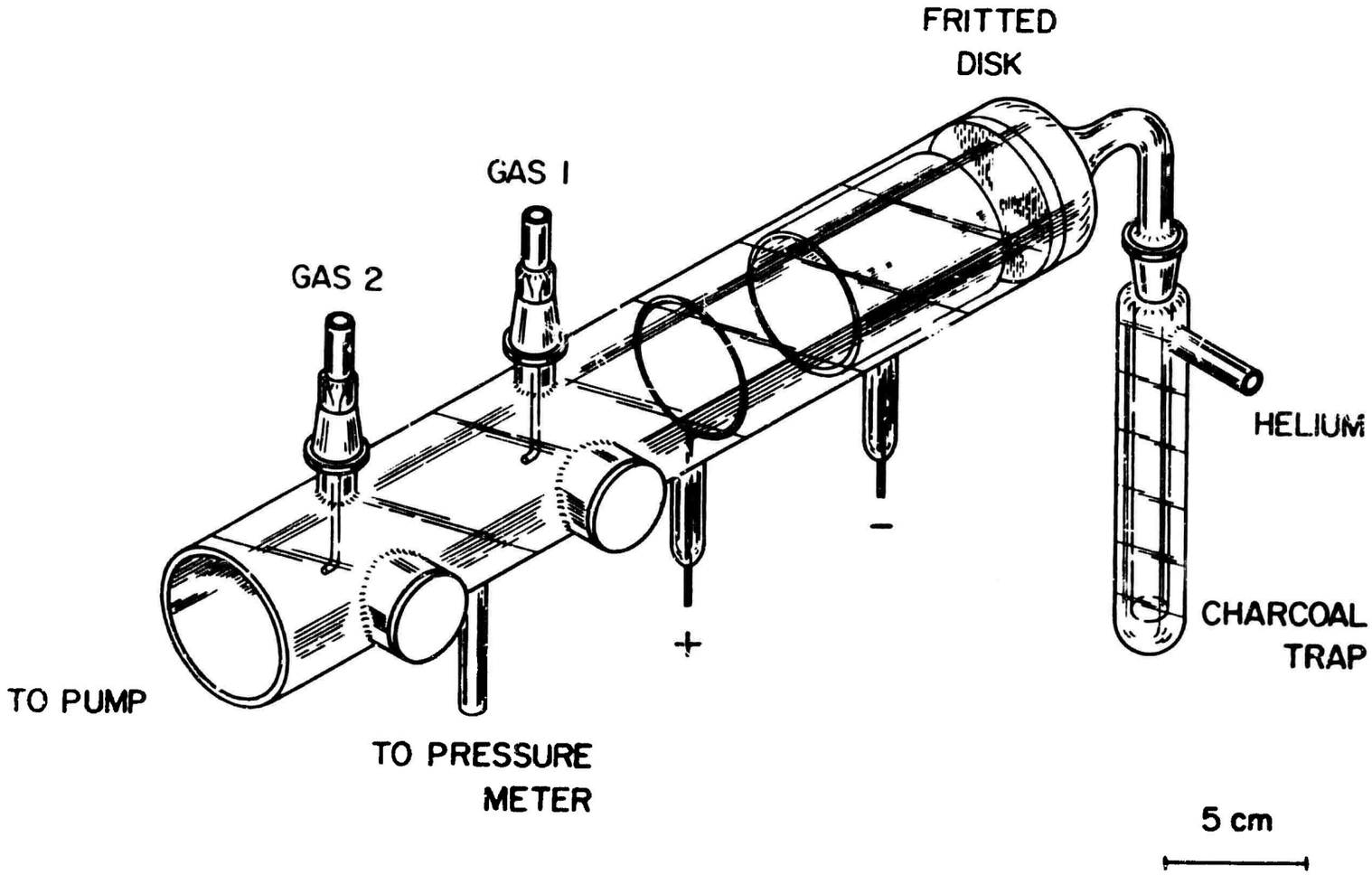
FRITTED
DISK
GAS 1
GAS 2
HELIUM
CHARCOAL
TRAP
TO PUMP
TO PRESSURE
METER
+
−
5 cm

FIG 2.

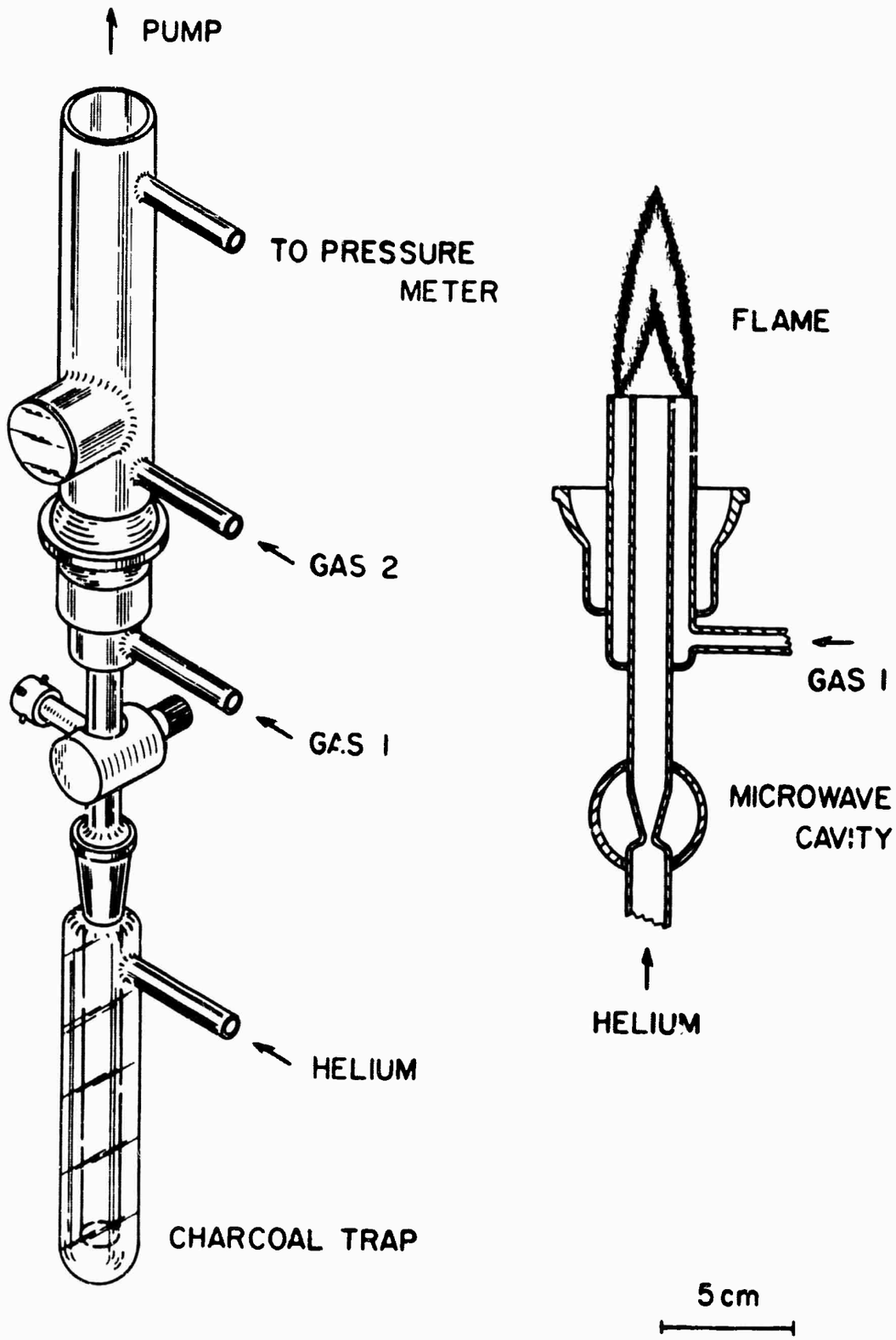
PUMP
TO PRESSURE METER
GAS 2
GAS 1
HELIUM
CHARCOAL TRAP
FLAME
GAS 1
MICROWAVE CAVITY
HELIUM
5 cm

FIG 2.2

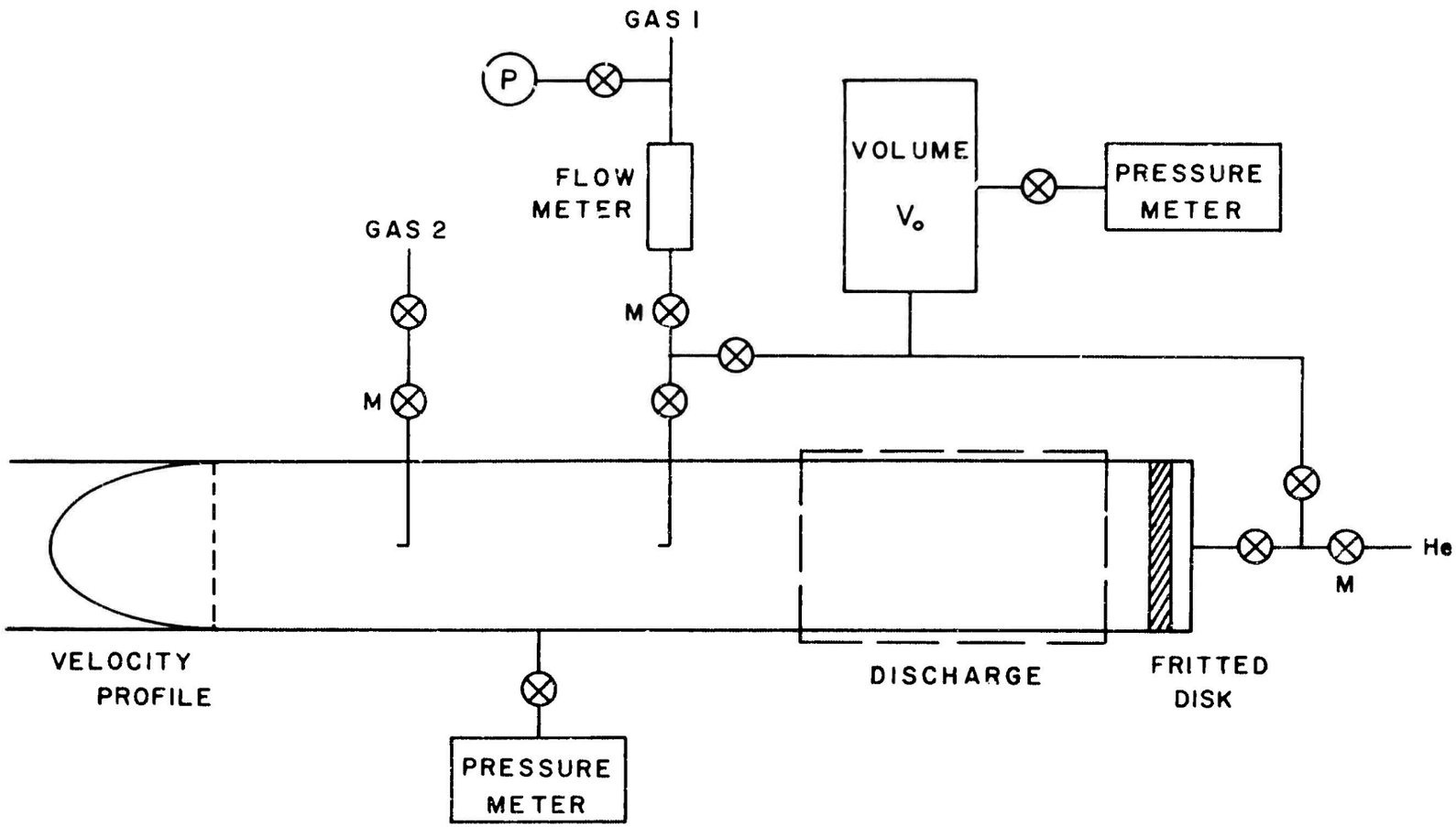
GAS I
P
FLOW
METER
VOLUME
V_o
PRESSURE
METER
GAS 2
M
M
He
M
VELOCITY
PROFILE
DISCHARGE
FRITTED
DISK
PRESSURE
METER

FIG 2.3

III ANALYSIS OF THE NITROGEN SPECTRUM

Selective excitation of nitrogen added to a helium afterglow as a minority gas was studied by observing the resulting nitrogen emission under a variety of experimental conditions. The intensity distribution among the excited electronic states is interpreted in terms of collisions of the second kind with energetic helium species. Particular attention is directed to the vibrational and rotational level populations in the $B^2\Sigma$ state of N_2^+ as determined from the relative intensity distribution in the $B^2\Sigma$ - $X^2\Sigma$ first negative system.

Correlations between the selectively excited spectra and exciting helium species were studied to determine the reaction mechanisms responsible for the nitrogen excitation. Knowledge of reactants and associated kinetic and internal energies, one can predict reaction mechanisms leading to excited state products according to the Franck resonance rule[1] and Franck-Condon factors for excitation from the ground state[2]. A particularly useful diagnostic method amounted to changing the relative concentrations of energetic helium species by changing the experimental conditions and then observing relative changes in the resulting spectrum. This method proved to be important because it was found that several of the energetic helium species could contribute to the population of the same excited state.

A detailed study of the (0,0) and (1,0) bands of the $B^2\Sigma$ - $X^2\Sigma$ system is included in which the distributions of population over the

rotational levels were investigated as a function of experimental conditions. A study of the rotational perturbation appearing in the $v = 1$ level of the $B^2\Sigma$ state due to the close-lying $A^2\Pi$ state is made. The pressure dependence of the perturbed rotational lines relative to the unperturbed contains information about formation and relaxation mechanisms for the $B^2\Sigma$ and $A^2\Pi$ states.

A study of population distributions over the vibrational levels of the excited states ($A^2\Pi$, $B^2\Sigma$, and $D^2\Pi$) of N_2^+ was made under different experimental conditions designed to change the concentrations of exciting helium species relative to one another. Particular attention was given to the $B^2\Sigma$ - $X^2\Sigma$ system where the important results aided in assignment of the individual reaction mechanisms responsible for the N_2^+ excitation.

3.1 Photographic Spectra for Helium and Helium-Nitrogen Afterglow Emissions from 2300 to 8700Å

The continuous d.c. discharge-afterglow flow system described in Section 2.1 was used to obtain low resolution photographic spectra of the pure helium and enhanced nitrogen spectra in the afterglow. Spectra were obtained for the experimental condition of 0.6 torr downstream pressure, a helium flow rate of 185 atmosphere -cm^3 sec^{-1}, and discharge maintained at an incident power of about 40 watts. The afterglow of pure helium appeared as a pink glow extending downstream 5 to 30 cm corresponding to times of approximately 1 to 10 msec. after the discharge. Upon addition of trace quantities of

nitrogen to the afterglow, a resulting bright blue-white emission delineated the helium glow downstream from the nitrogen input. The nitrogen emission consisted of two well-defined regions; a diffuse blue cone symmetrical to the tube axis, and a narrow bright white region surrounding the blue cone at larger radial distances from the axis. The intensity of each region could be varied relative to one another by changing the experimental conditions; this effect is discussed in Section 3.3.

Spectra as observed in the region 2260 to 8700Å are reproduced in Figs. 3.1 thru 3.5. The spectra were obtained with the f/3.5 Huet quartz prism spectrograph for the region 2260 to 3000Å and the region of 3000 to 8700Å was photographed with the f/5.6 Bass-Kessler grating spectrograph. Emission spectra for the pure helium afterglow are reproduced in the upper photographs of Figs. 3.2 thru 3.4 corresponding to the wavelength range, 2800 to 6400Å. Atomic lines and molecular band head wavelengths are labeled accordingly and the multiplicity of the transition is indicated by (S) for singlet and (T) for triplet. The HeI wavelengths were obtained from the complete table of Martin[3] while assignments of the He_2 band head wavelengths were made according to Rosen[4] and the recent work of Ginter[5].

The nitrogen spectrum for the wavelength region 2300 to 3000Å is composed of the $D^2\Pi_g$ - $A^2\Pi_u$ Janin-d'Incan system of N_2^+ and is reproduced in Fig. 3.1. This system has also been excited in a microwave discharge through Ne with N_2[7] and in a condensed discharge through Ne with about 1 to 5% N_2.[6]

Vibrational assignments were made from the band head wavelengths reported by Tanaka, et.al[6], where levels to v' = 11 of the $D^2\Pi$ state are observed to be populated. Individual bands are composed of two heads degraded to the red; the rotational lines appear closely spaced because of overlapping branches.

Spectra of the readily occurring $B^2\Sigma$ - $X^2\Sigma$ first negative system are reproduced in Figs. 3.2 thru 3.4. Low pressure discharge tubes containing nitrogen and an excess of helium, hollow cathode discharges, shock tubes, and upper atmospheric emission phenomenor are well known sources for this same system. Individual bands originating in the low vibrational levels (v' < 10) of the $B^2\Sigma$ state are single headed and degraded to the violet. The strong bands form well defined sequences drawing together to a turning point and then separating again in the opposite wavelength direction. The sequence of bands occurring after the turning point are the "tail bands" originating from high vibrational levels which have been observed up to v' = 21 in the afterglow source. Individual tail bands are labeled above the normal first negative system in Figs. 3.2 and 3.3 and appear degraded to the red. Wavelength assignments for the observed bands were obtained from tables of Wallace[8].

The $A^2\Pi$ - $X^2\Sigma$ Meinel system of N_2^+ occurs readily in the nitrogen spectra reproduced in Figs. 3.4 and 3.5. Meinel first observed bands with v' $\leq$ 5 occurring in the aurora[9] and later the system was observed in low pressure and hollow cathode discharges

through N_2 and He mixtures[10]. Wavelength assignments of bands with $v' \leq 5$ were made according to Wallace[8]. Wavelength positions of observed band origins not yet reported for $v' > 5$ were calculated from the vibrational energies of the $A^2\Pi$ and $X^2\Sigma$ states[8]. The new assignments include the bands; (6,2), (7,3), (8,3), (9,4), (10,5), (11,6), (12,6), and (13,7).

Two well known band systems, the $B^3\Pi$ - $A^3\Sigma$ first positive system and $C^3\Pi$ - $B^3\Pi$ second positive system of the neutral nitrogen molecule, are readily observed in discharges through N_2 but occur only weakly in the present afterglow source. This lack of an extensive first positive system in the wavelength region 5800 to 7000Å greatly facilitated the new band assignments in the Meinel system.

In addition to the spectra of molecular nitrogen, strong atomic nitrogen emission lines occur in the present afterglow source reproduced in Fig. 3.5. Wavelength assignments are taken from the tables of Nawrocki and Papa[11]. It is interesting to note that the observed atomic nitrogen lines were also reported in auroral sources by Meinel.[12]

The pure helium and selectively-excited nitrogen spectra discussed in this section and reproduced in Figs. 3.1 thru 3.7 were obtained for the set of experimental conditions producing the brightest nitrogen glow. The excited nitrogen spectra was also investigated over a pressure range of 0.2 to 5 torr in the d.c. discharge afterglow system and 0.55 to 25 torr in the afterglow of the microwave discharge. Relative changes in the resulting spectra

were studied for changes in the helium flow rate from 50 to 200 atmosphere - cm^3 sec^{-1} and incident power applied to the discharge from 5 to 80 watts.

A special condition of the afterglow for which large relative changes have been observed in the resulting nitrogen spectra merits further comment. A relatively weak green glow was observed immedia- downstream from the intense blue-white glow of nitrogen with t. ce amounts of nitrogen added to the afterglow. A helium flow rate of approximately 185 atmosphere cm^3 sec^{-1} was used with a power applied to the discharge of 80 watts. Production of the green glow was very sensitive to small changes in experimental conditions and in particular the nitrogen flow rate. Resulting nitrogen spectra in the 3800 to 6000Å wavelength region was predominately atomic nitrogen.

3.2 Rotational Structure of (0,0) and (1,0) Bands of the $B^2\Sigma$ - $X^2\Sigma$ First Negative Transition in N_2^+

In the case of $^2\Sigma$ - $^2\Sigma$ transitions, the selection rule $\Delta K = \pm 1$ determines the rotational structure within the individual bands; an R-branch with $\Delta K = +1$ and a P-branch with $\Delta K = -1$. Each rotational level consists of two closely spaced sublevels with $J = K \pm \frac{1}{2}$. The corresponding rotational lines normally appear as unresolved doublets with $\Delta J = \pm 1$. The $\Delta J = 0$ component has negligible intensity compared to the $\Delta J = \pm 1$ lines[13].

An intensity alternation of the rotational lines occurs because

of the symmetry properties of homonuclear molecules. For N_2^+ where the N^{14} nucleus has a spin of I = 1, the rotational lines with even K have nuclear statistical weights two times the values for the odd lines. Relative populations of the rotational levels as a function of K' give information pertaining to mechanisms of populating and depopulating the rotational levels. This method of analysis will be discussed later in the section.

A good example of a $^2\Sigma$ - $^2\Sigma$ transition is provided by the (0,0) band of the $B^2\Sigma$ - $X^2\Sigma$ first negative system reproduced in Fig. 3.6. From the band origin at λ_o = 3911.4Å, the P-branch forms a single series of lines with increasing wavelength to K' = 12 where it turns back on itself forming the band head. Further increase in K' corresponds to a decrease in wavelength as indicated by the dashed lines. The R-branch is composed of a single series of lines with decreasing wavelength. The overall effect gives the bands an appearance of being degraded toward the red.

The (1,0) vibrational band of the $B^2\Sigma$ - $X^2\Sigma$ first negative system is reproduced in Fig. 3.7. Being a $^2\Sigma$ - $^2\Sigma$ transition, its general form is similar to the (0,0) band discussed previously. Starting at the band origin, λ_o = 3579.4Å, the series of lines composing the P-branch increases with increasing wavelength to K' = 12 where it turns back on itself forming the band head. The R-branch lines decrease in wavelength with increasing K. Anomalous spin doublet splittings observed in the (1,0) band for K' > 8 is caused

a resonance perturbation in the rotational term series of the upper $v' = 1$ level of the $B^2\Sigma$ state by the nearly degenerate rotational levels of the $v' = 11$ level of the $A^2\Pi$ state. Fassbender[13] and Coster and Brons[14] analyzed the rotational perturbation occurring near $K' = 13$ in the (1,1), (1,2), and (1,3) bands. Actual spin splittings are due to a perturbed energy shift of the $F_2(K)$ components given by $J = K - \frac{1}{2}$ with a maximum shift occurring between $K' = 12$ and 13. The resulting wavefunction for the perturbed levels is a linear combination of the unperturbed $^2\Sigma$ and $^2\Pi$ wavefunctions.[15] An extra line (E) occurs near $K' = 13$ and is the corresponding perturbed $A^2\Pi - X^2\Sigma$ transition. In addition to the strong perturbation near $K' = 13$, a second weaker perturbation is predicted to occur near $K' = 1$ in the $F_1(K)$ components which manifests itself in broadening of the $K' = 0$, 1 and 2 rotational lines.

The distributions of population over the rotational energy levels in thermal equilibrium follow Maxwell-Boltzmann statistics in which the number of molecules in the J rotational level at a temperature T is given by the expression[15],

$$N_J = N_v hc \frac{Bv}{kT} (2J + 1) \exp [- B_v J(J + 1) hc/kT] \qquad (3.1)$$

where N_v is the number of molecules in the vibrational level, v, B_v represents the rotational constant, and the remaining symbols have their usual meaning. In emission, the intensities of the rotational lines within a band can be written,

$$I = \frac{C\nu^4}{Q_r} (J' + J'' + 1) \exp [- B_v' J'(J' + 1) hc/kT] \qquad (3.2)$$

where Q_r is the partition function and the factor $\frac{C_\nu^4}{Q_r}$ is nearly constant for a given vibrational band. Eq. (3.2) can be written

$$\ln\left[\frac{I}{J' + J'' + 1}\right] = A - \frac{B_v' J'(J' + 1)hc}{kT} \qquad (3.3)$$

where $A = \frac{C_\nu^4}{Q_r}$. For the homonuclear molecule, N_2^+, the nuclear statistical weight, g_n, is included and Eq. (3.3) becomes,

$$\ln\left[\frac{I}{g_n(J' + J'' + 1)}\right] = A - \frac{B_v' J'(J' + 1)hc}{kT} \qquad (3.4)$$

where $g_n = 1$ or 2 for odd or even rotational levels respectively. By plotting $\frac{I}{g_n(J' + J'' + 1)}$ against $J'(J' + 1)$ or the rotational term, $F_v(J)$, a straight line results with a slope of $-B_v'hc/kT$ for the condition of thermal equilibrium among rotational degrees of freedom. An effective rotational temperature can be calculated from the slope. Moreover the form of the logarithmic plot may reflect the mode of excitation whether or not in thermal equilibrium.

Observed values of $\ln I/g_n(K' + K'' + 1)$ in the (0,0) band at 3914Å are plotted against $K'(K' + 1)$ for the even rotational lines of the P-branch in Fig. 3.8. K is used instead of J for the (0,0) band since the spin doublet splittings $J = K \pm \frac{1}{2}$ are not resolved and the $^2\Sigma - {}^2\Sigma$ transition has the same structure as a $^1\Sigma - {}^1\Sigma$ type[15]. The linear dependence of the two series of points indicates that there is thermal equilibrium for which effective rotational temperatures of 480°K and 360°K are calculated for (A) and (B) respectively. Representative data for (A) were obtained in

the afterglow of the microwave discharge (Fig. 2.2) with a downstream pressure of 10 torr and discharge power of 17 watts. For comparison, (B) was measured at a pressure of 0.6 torr in the afterglow of the d.c. discharge system (Fig. 2.1) operated with an incident power of 50 watts.

Rotational temperatures measured in system (A) showed no significant dependence on pressure for a range of 0.55 to 20 torr. Rotational temperatures measured in system (B) increased with increasing pressure from 325°K at 0.3 torr to 525°K at 1.25 torr. A linear dependence of $\ln[I/g_n(K' + K'' + 1)]$ plotted against $K'(K' + 1)$ was observed for each series of measurements. From repeated measurements of the rotational temperature for the same experimental conditions, the uncertainty in the measured temperatures were estimated to be approximately $\pm$ 30°K.

Similarly, observed values of $\ln[I/g_n(J' + J'' + 1)]$ for the P-branch of the (1,0) band are plotted against $F_v(J')$ in Figs. 3.9 and 3.10. With the spin doublet resolved into $F_1(K)$ and $F_2(K)$ components due to the perturbation, J was used instead of K. For the unresolved levels with $K' < 9$ the factor $g_n(J' + J'' + 1)$ in Eq. (3.4) was calculated for the sum of the two components. The rotational population distributions in the (1,0) band were measured for the identical experimental conditions outlined previously for the (0,0) band.

Curve (B) in Fig. 3.9 corresponds to (B) in Fig. 3.8 measured at a downstream pressure of 0.6 torr. Circles represent the unresolved

components for $K' < 8$ and the $F_1(K)$ levels for $K' > 8$; triangles correspond to the perturbed $F_2(K)$ components; and the extra line from $A^2\Pi$ state near $K' = 13$ by E. A slope corresponding to the temperature 360^oK obtained from the (0,0) band measurements is given by the broken line. The scatter of data points can largely be attributed to the low signal to noise ratios for the measurements. In general, the data indicates a linear dependence except for a small decrease in the population for the low rotational levels with energies between 50 and 200 cm^{-1}. This apparent non-thermal distribution may be caused by self-absorption[16]. A search of the (0,0) band data of which the curves in Fig. 3.8 are representative samples was made for apparent non-thermal distributions. A small decrease in the population was observed for the low rotational levels, but unfortunately this observation is least evident in the representative data in Fig. 3.8.

The (1,0) band high pressure data at 10 torr corresponding to (A) is reproduced in Fig. 3.10. The broken line has been drawn with a slope corresponding to a rotational temperature of 480^oK which was calculated from the (0,0) band data. However, a more evident linear dependence for the unresolved and unpertureed $F_1(K)$ components is given by the solid line with a slope characteristic of 880^oK. Rotational levels of the perturbed $F_2(K)$ components and the extra line have significantly lower populations than their corresponding unperturbed components with the largest deviation occurring near the rotational energy of maximum perturbation. In

addition, the region of a weaker perturbation near K' = 1 shows a corresponding decrease in the observed populations.

In the afterglow of the microwave discharge corresponding to the (A) curves, rotational population distributions in the (1,0) band were measured for pressures between 0.55 to 20.0 torr. Observed values of $\ln[I/_{gn}(J' + J'' + 1)]$ for the unperturbed components did not vary linearly with $F_v(J')$ but exhibited deviations with respect to each other. However, the observed values of the perturbed components relative to the unperturbed showed a definite decrease with increasing pressure. To gain insight into the general effects of the perturbation and pressure on the rotational population distribution, ratios of the perturbed to the unperturbed populations were calculated for the K' = 12 and 14 components as a function of pressure. To account for the intensity difference in normal spin doublets due to the statistical weights in the initial state, observed values of the $F_2(K)$ components were multiplied by the factor, $1 + 1/K$. For K' = 12 components, ratios of the perturbed to unperturbed populations decreased with increasing pressure from a value 0.8 at 0.55 torr to 0.5 at 20 torr. Similarly, ratios of K' = 14 components decreased from a value of 1.0 at 0.55 torr to 0.5 to 20 torr.

An explanation for observed population distributions in the presence of the rotational perturbation is based on the relative populations of the two perturbing electronic states and the effect of collisional transfer on pressure. The mechanism to be presented will be included in the general model for excitation of nitrogen in a helium afterglow outlined in Section 3.4.

3.3 Vibrational Population Distribution in the N_2^+ Emission Spectra

Distributions of population over the vibrational levels of the excited electronic states of the enhanced nitrogen spectra were measured from vibrational band intensities. The integrated intensity of the (v',v") band connected by an electric dipole transition is given by[17]

$$I_{v'v''} = N_{v'}A_{v'v''}E_{v'v''} \qquad (3.5)$$

where $N_{v'}$ is the relative population of the v' level, $A_{v'v''}$ the Einstein coefficient for spontaneous emission, and $E_{v'v''}$ the energy difference between the upper and lower levels. Vibrational population distributions can be obtained from measured intensities by Eq. (3.5). We are interested in the level populations relative to one another, where the measurement of peak height intensities is a good approximation to the integrated band intensities. Since measurements were made over a large wavelength range, the data were corrected for the spectral response of the apparatus.

Representative intensities and populations are given in Table 3.1 for the different vibrational levels of excited electronic states of N_2^+ produced in the afterglow of the d.c. discharge flow system at a downstream pressure of 0.6 torr. Particular attention is directed to the population distribution over the vibrational levels of the $B^2\Sigma$ state of N_2^+ as given in Figs. 3.11 thru 3.13 for different experimental conditions. Relative values of $I_{v'v''}/A_{v'v''}E_{v'v''}$ are plotted against E_v according to Eq. (3.5) for v' = 0 to 7. Values

for the Einstein transition probabilities were obtained from Nicholls[17]. In each graph, the broken line represents the calculated population distribution over the first four levels according to the Franck-Condon factors for excitation from the v" = 0 level of the ground state of N_2[18]. The relative effect on the population distribution by applying a microwave field to the afterglow upstream from the nitrogen emission is given in Fig. 3.11. For the d.c. discharge-afterglow system operated at 0.6 torr, curve (a) represents the condition of zero field and (b) corresponds to an applied field of 2.4 watts. Relative populations were normalized to 100 for the v' + 0 level in each case. The different slopes for each curve suggests that two distinct processes are populating the vibrational levels; one nearly following the broken line curve for the first three levels, and the other populating the higher vibrational levels with an infinite vibrational temperature. The overall effect of the microwave field was to decrease the vibrational populations of the higher levels with v' > 2 relative to the v' = 0 level.

Hydrogen added to the afterglow upstream from the nitrogen emission has been observed to decreased the populations in the v' = 0 and 1 levels relative to the higher vibrational levels and is reproduced in Fig. 3.12. Curve (a) represents the condition for zero H_2 flow and is identical to (a) in Fig. 3.11. Curve (b) corresponds to a H_2 flow rate of 5×10^{18} sec^{-1} where the relative population for the v' = 7 level was chosen to be equal to the same value for (a).

The effect of pressure on the relative vibrational population distributions observed in the afterglow of the microwave discharge is given in Fig. 3.13. Curve (a) was observed for a downstream pressure of 0.7 torr, (b) corresponds to 2 torr, and (c) represents 20 torr where the relative values for the population were set equal to 100 for v' = 0. At low pressures the observed populations suggest that only one mechanism is operative since the higher vibrational levels are essentially absent and the population curve is linear in E_v. At 2 torr, represented by (b), the observed populations are similar to the (a) curves in Figs. 3.11 and 3.12 indicating a two mechanism process. For high pressure, curve (c) is similar to (b) except for the abnormally low populations for the v' = 1, 3, and 5 levels. The odd levels v' = 1, 3, and 5 are those levels in which rotational perturbations have been observed[19].

The fractional change in intensity I/I_o, of selected vibrational bands of the excited N_2^+ and NI emission have been measured and are shown in Fig. 3.14 as a function of incident microwave power applied to the afterglow. I_o is the observed intensity for zero field where the ratio I/I_o is unity at zero power. Curve (a) represents the intensity decrease for the (0,3) band of the $B^2\Sigma - X^2\Sigma$ system of N_2^+, (b) gives the relative change of the (3,0), (4,1) and (5,2) bands of the $A^2\Sigma - X^2\Sigma$ system; (c) fits the data for the (4,7), (5,8), (6,9), (7,10) and (15,17) bands of the $B^2 - X^2$ system; (a0 is a measure of the NI emission at 7468Å.

Observed intensities for selected bands and atomic lines of the enhanced nitrogen spectrum are reported in Table 3.1. The relative intensities were corrected for the spectral response of the apparatus and normalized to give 1000 for the (0,3) band of the first negative system. Relative populations were calculated from Eq. (3.5) for the representative bands having available transition probabilities.

3.4 Summary and Model for Excitation of N_2 by Energetic Helium

Possible mechanisms for excitation of nitrogen in a helium afterglow are: (1) direct excitation from the ground state by electron impact, (2) vacuum ultraviolet photon absorption, (3) radiative transitions, and (4) inelastic collisions with energetic helium species. The first three methods are negligible compared to (4) for reasons to be discussed in detail in Chapter 4. In the study of excitation mechanisms included in (4), the following energetic helium species are to be considered: He^m, He^+, He_2^m, and He_2^+.[20]

Assignment of reaction mechanisms involving the energetic helium and nitrogen reactants are required to account for the observed excited state nitrogen products. Potential energy curves for the electronic states of N_2^+ are reproduced in Fig. 3.15 according to Ogawa[21], and energies for the energetic helium species are included. He^m has an energy of 19.81 eV and He^+ has a value of 24.58 eV. He_2^+ and He_2^m present a range of available energies[20] of several eV extent centered about 19.7 and 15.5 eV respectively. Molecular helium energies available for reaction in which the molecule undergoes

dissociation is equal to the absolute energy of the ground vibrational level of the excited state minus the repulsive energy of the two helium atoms for the internuclear separation existing at the time of deexcitation. Potential energies used for the excited states of molecular helium were obtained from Mulliken[22]. The repulsive energy as a function of internuclear distance between the two neutral helium atoms was taken from the data of Phillipson[23]. Assignment of the internuclear distance upon deexcitation of the molecular helium and the calculation of the available energies were made by applying the Franck-Condon principle to the He_2 potential curves similar to the method used for determining the intensity distribution in a continuous emission spectrum[13]. If a significant number of energetic helium molecules are in excited vibration levels at the time they enter into a reaction, the range of available energy would be much larger than that shown in Fig. 3.15.

According to Massey's adiabatic hypothesis[24] the rates of exothermic charge transfer reactions involving He^+ and He_2^+ are expected to be small unless the following inequality holds

$$a\Delta E/hv < 1 \qquad (3.6)$$

where a is the characteristic distance of interaction ($\sim 8\mathring{A}^2$), v is the relative velocity of the colliding pair of reactants with a value of about 1.3×10^5 cm/sec for He and N_2 at $300^\circ K$, and ΔE is the energy defect of the reaction. For thermal energy reactions considered in the present work the adiabatic principle requires that ΔE be small. This 'resonance' nature of the charge transfer reaction

is useful in analyzing the expected excited state energies of the reaction products.

To aid in assignment of reaction mechanisms responsible for the selectively excited nitrogen spectrum, the effect of the microwave and H_2 quenching reported in Sections 3.2 and 3.3 was analyzed. In general, the effect of applying a microwave field to the afterglow was to decrease He^+ and He_2^+ concentrations relative to He^m and He_2^m in the reaction region while addition of H_2 to the afterglow decreased He^m concentrations relative to remaining energetic helium species[25].

The widely accepted rate determining path for the reaction containing He^+ is the dissociative charge transfer reaction[25]

$$He^+ + N_2 \rightarrow He + N(^4S^o) + N^+(^3P) \qquad (3.7)$$

which is likely a complex reaction where the first step is a direct charge transfer to the $v' = 4$ level of the $C^2\Sigma$ state of N_2^+ followed by predissociation by the $^4\Pi$ state. No resulting emission is expected to occur for reaction (3.7) since the nitrogen atom and ion products are left in their respective ground states. Observation of the possible $C^2\Sigma - X^2\Sigma$ second negative system excited by direct charge transfer with He^+ was not attempted because the system occurs in the vacuum ultraviolet region which was not observable with the present apparatus.

A likely mechanism for excitation of the atomic nitrogen emission shown in Fig. 3.5 is the radiative electron-ion recombination

reaction.

$$N^+(^3P) + e \rightarrow N^*(^2P, ^4P, ^4D) \rightarrow N + h\nu \qquad (3.8)$$

where the intermediate reactant, $N^+(^3P)$ is the product of reaction (3.7). The application of a microwave field to the afterglow causes the NI intensity to decrease rapidly as shown by curve (b) in Fig. 3.14 by both decreasing the rate of electron-ion recombination[27] in (3.8) and by decreasing the He^+ reactant in (3.7) by ambipolar diffusion loss to the walls.

The dominate mechanism populating the first two vibrational levels of the $B^2\Sigma$ state is attributed to the Penning reaction

$$He^m + N_2 \rightarrow He + N_2^+(B^2\Sigma, v'=0) + e \qquad (3.9)$$

The distribution of population over the vibrational levels follow the Franck-Condon factors for excitation from the ground state[28] as indicated by the initial slope of the curves in Figs. 3.11 to 3.13. Application of a microwave field to the afterglow leaves the He^m concentration relatively unchanged which is consistent with the negligible decrease observed in the (0,3) band intensity for curve (a) in Fig. 3.14. Addition of H_2 to the afterglow upstream from the nitrogen emission is expected to cause a more rapid decrease in He^m compared to the other energetic helium species[25]. This effect is seen in curve (b) of Fig. 3.12 by the order of magnitude decrease of the $v' = 0$ level population relative to the levels with $v' > 2$ upon addition of H_2.

The wide range of He_2^+ energy available for reaction is centered between the $v' = 3$ and 4 levels of the $B^2\Sigma$ state of N_2^+ at 19.7 eV. The primary mechanism populating the $v' > 2$ levels of the $B^2\Sigma$ state

is the charge transfer reaction,

$$He_2^+ + N_2 \rightarrow 2He + N_2^+(B^2\Sigma,\ v'>2) \qquad (3.10)$$

The resulting distribution of population over the v' = 2 to 7 levels is represented by the slope of the (a) curves in Figs. 3.11 and 3.12 corresponding to an infinite vibrational temperature, i.e., the levels are equally populated. The rates of populating v' = 0,1,2, and 3 by reaction (3.9) decrease rapidly with increasing v due to the Franck-Condon factors for excitation from the ground state; the v' = 2 level being 10^{-3} that for the v' = 0 level. This is the reason that although the He^m concentration is much larger than the He_2^+ reaction (3.10) becomes important for populating the levels beginning with v' = 2. The equal population distribution for the levels v' = 2 to 7 corresponding to an energy range of about 1.3 eV is attributed to the non-symmetrical charge transfer reaction (3.10). By requirements of the adiabatic principle predicting an energy resonance, equal populations of the reaction product for the large energy range presupposes that a comparable energy range is available in the reactant He_2^+. This is not out of line for He_2^+ potential curves. The probability that a He_2^+ molecule with a given energy will undergo an inelastic collision with N_2 is a function of the He_2^+ internuclear distance at the time of the collision. The repulsive ground state He_2 potential curve rapidly changes over the range of internuclear distance corresponding to the non-zero probability density distribution of the ground vibrational level of He_2^+. Therefore the range of internuclear distance over which the He_2^+ reacts and becomes deexcited corresponds to an energy range of 1 to 2 eV.

Observed tail bands originating in the v' = 13, 14, and 15 levels of the $B^2\Sigma$ state are likewise attributed to the charge transfer reaction (3.10). An energy difference of approximately 2.3 eV exists between the v' = 14 level of the $B^2\Sigma$ state and the calculated He_2^+ energy 19.7 eV. The vibrational populations for the v' = 13, 14, and 15 levels are approximately one order of magnitude less than those for the v' = 2 to 7 levels as reported in Table 3.1 for the same experimental conditions and are consistent with Eq. (3.6) for the large energy defect of approximately 2.3 eV.

The population distribution in the high vibrational levels of the $B^2\Sigma$ state for the energy defect of 2.3 eV suggests a mechanism in which the He_2^+ molecules are in excited vibrational levels at the instance of inelastic colliding with N_2. In addition to energetic considerations, the observed tail bands exhibit a decrease in intensity upon application of a microwave field with a slope identical to that for the (4,7) (5,8) (6,9) and (7,10) bands given by curve (c) in Fig. 3.14.

Excitation of the weakly appearing $D^2\Pi$ - $A^2\Pi$ Janin d'Incan bands can be attributed to the same charge-transfer reaction (3.10) with He_2^+. The energy defect for the reaction calculated for the v' = 0 to 8 levels of the $D^2\Pi$ state amounts to a range of 2 to 3 eV. The observed low populations relative to the other excited state products of reaction (3.10) is consistent with Eq. (3.6) for the large energy defect. In the microwave quenching experiment, Fig. 3.14, the (5,3) and (8,6) band intensities appeared to follow curve (c)

but with less certainty because of their relatively weak intensities.

The readily occurring bands of the $A^2\Pi$ - $X^2\Pi$ Meinel system are excited by the Penning-ionization reaction involving He_2^m,

$$He_2^m + N_2 \rightarrow 2He + N_2^+(A^2\Pi,\ v' = 2,3,4) + e \qquad (3.11)$$

The same arguments used to estimate the available energy range for He_2^+ apply to reactions with He_2^m. The He_2^m energy range is centered near the v' = 0 level of the $X^2\Sigma$ state of N_2^+ at 15.5 eV and is labeled in Fig. 3.15. The energy defect of reaction (3.11) corresponds to a range of 1.5 to 2.2 eV which is within the estimated energy available from exothermic reactions with He_2^m. The presence of the light electron in the products relaxes the strict energy resonance requirement as for He^m reactions since the excess energy can be absorbed in the kinetic energy of the electron. From Table 3.1, the distribution of population over the observed v' = 3, 4, and 5 vibrational levels of the $A^2\Pi$ state follow the Franck-Condon factors for excitation from the v" = 0 level of the ground state[28]. The relative intensities of the (3,0), (4,1) and (5,2) bands of the Meinel system was observed to decrease with an applied microwave field according to curve (b) in Fig. 3.14. This appreciable decrease indicates a corresponding decrease in the afterglow He_2^m concentration. The slope of (b) being less than (c) for He_2^+ reactions and greater than (a) for He^m reactions can be explained from a consideration of the He_2^m production mechanisms to be discussed in detail in Chapter 4.

$$He_2^+ + e \rightarrow He_2^* \rightarrow He_2^m + h\nu \qquad (3.12)$$

and

$$He^m + 2He \rightarrow He_2^m + He \qquad (3.13)$$

Contribution to the He_2^m concentration by reaction (3.12) rapidly decreases by applying a microwave field to the afterglow[27] while reaction (3.13) and the already present He_2^m concentration would be only slightly affected. The overall effect would result in a decrease in He_2^m similar to that observed for curve (b) in Fig. 3.14.

Definite assignments of excitation mechanisms for the weak $B^3\Pi$ - $A^3\Sigma$ first positive system and $C^3\Pi$ - $B^3\Pi$ second positive system of N_2 were not made. The general method of analysis applied to the N_2^+ band systems could not be used because of the weak intensities involved.

Intensity anomalies for the rotational population distribution in the (1,0) band observed as a function of pressure in Fig. 3.10 are a result of the reported rotational perturbation. Likewise, the abnormally low vibrational populations for the v' = 1, 3, and 5 levels reported in Fig. 3.13 at high pressure dorrespond to those vibrational levels of the $B^2\Sigma$ state whose rotational terms are perturbed by nearly degenerate levels of the $A^2\Pi$ state. A more careful analysis of the relative intensity distributions of the perturbed levels as a function of pressure gives information about the mechanisms populating the v' = 1 level of the $B^2\Sigma$ and $A^2\Pi$ states.

The dominate mechanism populating the v' = 1 level of $B^2\Sigma$ has been attributed to the Penning ionization reaction (3.9) with He^m governed by the Franck-Condon factors for excitation from the v" = 0 level of the ground $X^1\Sigma$ state of N_2. However no similar data is

available for the excitation of the perturbing v' = 11 level of the $A^2\Pi$ state. From the potential curves in Fig. 3.15, a simple analysis of the v' = 11 level excitation by a Penning reaction with He^m from the ground state according to the Franck-Condon principle indicates a less favorable process with smaller overlap integrals. This leads one to assume the steady state population of the v' = 1 level of $B^2\Sigma$ is greater than the v' = 11 level of $A^2\Pi$ by at least a factor of two but more like an order of magnitude.

The observed intensity dependence on pressure for the K' = 12 and 14 rotational lines of the (1,0) band has been reported in Section 3.2 and Fig. 3.10. The intensity decrease of the perturbed $F_2(K)$ components relative to the unperturbed $F_1(K)$ with increasing pressure can be explained by an increase in collisions of the second kind among the molecules in the perturbed levels[29]. Therefore with the assumed population distribution being greater for the $B^2\Sigma$ state the effect of the inelastic collisions appear to smooth out the population differences between the mutually perturbed components faster than the unperturbed resulting in the observed decrease in $F_2(K)$ intensity relative to $F_1(K)$. An identical mechanism would then be responsible for the abnormally low populations in the K' = 1 and 2 levels for high pressure even though the perturbed and unperturbed components are unresolved.

TABLE 3.1

NITROGEN SPECTRUM EXCITED IN A HELIUM AFTERGLOW

REPRESENTATIVE TRANSITIONS AND INTENSITIES

Transition	Band	Wavelength, (Å)	$I_{v'v''}$	$N_{v'}$
$B^2\Sigma - X^2\Sigma$	0,3	5228.3 V	1000	880
	1,4	5148.8 V	50	140
	2,5	5076.5 V	17	28
	3,6	5012.4 V	25	34
	4,7	4958.0 V	26	31
	5,8	4913.2 V	28	35
	6,9	4881.7 V	24	35
	7,10	4864.4 V	24	36
	13,15	4743.1 R	8	6
	14,16	4850.3 R	14	2
	15,17	4969.3 R	6	3
$A^2\Pi - X^2\Sigma$	3,0	6853.0 R	23	25
	4,1	7036.8 R	32	10
	5,2	7239.9 R	24	5
$D^2\Pi - A^2\Pi$	5,3	2418.5 R	1	
	7,5	2543.4 R	2	
$B^3\Pi - A^3\Sigma$	2,0	7753.7 V	2	
$C^3\Pi - B^3\Pi$	0,0	3371.4 V	.5	
NI $3p\,^4S^o - 3s\,^4P$		7423.63	14	
		7442.28	29	

III REFERENCES

1. A. C. G. Mitchell & M. W. Zemanski, Resonance Radiation and Excited Atoms, Cambridge Univ. Press, England 1934.
2. R. W. Nicholls, J. Quant. Spect. Rad. Transfer, 2, 433 (1962).
3. W. C. Martin, J. Res. NBS A64, 19 (1960).
4. B. Rosen, Des Longueurs D'Onde Caracteristiques des Bandes D'Emission et D'Absorption des Molecules Diatomiques, Hermann and Co. Depositaries, Paris, 1952.
5. M. L. Ginter, J. Chem. Phys. 42, 358 (1965); J. Mol. Spect. 17, 224 (1965) J. Mol. Spect. 18, 321 (1965); and J. Chem. Phys. 45, 248 (1966).
6. Y. Tanaka, T. Namioka, and A. S. Jursa, Can. J. Phys, 39, 1138 (1961).
7. J. Janin and J. d'Incan, C. R. Acad. Sci. Paris 246, 3436 (1958).
8. L. Wallace, Astrophys. J. Supp. 6, 445 (1962); Astrophys. J. Supp. 7, 165 (1962).
9. A. B. Meinel, Astrophy. J. 113, 583 (1951).
10. A. E. Douglas, Astrophys. J. 117, 380 (1953).
11. P. J. Nawrocki & R. Papa, Atmospheric Processes, Prentice-Hall, Inc., New Jersey 1963, p. 4-18.
12. A. B. Meinel, Astrophys. J., 114, 431 (1951).
13. M. Fassbender, Z. Physik 30, 73 (1924).
14. D. Coster and H. H. Brons, Z. Physik 70, 492 (1931).

15. For a complete discussion see G. Herzberg, Molecular Spectra and Molecular Structure, I., D. van Nostrand Co., Inc., New York, 1950.

16. H. P. Broida and H. J. Kostkowski, J. Chem. Phys. 25, 676 (1956).

17. R. W. Nicholls, Ann. de Geophys., 20, 114 (1964).

18. R. W. Nicholls, J. Quant. Spect. Rad. Transfer, 2, 433 (1962).

19. A. Lofthus, The Molecular Spectrum of Nitrogen, Spectroscopic Report 2, Univ. of Oslo, Norway, 1960.

20. See Chapter 5 and C. B. Collins and W. W. Robertson, J. Chem. Phys. 40, 701 (1964).

21. M. Ogawa, Private Communication

22. R. S. Mulliken, Phys. Rev. 136, A962 (1964).

23. P. E. Phillipson, Phys. Rev. 125, 1981 (1962).

24. H. S. W. Massey & E. H. S. Burhop, Electronic and Ionic Impact Phenomena, Clarendon Press, Oxford, England, 1952.

25. See Section 6 and Tables 6.1 thru 6.4.

26. F. C. Fehsenfeld, A. L. Schmeltekopf, P. D. Golden, H. I. Schiff, and E. E. Ferguson, J. Chem. Phys. 44, 4087 (1966).

27. P. J. Severin, J. Quant. Spect. Rad. Transfer, 4, 763 (1964).

28. W. W. Robertson, J. Chem. Phys. 44, 2456 (1966).

29. H. E. Radford and H. P. Broida, J. Chem. Phys. 38, 644 (1963).

III Figure Legend

3.1 Nitrogen spectra excited in a helium afterglow. The $D^2\Pi$ - $A^2\Pi$ Janin d'Incan system of N_2^+. Huet f/3.5 quartz prism spectrograph, 45/10 min, 103a-O Eastman Kodak plates.

3.2 Pure helium and nitrogen spectra excited in a helium afterglow. The $B^2\Sigma$ - $X^2\Sigma$ first negative system of N_2^+ and weakly occurring $C^3\Pi$ - $B^3\Pi$ second positive system of N_2. Bass Kessler f/10 quartz grating spectrograph, helium - 8 min, nitrogen - 30 sec, 103a-O Eastman Kodak plates.

3.3 Pure helium and nitrogen spectra excited in a helium afterglow. The $B^2\Sigma$ - $X^2\Sigma$ first negative system of N_2^+. Bass Kessler f/5.6 grating spectrograph, helium 4 min, nitrogen 1 min, 103a-F Eastman Kodak plates.

3.4 Pure helium and nitrogen spectra excited in a helium afterglow. The $B^2\Sigma$ - $X^2\Sigma$ first negative system and $A^2\Pi$ - $X^2\Sigma$ Meinel system of N_2^+. Bass-Kessler f/5.6 grating spectrograph, helium 4 min, nitrogen 4 min, 103a-F Eastman Kodak plates.

3.5 Nitrogen spectra excited in a helium afterglow. The $A^2\Pi$ - $X^2\Sigma$ Meinel system of N_2^+, weakly occurring $B^3\Pi$ - $A^3\Sigma$ first positive system of N_2 and NI transitions. Bass-Kessler f/5.6 grating spectrograph, 20 min, hypersensitized I-N Eastman Kodak plates.

3.6 Spectra of the (0,0) band of the $B^2\Sigma$ - $X^2\Sigma$ first negative system of N_2^+ excited in a helium afterglow. Fastie-Ebert

0.8 meter double-pass grating monochromator with 1200 l/mm grating and 10 micron slit width.

3.7 Spectra of the (1,0) band of the $B^2\Sigma$ - $X^2\Sigma$ first negative system of N_2^+ excited in a helium afterglow. Fastie-Ebert 0.8 meter double pass grating monochromator with 1200 l/mm grating and 10 micron slit width. Spin doublet components split by perturbation are labeled F_1 and F_2 and the extra line for K' = 13 by E.

3.8 [ln $I/g_n(K' + K'' + 1)$] values plotted against K" (K' +1) for the R-branch of the (0,0) band of the $B^2\Sigma$ - $X^2\Sigma$ first negative system of N_2^+ excited in a helium afterglow. (A) afterglow of a microwave discharge operated with an incident power of 17 watts and downstream pressure of 10 torr, (B) afterglow of a continuous d.c. discharge of 50 watts with a downstream pressure of 0.6 torr.

3.9 [ln $I/g_n(J' + J'' + 1)$] values plotted against $F_v(J')$ for the R-branch of the perturbed (1,0) band of $B^2\Sigma$ - $X^2\Sigma$ first negative system of N_2^+ excited in a helium afterglow. Circles represent the unresolved and unperturbed $F_1(J)$ components and triangles the perturbed $F_2(J)$. The extra line is marked E. Afterglow of a continuous d.c discharge of 50 watts with downstream pressure of 0.6 torr.

3.10 [ln I/g_n $(J' + J'' + 1)$] values plotted against $F_v(J)$ for the R-branch of the perturbed (1,0) band of $B^2\Sigma$ - $X^2\Sigma$ first negative system of N_2^+ excited in a helium afterglow. Circles

represent the unresolved and unperturbed $F_1(J)$ components and triangles the perturbed $F_2(J)$. The extra line is marked E. After glow of a microwave discharge at 17 watts with a downstream pressure of 0.6 torr.

3.11 Relative populations $\ln[I_{v'v''}/A_{v'v''}E_{v'v''}]$ of the vibrational levels in the $B^2\Sigma$ state of N_2^+ plotted against $E_{v'}$. The broken line is the calculated distribution according to the Franck-Condon principle for excitation from the ground state. Afterglow of the continuous d.c. discharge with a downstream pressure of 0.6 torr; (a) zero field, (b) microwave field of 2.4 watts applied to the afterglow.

3.12 Relative populations $\ln[I_{v'v''}/A_{v'v''}E_{v'v''}]$ of the vibrational levels in the $B^2\Sigma$ state of N_2^+ plotted against $E_{v'}$. The broken line is the calculated distribution according to the Franck-Condon principle for excitation from the ground state. Afterglow of the continuous d.c. discharge with a downstream pressure of 0.6 torr; (a) zero H_2 flow, (b) H_2 added to the afterglow at flow rate of 5×10^{18} sec^{-1}.

3.13 Relative populations $\ln[I_{v'v''}/A_{v'v''}E_{v'v''}]$ of the vibrational levels in the $B^2\Sigma$ state of N_2^+ are plotted against $E_{v'}$. Afterglow of the microwave discharge; (a) downstream pressure 0.7 torr, (b) 2 torr, (c) 20 torr.

3.14 The fractional change in nitrogen emission intensity excited in a helium afterglow plotted against the microwave power applied to the afterglow. Afterglow of the d.c. discharge

with a downstream pressure of 0.6 torr; (a) (0,3) band of the $B^2\Sigma$ - $X^2\Sigma$ system of N_2^+, (b) (3,0), (4,1) and (5,2) bands of the $A^2\Pi$ - $X^2\Sigma$ system, (c) (4,7), (5,8), (6,9), (7,10) and (15,17) bands of the $B^2\Sigma$ - $X^2\Sigma$ system and (7,5) band of the $D^2\Pi$ - $A^2\Pi$ system, (d) NI lines at 7442.28 and 7423,63Å.

3.15 Potential energy curves for the electronic states of N_2^+. Allowed electric dipole transitions and available energies for the energetic helium species are given.

N_2^+ $D\ ^2\Pi - A\ ^2\Pi$

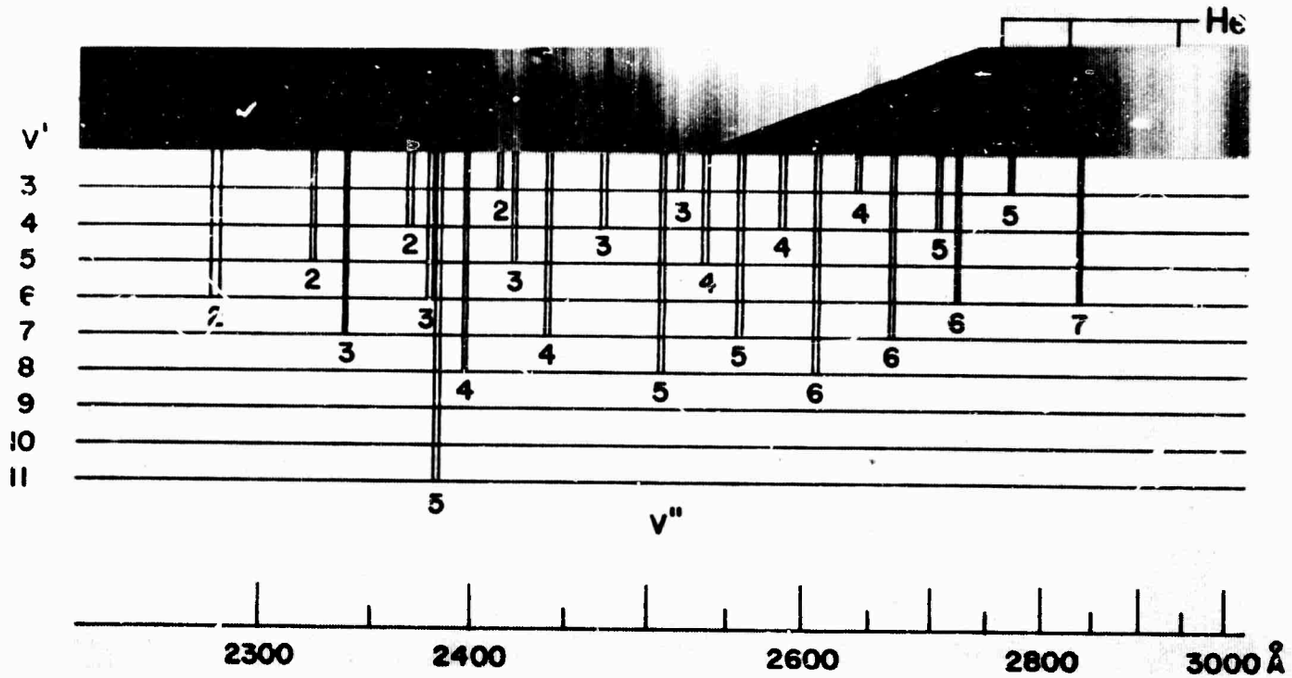

FIG 3.1

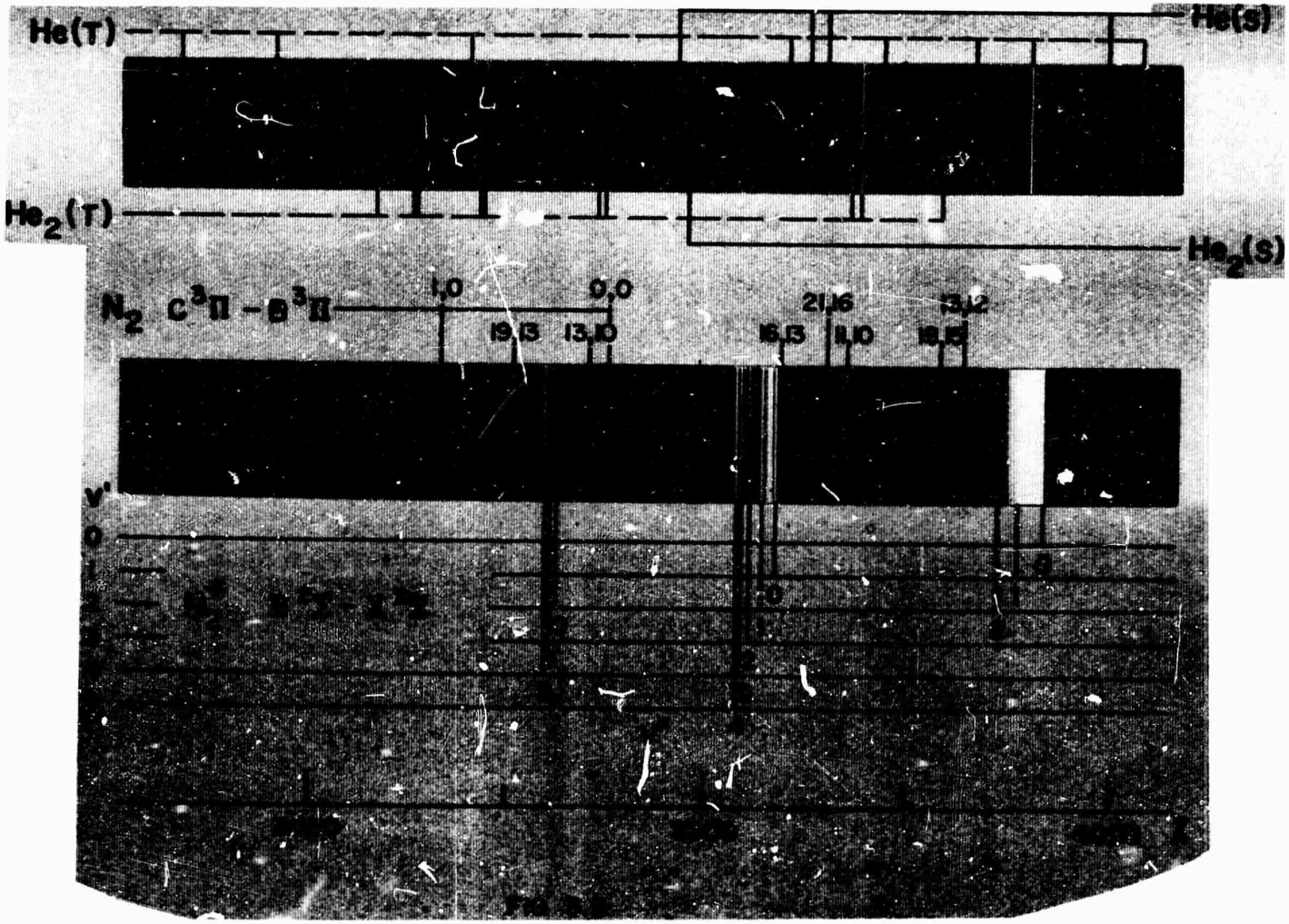
He(T)
He(S)
He2(T)
He2(S)
N2 C3Π – B3Π
1,0
0,0
19,13
13,10
21,16
16,13
11,10
13,12
18,15
v'
0

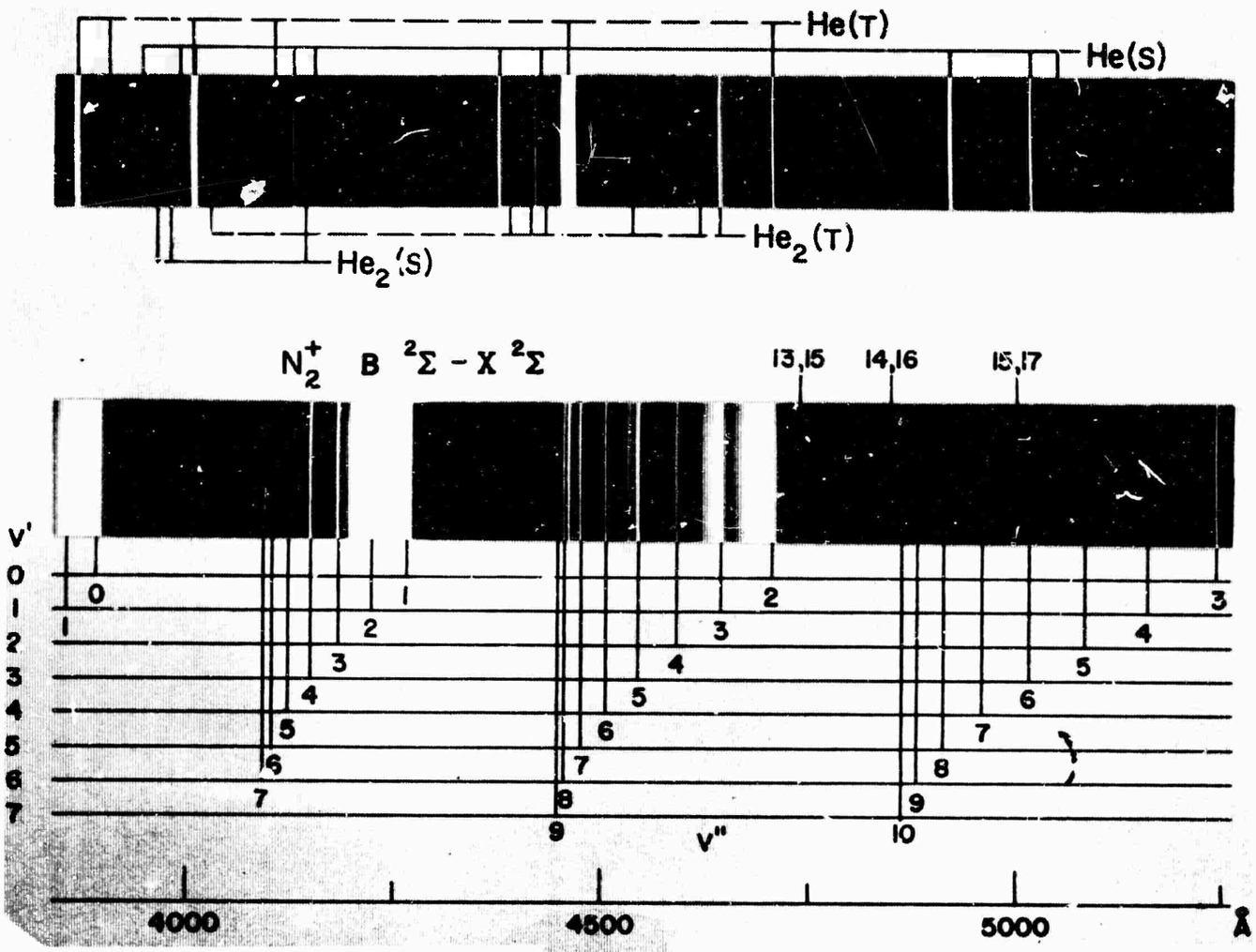

FIG 3.3

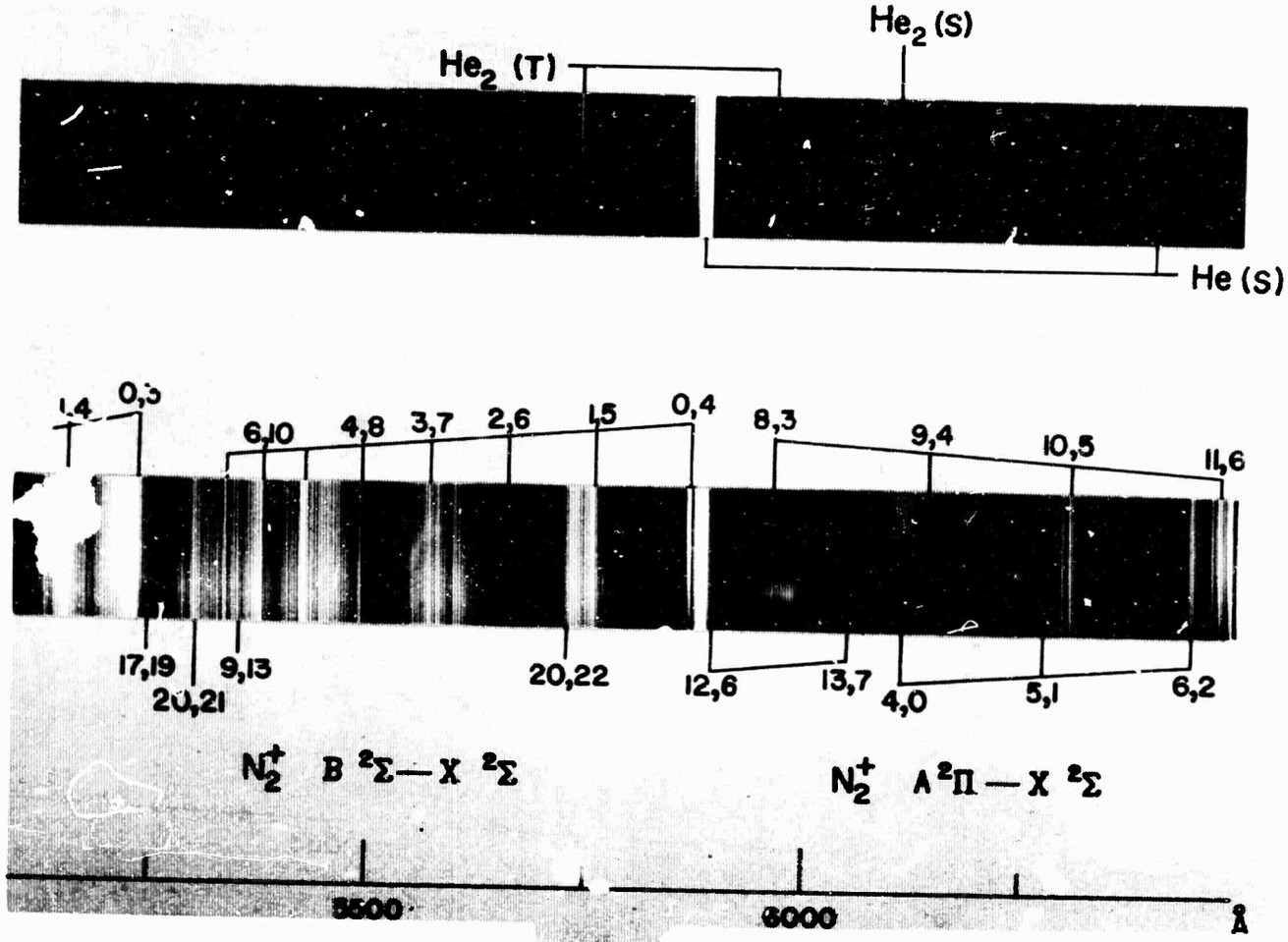
He2 (T)
He2 (S)
He (S)
1,4
0,5
6,10
4,8
3,7
2,6
1,5
0,4
8,3
9,4
10,5
11,6
17,19
20,21
9,13
20,22
12,6
13,7
4,0
5,1
6,2
N2+ B 2Σ — X 2Σ
N2+ A 2Π — X 2Σ
3500
4000
Å

FIG 3.4

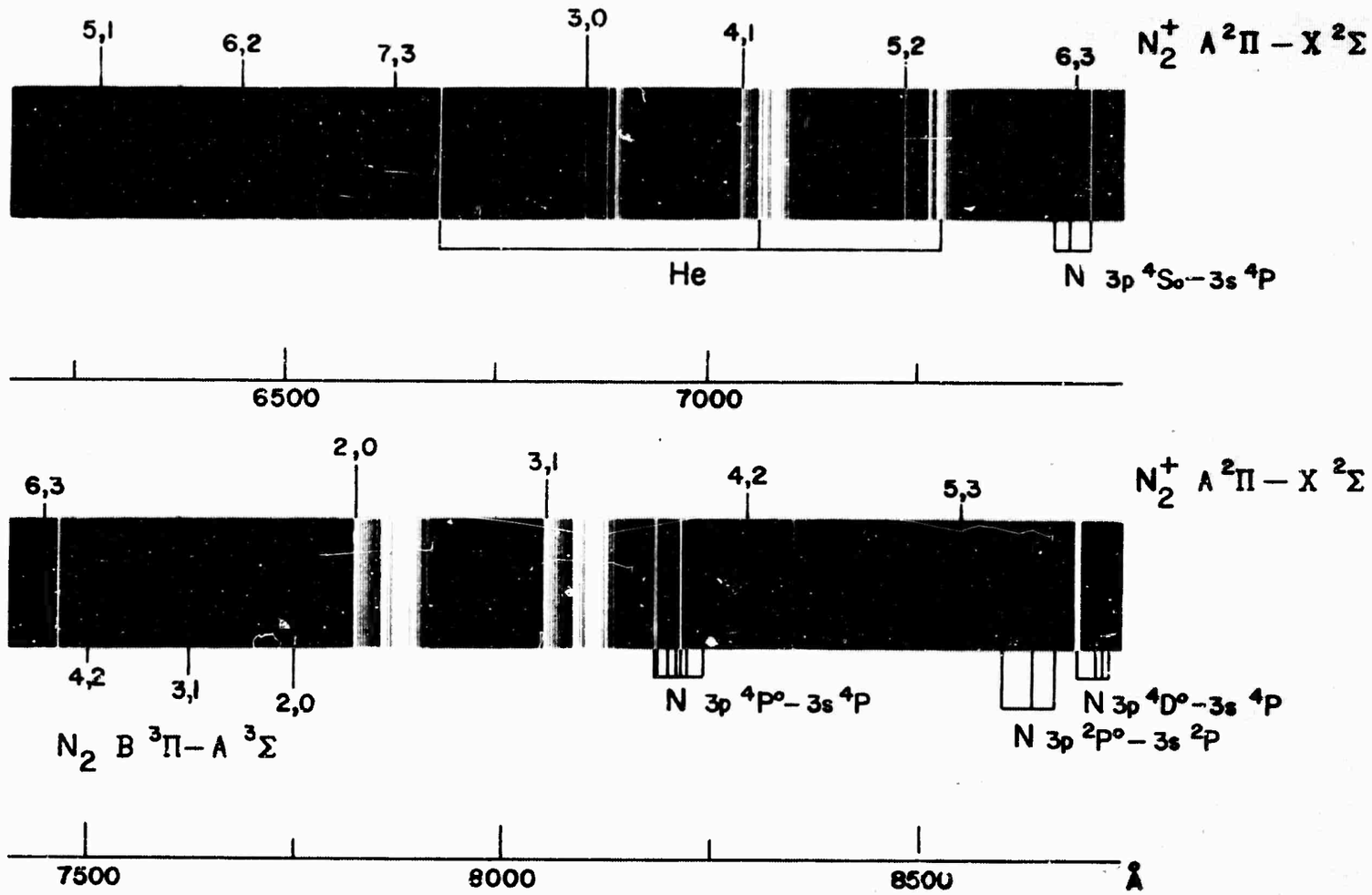
5,1
6,2
7,3
3,0
4,1
5,2
6,3
N_2^+ $A\,^2\Pi - X\,^2\Sigma$
He
N $3p\,^4S_0 - 3s\,^4P$
6500
7000
6,3
2,0
3,1
4,2
5,3
N_2^+ $A\,^2\Pi - X\,^2\Sigma$
4,2
3,1
2,0
N_2 $B\,^3\Pi - A\,^3\Sigma$
N $3p\,^4P^o - 3s\,^4P$
N $3p\,^4D^o - 3s\,^4P$
N $3p\,^2P^o - 3s\,^2P$
7500
8000
8500
Å

FIG 3.5

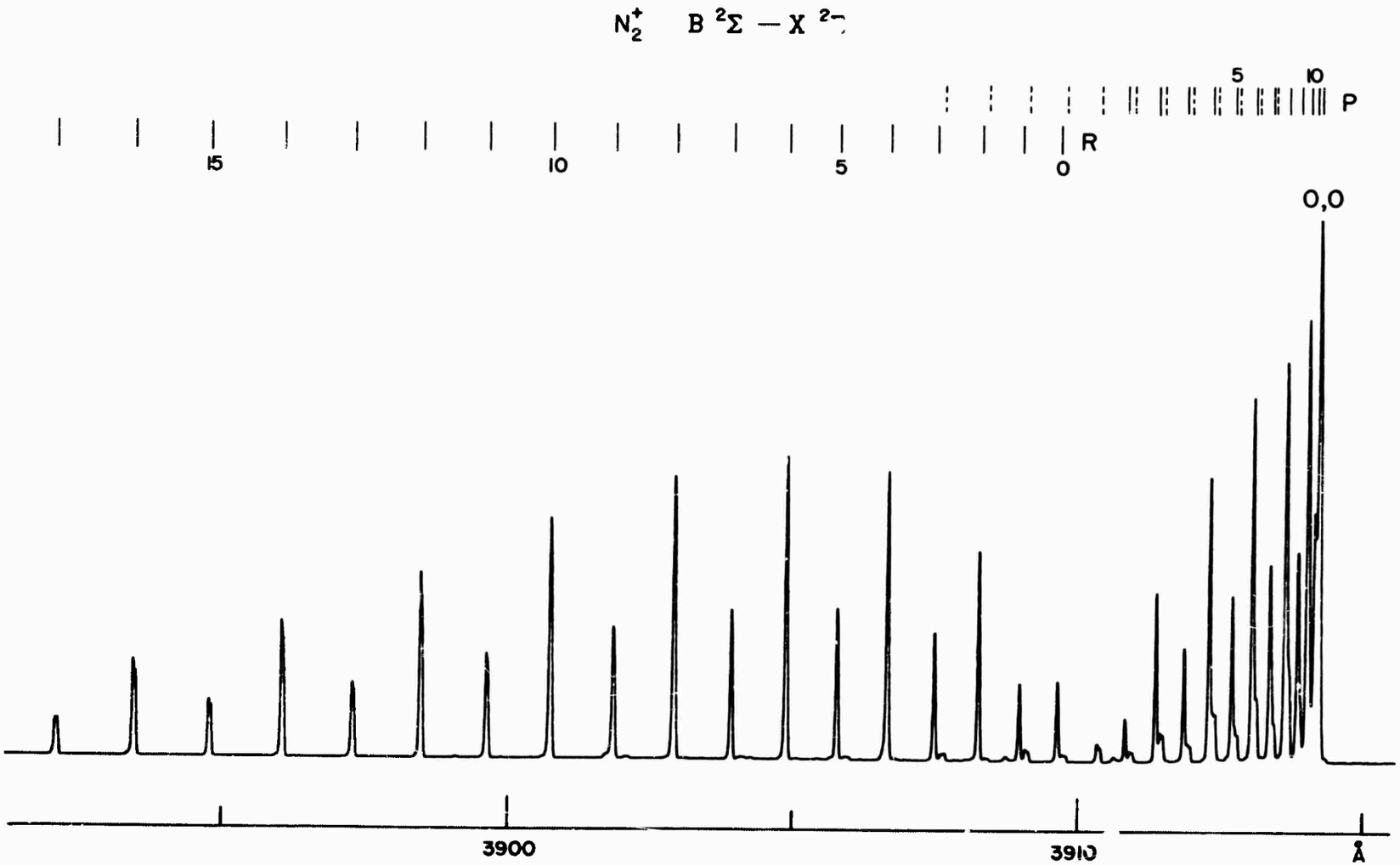

FIG 3.6

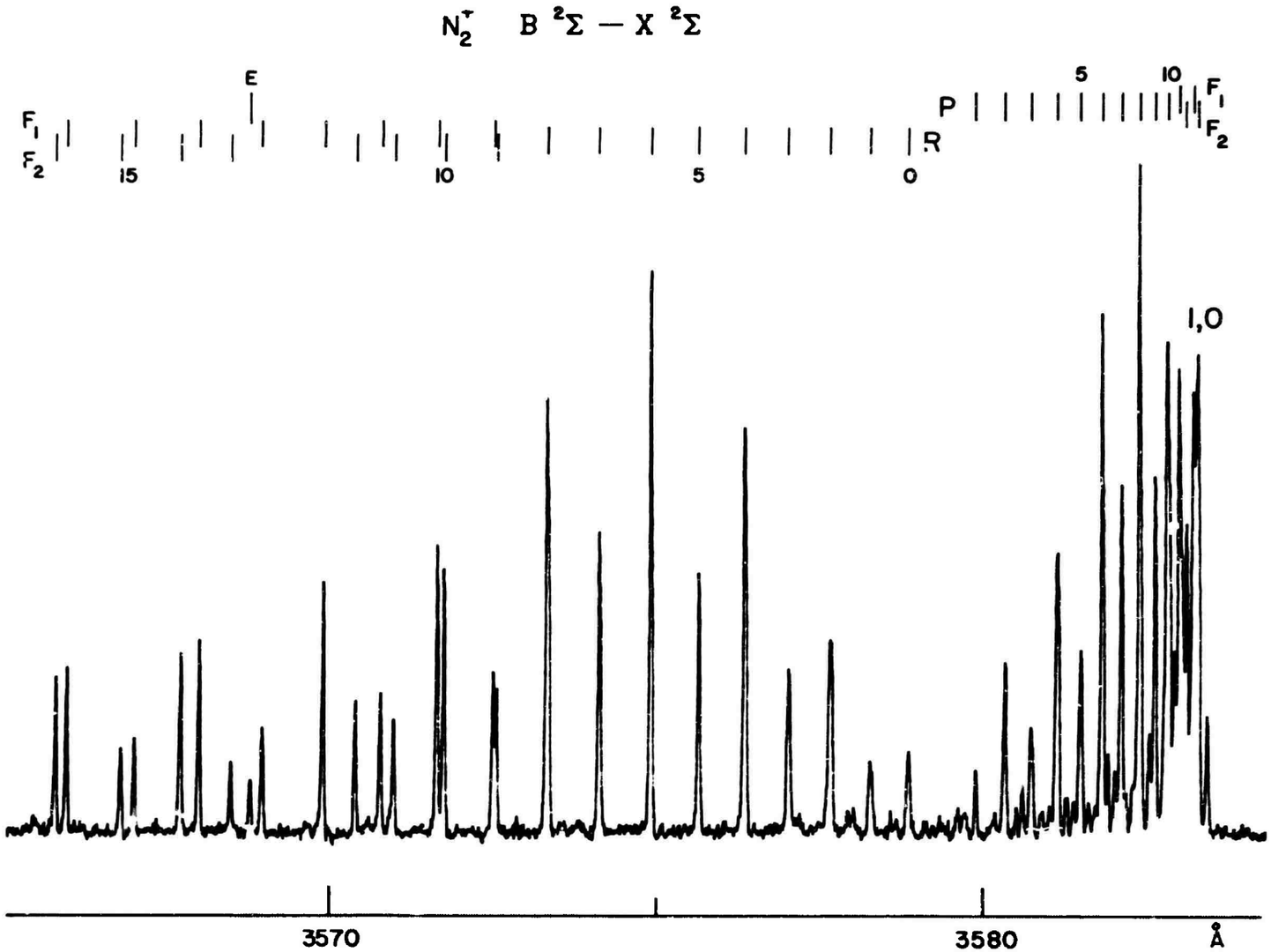

FIG 3.7

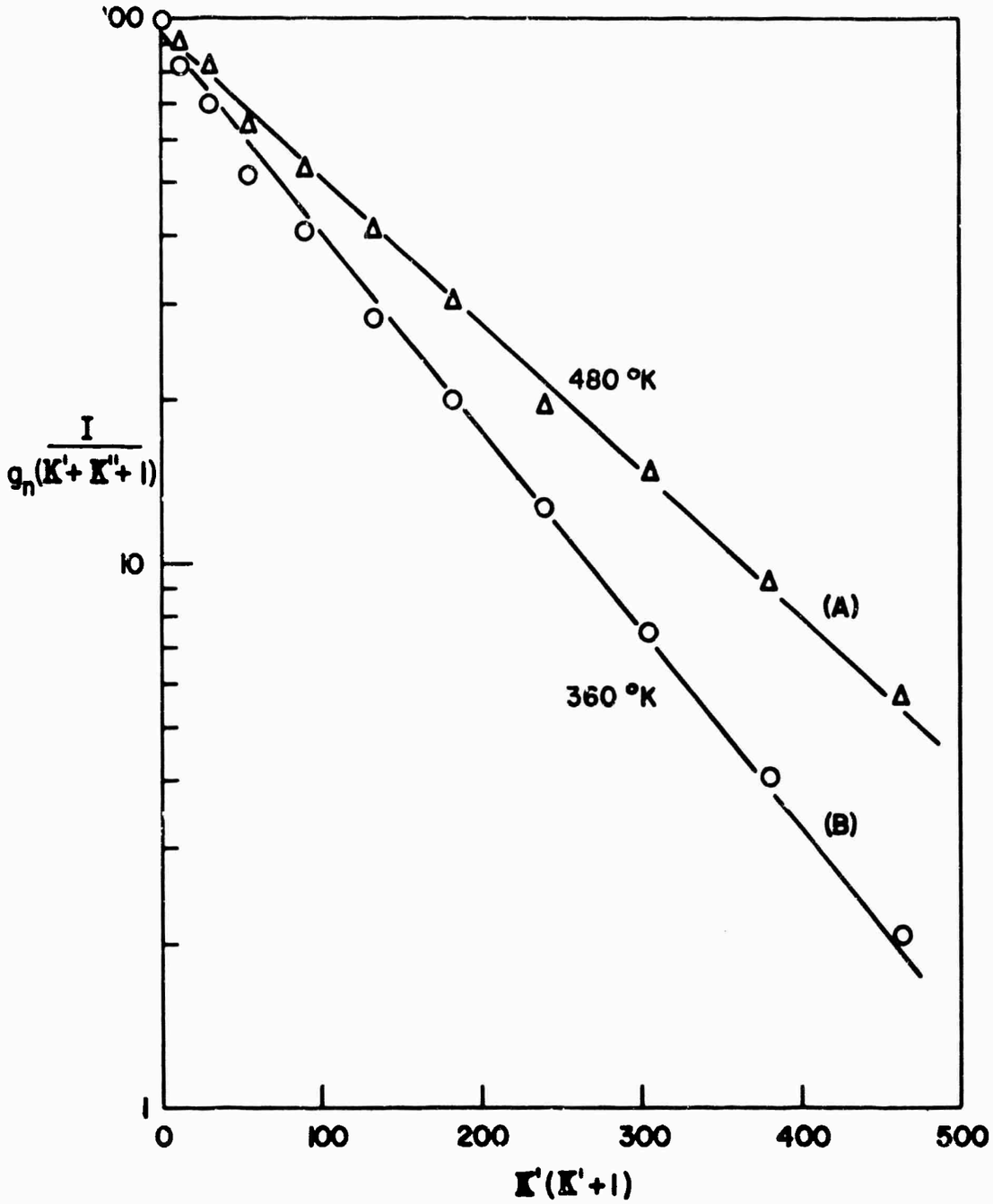

FIG 3.8

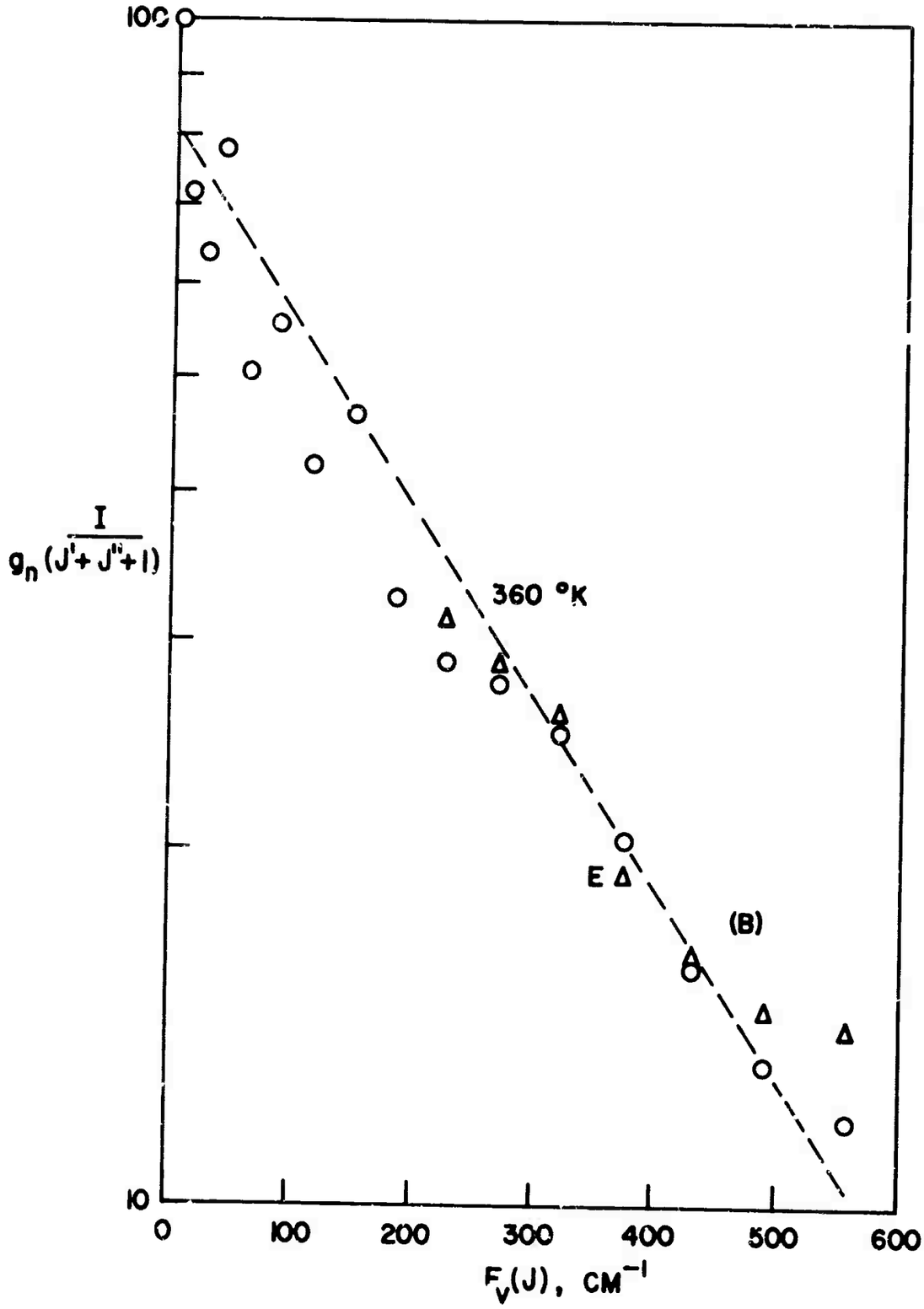

FIG 3.9

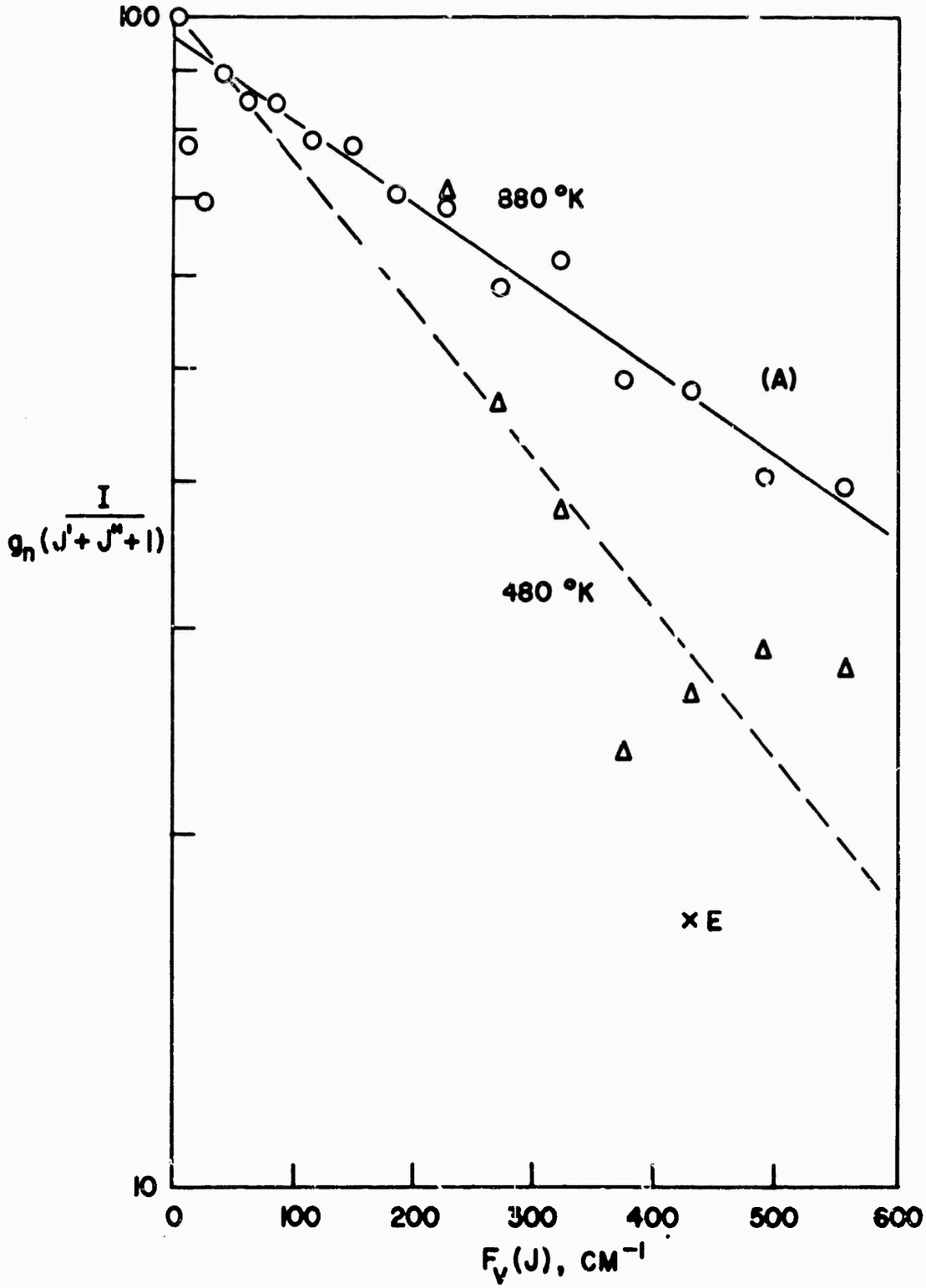
100
10
0
100
200
300
400
500
600
880 °K
480 °K
(A)
× E
$\frac{I}{g_n(J'+J''+1)}$
$F_v(J)$, CM^{-1}

FIG 3.10

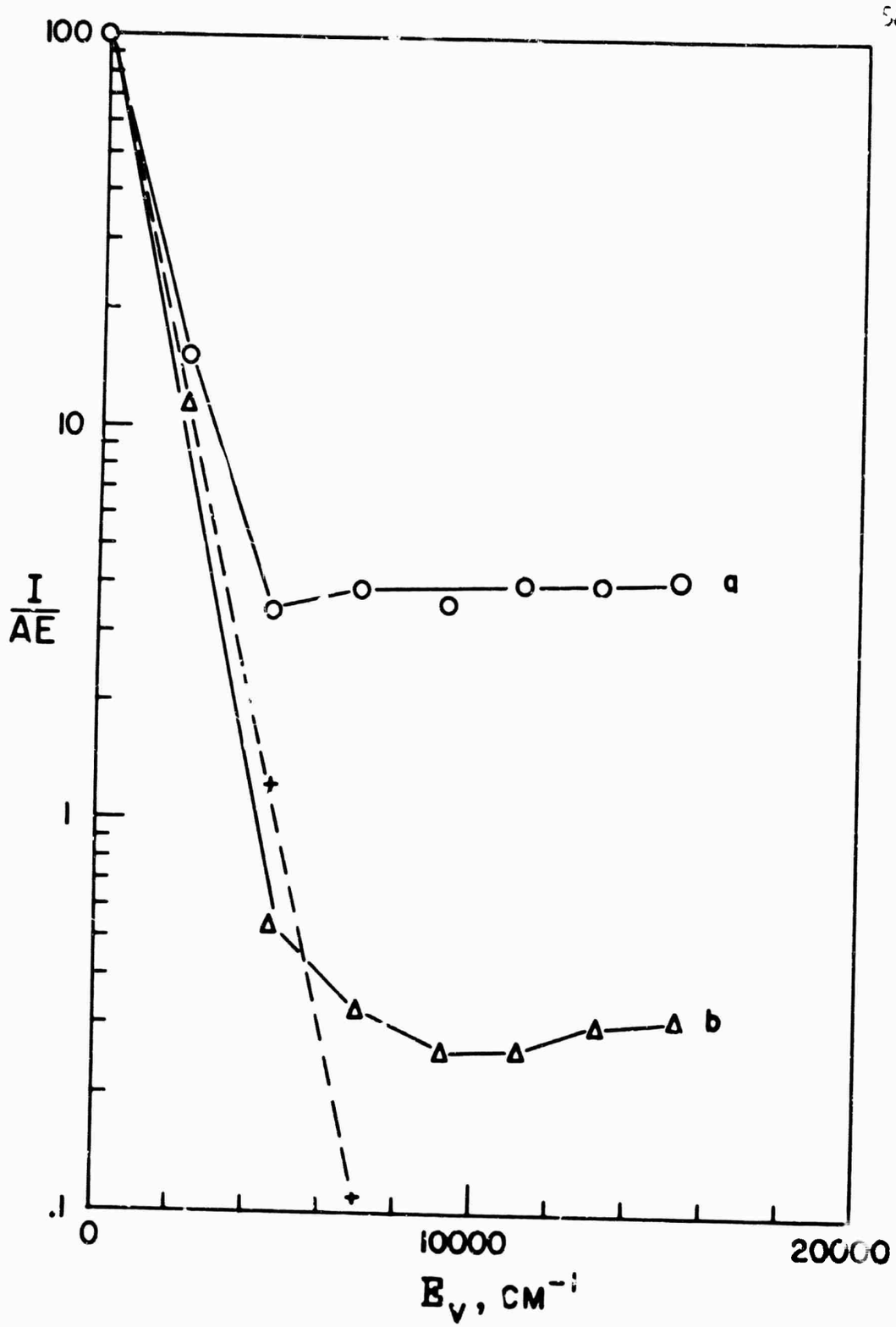

FIG 3.11

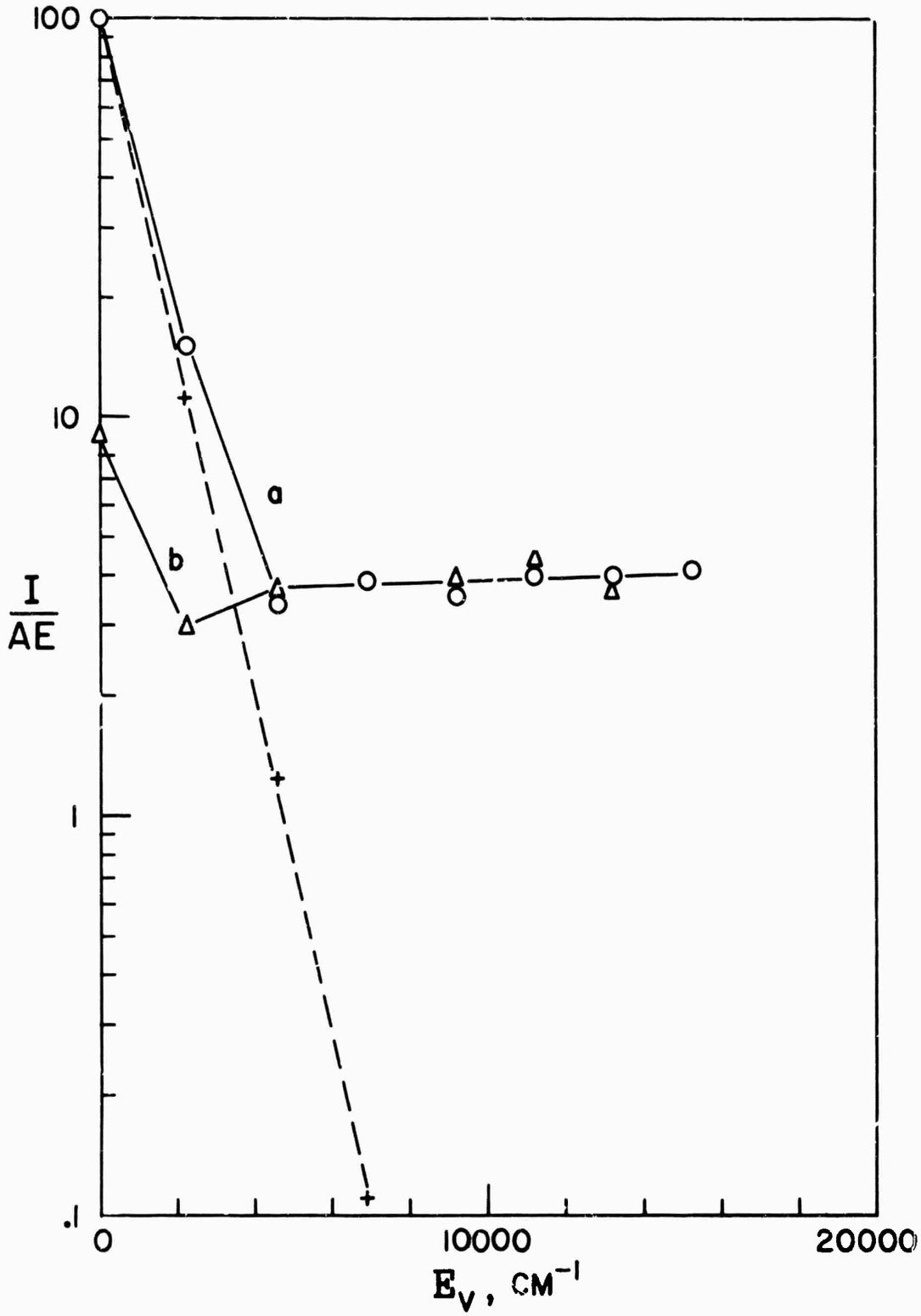

FIG 3.12

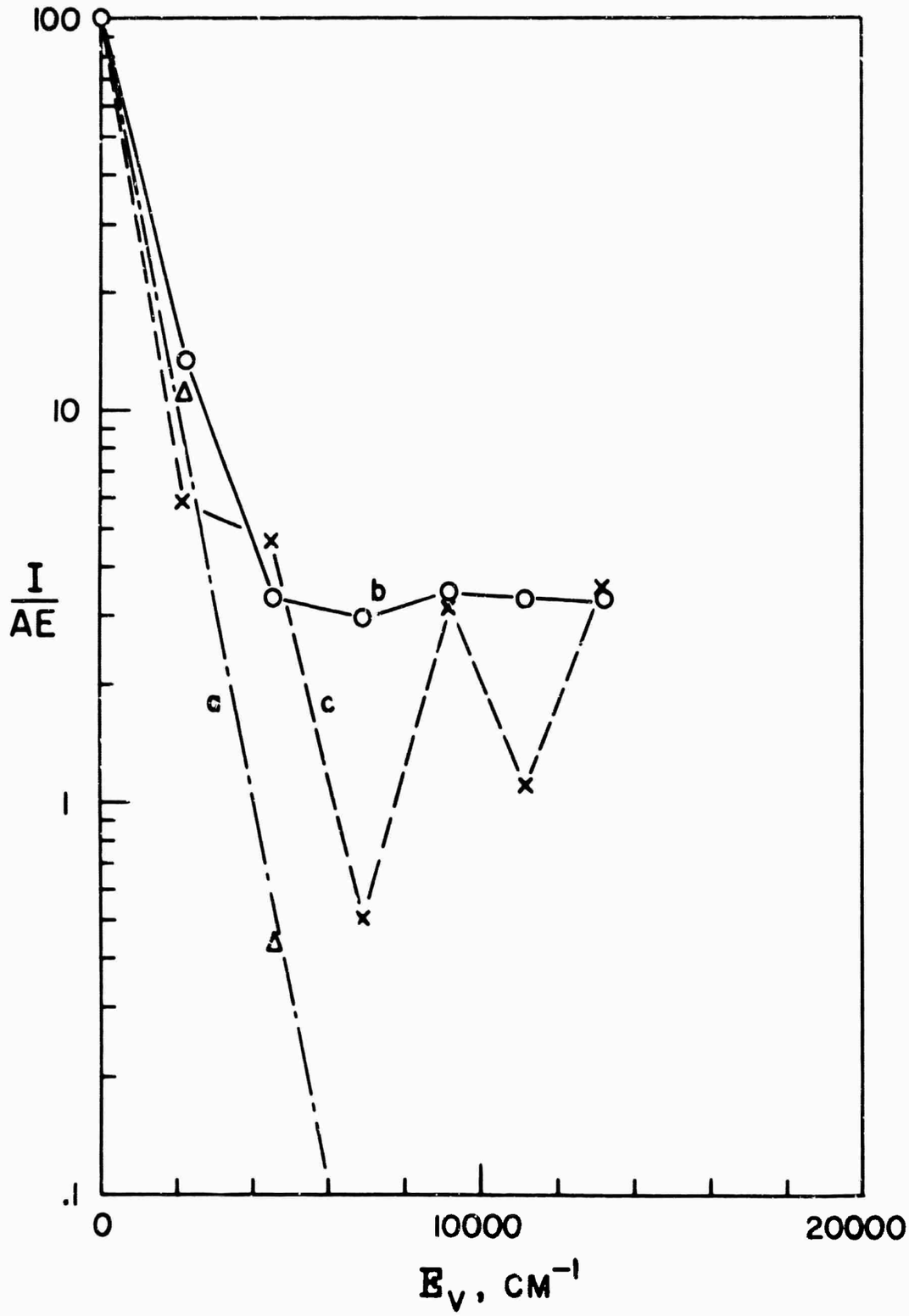

FIG 3.13

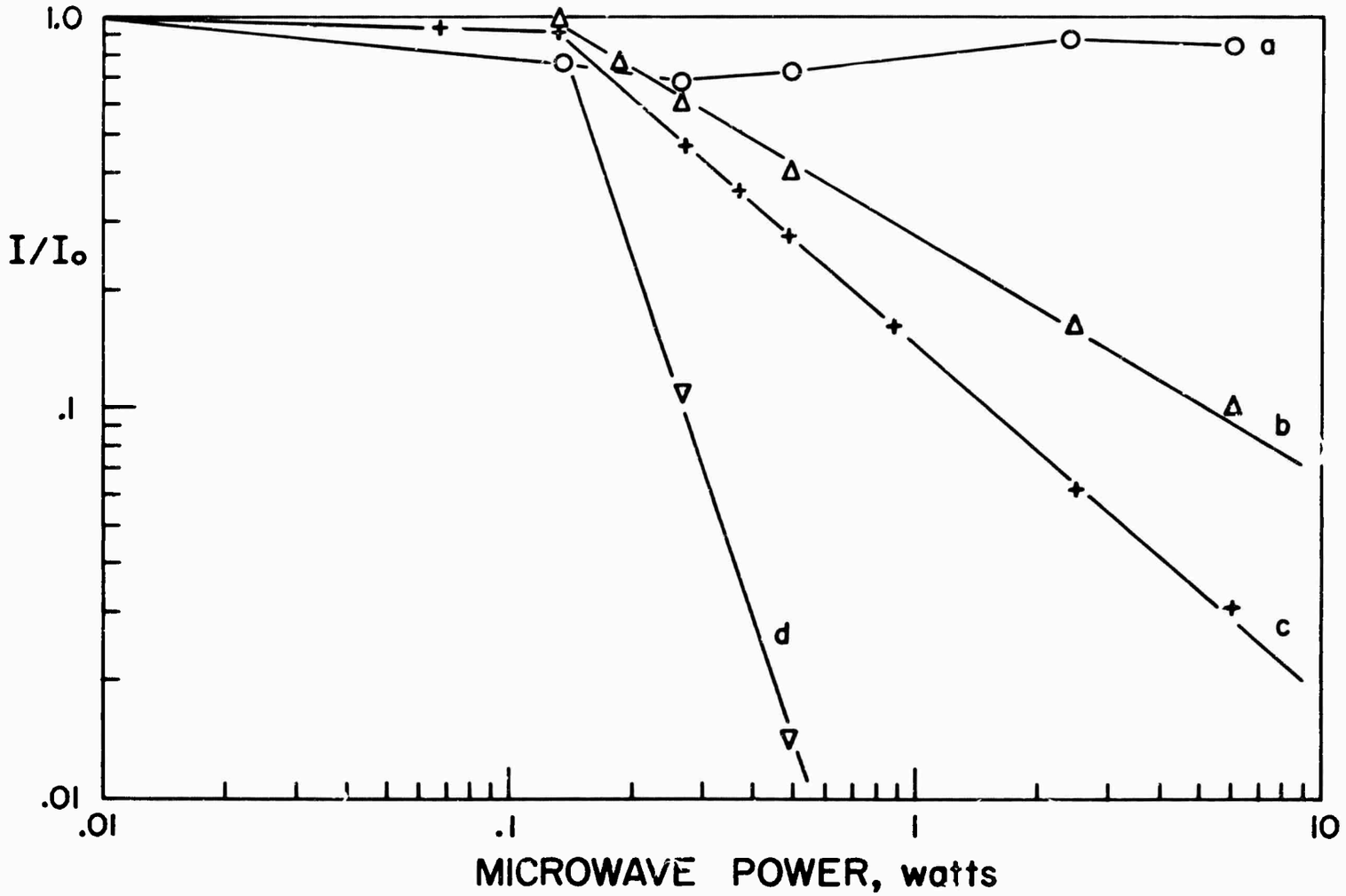

FIG 3.14

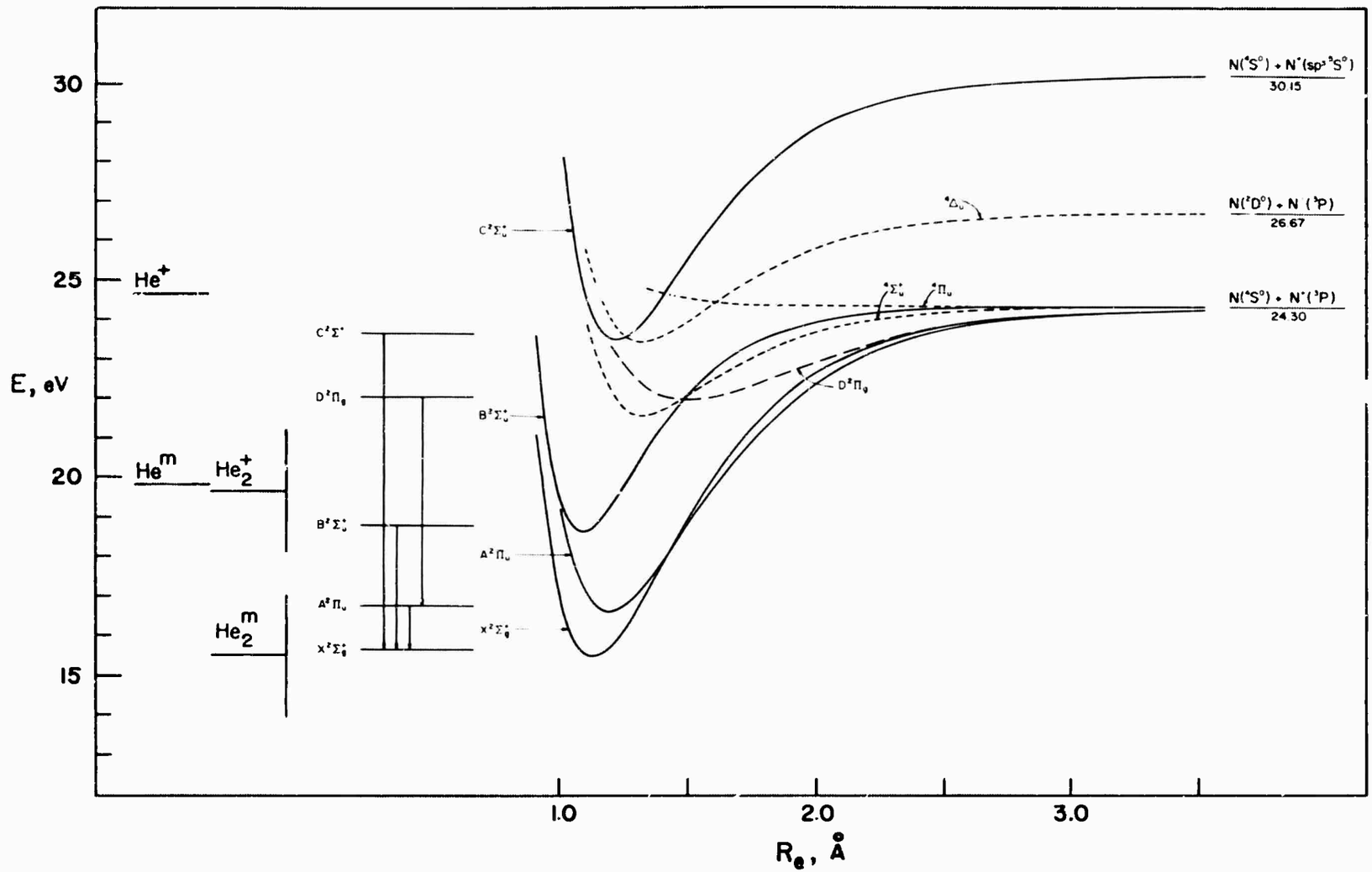
30
25
20
15
E, eV
He+
Hem
He2+
He2m
C²Σ+
D²Πg
B²Σu+
A²Πu
X²Σg+
C²Σu+
B²Σu+
A²Πu
X²Σg+
D²Πg
⁴Δu
⁴Σu+
⁴Πu
N(⁴S°) + N+(sp³ ³S°)
30.15
N(²D°) + N+(³P)
26.67
N(⁴S°) + N+(³P)
24.30
1.0
2.0
3.0
Re, Å

FIG 3.15

IV REACTION KINETICS OF EXCITED STATES

4.1 General Rate Equations

A method for measuring thermal energy-ion-neutral reaction rates in a steady-state afterglow system has been developed by Ferguson, et al,[1,2] hereinafter referred to as I and II. Briefly, observations of primary and secondary ions as a function of reactant concentration were used to identify reaction products and to measure rate coefficients. Ions were detected and concentrations measured with an electric quadrupole mass spectrometer. In this manner, measurements of absolute rate constants have been made for a wide variety of ion-neutral reactions in the range of 10^{-9} to 10^{-13} sec^{-1}.

It is the purpose of the present experiment to measure the absolute rate constants for exothermic reactions of added reactant gases with long-lived energetic helium species. The helium species include the metastable atom, $He(2^3S)$ or He^m, the metastable molecule, $He_2(^3\Sigma)$ or He_2^m, the ground state atomic ion, He^+, and the ground state molecular ion, $He_2^+(^2\Sigma)$. Reactions of the singlet metastable helium atom, $He(2^1S)$, are considered negligible compared to the triplet for reasons to be discussed later. Several atomic and molecular reactant gases were added to the helium afterglow -- Ar, Kr, N_2, O_2, H_2, NO, CO, and CO_2.

Observation of excited-state reactants and products as a function of reactant concentration are used to identify the reaction mechanisms and to measure the absolute rate constants. By varying the pressure, discharge power, and quenching microwave field,

concentrations of energetic helium species can be varied relative to one another such that individual excitation mechanisms containing a single species can then be studied.

The actual detection and concentration measurements of energetic helium species are indirectly made by observing the selective excitation of added reactants. In many cases, the excitation of a vibrational level of an excited electronic state for the reactant added to the helium afterglow can be identified with an individual helium species. With a few simplifying assumptions, the integrated intensity dependence of the selective excitation upon the reactant concentration can be interpreted in terms of a rate constant. Excitation and relaxation kinetics are presented in detail for nitrogen since the individual excitation mechanisms with nitrogen for each energetic helium species except He^+ has been studied and can be observed by the subsequent emission from N_2^{+*}. For He^+ reactions, CO_2 has been used as the detector by observing the resulting CO^{+*} emission.

Exact mathematical descriptions for fast gas flows of discharged gases and mixing of reactant gases downstream are very complicated. In the light of the recent results in II, the following assumptions concerning the present apparatus simplifies the model for the kinetics of the reaction: (1) downstream at the reactant gas

inlet, ion diffusion has relaxed to its fundamental mode; (2) electron-ion recombination rates depend linearly on ion concentration; (3) reactant gases diffusively mix with the helium flow and are of uniform concentration downstream from the point of introduction and are of negligible concentration upstream.

Validity of the experimental measurements under the preceeding assumptions can be checked in several ways. First, the assumptions in their present form have already been applied to the rate measurements in the similar fast flow system described in I. In II, the method of diffusive mixing of the reactant gases (assumption 3) was investigated both empirically by studying modes of introducing the reactants and by a theoretical analysis of the flowing diffusion problem. In addition, measurements of charge concentrations in the afterglow ($<5\times10^{-9}$ cm^{-3}) substantiate assumption (2). That is, the electron loss rate was attributed primarily to ambipolar diffusion where the loss by electron-ion recombination was treated as a perturbation. Combination of (1) and (2) yields a linear dependence of the diffusion and recombination loss rate on ion concentration. Therefore it is concluded that the assumptions stated in II would directly apply to the present measurements since the flow system described in Chapter 2 was similar to that used in I. The

first assumption concerning the uniformity of gas density down the tube is also consistant with the calculations in Section 2.2.

In developing the method for rate constant measurements of reactions involving active helium reactants, the following excitation mechanisms need be considered:

$$He^m + N_2 \rightarrow He + N_2^+ (B^2\Sigma,\ v = 0) + e \qquad (4.1a)$$

$$He^+ + N_2 \rightarrow He + N + N^+ \qquad (4.1b)$$

$$He_2^+ + N_2 \rightarrow 2He + N_2^+ (B^2\Sigma,\ v > 2) \qquad (4.1c)$$

$$He_2^m + N_2 \rightarrow 2He + N_2^+ (A^2\Pi) + e \qquad (4.1d)$$

$$He^+ + CO_2 \rightarrow He + O + CO^+(^2\Pi) \qquad (4.1e)$$

$$He(2^1S) + N_2 \rightarrow He + N_2^+ (B^2\Sigma) + e \qquad (4.1f)$$

Steady-state concentrations of the singlet metastable helium are taken to be more than an order of magnitude lower than the triplet both because of the failure to observe $He(^1S)$ in absorption at 5016Å and of the known loss mechanism for the singlet, namely, the very rapid conversion of the singlet to triplet by superelastic collision with an electron[3],

$$He(^1S) + e \xrightarrow{k_1} He(^3S) + e \qquad (4.2)$$

The charge transfer reaction (4.1b) is presumed to proceed at a faster rate by the dissociative charge transfer path compared to the direct charge transfer into the radiating $C^2\Sigma_u$ state of N_2^+ because of the predissociation by the $^4\Pi_u$ state as discussed in I and Section 3.4. The resulting reaction products are left in their respective ground states. Consequently,

(4.1b) cannot be used in the rate measurements of He^+ reactions. Therefore, the dissociative charge transfer reaction with CO_2, (4.1e) is used since the CO^+ reaction product is left in the excited $^2\Pi$ state which emits the well known comet-tail system.[4]

Relative intensity measurements of the resulting N_2^+ and CO^+ emission given in (4.1) are used to monitor the excited state populations contained in the reaction products. In addition, the relative concentrations of the excited states are used to observe the energetic helium densities in the afterglow by way of their linear dependence given by bimolecular reaction rate theory. One may distinguish between the reactions listed above both by proper choice of the emission bands which are characteristic of a single active helium species and by a suitable choice of the experimental conditions which favor a particular species in the afterglow region.

In order to arrive at general kinetic equations describing excitation and relaxation of reactants added to a helium afterglow, the source and loss mechanisms for each of the energetic helium species need be considered. Loss of energetic helium due to reactant must be separated from other loss mechanisms characteristic of the pure helium afterglow.

For the sake of completeness, each mechanism which can be responsible for the production or loss of energetic helium species in the afterglow is included in the rate equations. The kinetic equations governing the concentration of the triplet metastable atom, He^m, in the afterglow of pure helium is given by

$$\frac{\partial[He^m]}{\partial t} = k_1[He(2^1S)]n_e - k_2[He^m]^2 - k_3[He^m][He]^2 - D'\nabla^2[He^m] - k_4[He^m]n_e \quad (4.3)$$

where k represents the rate constant in $cm^3\ sec^{-1}$. $[He^m]$ and n_e are the metastable helium and electron concentration, respectively expressed in cm^{-3}. D' is the diffusion coefficient for He^m in pure helium. The first term represents the production mechanism from singlet metastables by superelastic collision with electrons (reaction 4.2) K_2 indicates the loss due to metastable-metastable collisions of the type,

$$He^m + He^m \xrightarrow{k_2} He^+ + e + He \quad (4.4)$$

The loss term represented by k_3, is due to the three body reaction

$$He^m + 2He \xrightarrow{k_3} He_2(^3\Sigma_u^+) + He \quad (4.5)$$

Metastable triplet loss by diffusion of He^m in He to the walls is accounted for in the next term. Under the assumption that the diffusion has relaxed to its fundamental mode, the loss rate is given by the factor $-\frac{D'}{\Lambda^2}[He^m]$, where Λ is the characteristic diffusion length[5]. The last term accounts for the loss of triplet metastables by collisional de-excitation with electrons.

In a similar manner, the helium atomic ion concentration in the afterglow of pure helium is governed by the equation,

$$\frac{\partial[He^+]}{\partial t} = k_2[He^m]^2 - \alpha'[He^+]n_e - \frac{D'_a}{\Lambda^2}[He^+] - k_5[He]^2[He^+] \quad (4.6)$$

where α' is the electron-ion recombination coefficient, D'_a represents the atomic ambipolar diffusion coefficient for He^+ in He. The production mechanism represented by k_2 arises from metastable-metastable collisions as given in reaction (4.4). The next two

loss processes are electron-ion recombination and ambipolar diffusion to the walls. The last term represents the three-body reaction where an atomic ion reactant is lost and a product molecular ion is formed,

$$He^+ + 2He \xrightarrow{k_5} He_2^+ + He \tag{4.7}$$

The helium molecular ion concentration is described by the differential equation,

$$\frac{\partial[He_2^+]}{\partial t} = k_5[He]^2[He^+] - \alpha''[He_2^+]n_e - \frac{D_a''}{\Lambda^2}[He_2^+] \tag{4.8}$$

where the single production mechanism is the three-body reaction (4.7). The following two terms measure the electron-ion recombination and ambipolar diffusion loss rates, respectively. The electron-molecular ion recombination coefficient, α'', is composed of both radiative (non-dissociative) and dissociative recombination with $\alpha'' = \alpha_R'' + \alpha_D''$.

The afterglow concentration of the $2^3\Sigma$ metastable helium molecule, He_2^m, is given by the time-dependent equation,

$$\frac{\partial[He_2^m]}{\partial t} = \alpha''[He_2^+]n_e + k_3[He^m][He]^2 - \frac{D_a''}{\Lambda^2}[He_2^m] \tag{4.9}$$

The source mechanism for He_2^m represented by the first term on the right hand side of the equation can be used in the present form for the following two reactions

$$He_2^+ + e \rightarrow He_2^m \tag{4.10a}$$

$$He_2^+ + e \rightarrow He_2^* \rightarrow He_2^m + h\nu \tag{4.10b}$$

where the excited state in (4.10b) is assumed to be connected by

electric dipole radiation to the metastable He_2^m state. Since the radiative lifetime and radiative recombination coefficient are approximately 10^{-8} sec and 4×10^{-9} cm^3 sec^{-1} respectively, electron-ion recombination will be the rate determining step. Therefore the time rate of change of He_2^m for both (4.10a) and (4.10b) processes will be given by the first term in (4.9). The second term with the rate constant, k_3, measures the production of He_2^m by the three-body reaction (4.5). The last term represents the diffusion of He_2^m in He.

To use nitrogen and carbon monoxide excited-state populations as a function of reactant concentration, the source and loss mechanisms for these populations must be considered. In addition to the reactions listed in (4.1), possible source and loss mechanisms which determine the steady-state population of the v' vibrational level of an excited state of the nitrogen ion in the afterglow are: (1) direct excitation from the ground state by electron impact, (2) vacuum ultraviolet photon absorption, (3) radiative transitions, (4) inelastic collisions with excited state products of the primary reaction, (5) low energy inelastic collisions, and (6) loss of N_2^+ by volume recombination and diffusion.

The excitation mechanism (1) is not expected to be important in the present experiments since the electron energy is nearly in thermal equilibrium in the afterglow. Even if this assumption were in doubt, excitation of the $C^3\Pi_u$ state of N_2 is expected to predominate[6]. Process (2) has been shown to be negligible for

the excited states involved by the pulsed-discharge method described in Chapter 2. Radiative transitions (3) are very important for the excited state populations of N_2^+ and will be considered in the following discussion. The effectiveness of indirect excitation of nitrogen by inelastic collisions with excited state products is dependent upon the reactant under study and the individual N_2^+ band being observed. Therefore the relative contribution of process (4) as a source mechanism will be considered separately for each reaction. The most frequent low energy inelastic collisions (5) are expected to be between N_2^+ and the carrier gas with a transfer of energy of approximately kT or less. With the low gas kinetic temperatures ($\sim 300^{\circ}K$) of the afterglow, inelastic collisions would change only the rotational population within a vibrational band. An observable effect of these "low energy" inelastic collisions might be a tendancy to smooth out large population differences between rotational levels. The relaxation mechanisms of excited states of N_2^+ include diffusion and recombination as well as radiative losses. The loss mechanisms (6) are not expected to be important in the present experiments because only states connected by electric dipole radiation are considered and the relaxation due to radiative losses are many orders of magnitude faster than either diffusion or volume recombination for the pressures used in these experiments.

In view of the predicted source and loss mechanisms and subsequent assumptions, the kinetic equation describing the

population of the v' vibrational level of an excited electronic state of N_2^+ can be written,

$$dN_{v'}/dt = k_a^{v'}[He^m][N_2] + k_b^{v'}[He^+][N_2] + k_c^{v'}[He_2^+][N_2] + k_d^{v'}[He_2^m][N_2] + k_i^{v'}[X^m][N_2] + \sum_v N_v A_{vv'} - N_{v'} \sum_{v''} A_{v'v''} \qquad (4.11)$$

By definition, $k_a^{v'}$, $k_b^{v'}$, $k_c^{v'}$ and $k_d^{v'}$ are the individual rate constants referring a particular vibrational level v' of an excited electronic state in the products of the reactions outlined in (4.1). Absolute rate constants can be obtained by taking the sum of the individual rate coefficients for all possible vibrational levels and electronic states in the product, i.e., for reaction (4.1a),

$$k_a = \sum_{e'} \sum_{v'} k_a^{v'} \qquad (4.12)$$

Similarly $k_i^{v'}$ is the individual rate constant which refers to the indirect excitation of the v' vibrational level of the N_2^+ electronic state under study by a complex reaction of the type,

$$He^m + X \rightarrow He + X^m$$
$$X^m + N_2 \rightarrow X + (N_2^+)^* + e \qquad (4.13)$$

where He^+, He_2^+ and He_2^m may occur in place of He^m. For example, a complex reaction[1,7] expected to occur in the present experiments arises when Ne is added to the helium afterglow by the first inlet port and nitrogen by the second.

$$He_2^+ + Ne \rightarrow 2He + Ne^+$$
$$Ne^+ + N_2 \rightarrow Ne + N_2^+ (D^2\Pi_g) + e \qquad (4.14)$$

The rates of formation and decay due to spontaneous radiation are indicated by the last two terms in (4.11) respectively.

$A_{v'v''}$ is the Einstein coefficient giving the spontaneous emission transition probability per second for a transition from v' of the excited electronic state to v'' of the lower state. In the formation term, the sum is taken over all upper levels, v, which are connected by electric dipole transition matrix elements. Similarly for the decay term the sum is taken over all lower levels for which the electric dipole transition matrix element is non-vanishing.

The intensity of a spectral line for spontaneous emission is proportional to the population of the upper state, the Einstein coefficient for spontaneous emission, and the energy difference between the upper and lower states[8],

$$I_{ij} = N_i A_{ij} E_{ij} \tag{4.15}$$

Similarly, the integrated intensity $I_{v'v''}$ of a molecular band system connected by an electric dipole transition matrix element is defined,

$$I_{v'v''} = N_{v'} A_{v'v''} E_{v'v''} \tag{4.16}$$

To calculate the excited state populations, $N_{v'}$, in Eq. (4.16) the rate equation (4.11) must be solved in the steady state approximation. In this approximation, the concentration of the excited state nitrogen treated as an intermediate is considered constant and

$$dN_{v'}/dt = 0 \tag{4.17}$$

Solving Eq. (4.11) for the steady state population, $N_{v'}$, and substituting in Eq. (4.16), the integrated intensity of the (v'v'') molecular band is given by

$$I_{v'v''} = \frac{A_{v'v''}E_{v'v''}}{\sum_{v''} A_{v'v''}} \left[k_a^{v'}[He^m][N_2] + k_b^{v'}[He^+][N_2] + k_c^{v'}[He_2^+][N_2] + k_d^{v}[He_2^m][N_2] + k_i^{v'}[X^m][N_2] + \sum_v N_v A_{vv'} \right] \quad (4.18)$$

Equation (4.18) is the basic relation between the observed emission intensity and the reactant concentrations. Starting from this equation, in the following sections, two somewhat different approaches will be formulated for measuring the reaction rate constants.

4.2 Reactions Involving Energetic Helium and Nitrogen

The integrated intensity of the molecular emission given in (4.18) as a function of nitrogen reactant concentration can be interpreted in terms of the rate constant for the reaction producing the emission. Attention will be directed toward allowed transitions originating in the v' = 0 level of the $B^2\Sigma_u^+$ excited electronic state of N_2^+. The Penning reaction,

$$He^m + N_2 \rightarrow He + N_2^+ (B^2\Sigma) + e \quad (4.1a)$$

has been found to proceed at a rate of $k_a = 9.0 \times 10^{-11}$ cm^3 sec^{-1} and to preferentially populate the low vibrational levels of the $B^2\Sigma_u^+$ state of N_2^+ according to the Franck-Condon principle for excitation from the ground state of N_2 [9]. The contribution to the integrated intensity for the selective excitation of the v' = 0 level of the $B^2\Sigma_u^+$ state by the second term in Eq. (4.18) representing the charge-transfer reaction with the atomic helium ion is expected to be negligible compared to reaction (4.1a), that is, $k_b^{v'} \ll k_a^{v'}$ for v' = 0. The rate of the direct charge transfer reaction,

$$He^+ + N_2 \xrightarrow{k_b} He + N_2^+ (B^2\Sigma) + 5.8 \text{ eV}$$

is expected to be vanishing small, for small v since energetics of the reaction is exothermic and the large energy defect is prohibitively non-resonance for the asymmetrical charge transfer reaction.

Although there is some doubt as to the range of available energy for transfer in the reaction[10],

$$He_2^m + N_2 \rightarrow 2He + N_2^+ (B^2\Sigma) + e$$

the contribution to the $N_2^+ (B^2\Sigma)$ population is expected to be negligible as discussed in Section 3.4.

In this section, only the reactions between energetic helium and nitrogen are considered. The only way nitrogen can be excited indirectly by an energetic species X^m represented by the rate constant, $k_i^{v'}$, is when X is an impurity. From the results obtained in Section 2.4 the contribution from the next to last term in (4.18) is taken to be negligible compared to reaction (4.1a).

The last term in Eq. (4.18) gives a value for the rate of populating the v' = 0 level of the $B^2\Sigma_u^+$ state by all possible transitions from higher energy levels. The sum is to be taken over all vibrational levels of each electronic state connected to the $B^2\Sigma(v' = 0)$ level by electric dipole transition matrix elements. Of all the known electronic states with energy greater than $B^2\Sigma_u^+$ [11], only the $D^2\Pi_g$ state has the proper symmetry which satisfies the electronic transition selection rule for homonuclear molecules, namely, only even states can combine with odd, $g \leftrightarrow u$. Also, the contribution to the $B^2\Sigma$ (v' = 0) level population by the transition,

$D^2\Pi_g - B^2\Sigma_u$, is assumed to be negligible compared to the other populating processes because this transition has not been observed in the present work nor has it been reported in the literature. Moreover qualitative estimate of the Franck-Condon effect from the potential curves indicates that the Einstein coefficients are relatively small due to small Frank-Condon factors, $q_{v'v''}$.

Eq. (4.18) can now be written,

$$I_{v'v''} = \frac{A_{v'v''}E_{v'v''}}{\sum_{v''} A_{v'v''}} \left[k_a^{v'}[He^m][N_2] + k_c^{v'}[He_2^+][N_2] \right] . \qquad (4.19)$$

where the upper level refers to the v' = 0 level of the $B^2\Sigma_u^+$ electronic state. The kinetic rate equations (4.3) and (4.8) governing the He^m and He_2^+ concentrations as a function of time in pure helium have to be modified upon addition of the reactant nitrogen. Starting with Eq. (4.3), the time dependence of the metastable concentration can be expressed in terms of the axial distance down the tube for a given flow rate, i.e.

$$\frac{\partial[He^m]}{\partial t} = \bar{u}\,\frac{\partial[He^m]}{\partial z} \qquad (4.20)$$

where $\bar{u}$ is the average flow velocity and z is the axial position along the tube. In the present experiment, one is interested in the rate of change of He^m as a function of axial distance down the tube beginning at the point of nitrogen reactant introduction. With a rate, $k = 1.3 \times 10^{-9}$ cm^3/sec, the formation of He^m by superelastic collisions of electrons with $He(^1S)$ from the discharge will have gone to completion before introducing the reactant and can be

neglected in the remaining discussion.

By representing the combined loss mechanisms for He^m in a pure helium afterglow by K', Eq. (4.3) becomes

$$\bar{u}\,\frac{\partial[He^m]}{\partial z} = -\,K'[He^m] \tag{4.21}$$

Upon addition of nitrogen as a reactant at the axial position along the tube, $z = z_o$, the rate equation governing the He^m concentration will be modified to include the loss of He^m by inelastic collisions with N_2 given by reaction, (4.1a). Eq. (4.21) becomes

$$\bar{u}\,\frac{\partial[He^m]}{\partial z} = -\,K'[He^m] - k_a[He^m][N_2] \tag{4.22}$$

With the position of the spectrometer and hence the position for observing the molecular nitrogen emission located at $z = z_1$ where $z_1 - z_o = \ell$, the He^m concentration can be obtained as a function of z by solving Eq. (4.22) with the following assumptions. For the range of N_2 flow rates used, $[N_2] > [He^m]$ such that $[N_2]$ can be considered constant over the axial distance ℓ; the validity of this assumption will be discussed in the following chapter when the N_2 and He^m concentrations are measured for the experiment in question. In general the N_2 reactant concentration will be greatly in excess of the He^m concentration and need only be considered in the limiting region $(N_2) \to 0$. Eq. (4.22) becomes

$$\frac{d[He^m]}{[He^m]} = -\,\frac{1}{\bar{u}}\left[K' + k_a[N_2]\right] dz$$

Integrating from z_o to z_1,

$$\ln[He^m]_{z_1} - \ln[He^m]_{z_o} = -\,\tau\left[K' + k_a[N_2]\right] \tag{4.23}$$

and

$$[He^m]_{z_1} = [He^m]_{z_o} \exp\left\{ - \tau\left[K' + k_a[N_2]\right]\right\} \tag{4.24}$$

where $\tau = \ell/\bar{u}$ is the reaction time and $(He^m)_z$ and $(He^m)_{z_o}$ are the metastable helium concentrations of positions $z = z_1$ and z_o respectively for a given nitrogen concentration.

As was mentioned earlier, the method of measuring rate constants outlined in this section is to be applied to the reaction (4.1a). This particular reaction was chosen because it was most easily isolated from the others. Therefore all that remains of Eq. (4.19) is in some way to separate the contributing mechanism for populating the $v' = 0$ level of the $B^2\Sigma$ state by charge transfer with He_2^+. The relative concentration of He_2^+ can be made negligible compared to that of He^m by applying a weak microwave field between the discharge and nitrogen reactant input as was explained in Section 3.3. The integrated intensity equation (4.19) becomes

$$I_{v'v''} = \frac{A_{v'v''}E_{v'v''}}{\sum_{v''} A_{v'v''}} k_a^{v'}[He^m]_{z_1} [N_2] \tag{4.25}$$

Substituting Eq. (4.24) for the He^m concentration at z_1,

$$I_{v'v''} = \frac{A_{v'v''}E_{v'v''}}{\sum_{v''} A_{v'v''}}\left\{k_a^{v'}[He^m]_{z_o} [N_2] \exp\left[- \tau\left\{k_a[N_2] + K'\right\}\right]\right\} \tag{4.26}$$

By varying the nitrogen flow rate, the corresponding change in emission intensity from Eq. (4.26) becomes,

$$\frac{dI_{v'v''}}{d(N_2)} = \frac{A_{v'v''}E_{v'v''}}{\sum_{v''} A_{v'v''}} k_a^{v'}[He^m]_{z_o} \left[1-\tau k_a[N_2]\right]\exp\left\{-\tau\left[k_a[N_2] + K'\right]\right\} \tag{4.27}$$

At this point, it is instructive to remember the assumption about

the velocity distribution in the afterglow, namely, that flow is described by Poiseuille's Eq. (2.3) with a parabolic radical velocity distribution over the diameter of the tube. The integrated emission intensity observed at position z, is expected to increase with N_2 concentration according to Eq. (4.27), attain a maximum, and then decrease with increasing $[N_2]$. The intensity maximum is described by the condition,

$$\left[dI_{v'v''}/d[N_2]\ I_{max}\right] = 0 \tag{4.28}$$

Setting Eq. (4.27) equal to zero according to Eq. (4.28) yields the following expression for the rate constant k_a,

$$k_a = \frac{1}{\tau(N_2)_{max}}\ cm^3\ sec^{-1} \tag{4.29}$$

where $[N_2]_{max}$ is the nitrogen concentration corresponding to the maximum in $I_{v'v''}$. The mestastable helium concentration at z_o, $[He^m]_{z_o}$ does not depend upon the nitrogen flow rate.

4.3 General Method for Energetic Helium-Reactant Reactions

Determination of the rate constants for Penning reactions involving He^m and added reactant gases can be made by measuring metastable helium concentration by light absorption[1]. The He^m concentration as a function of reactant flow rate is then interpreted in terms of a reaction rate. Application of this method is strongly dependent upon the He^m concentration, absorption path length, and overall sensitivity of the apparatus. The method to be developed in this section and the results given in Chapter 5 likewise interpret

the rate constant by relating the metastable helium concentration as well as the other energetic helium species to the reactant flow rate. However the method for observing the energetic helium species depends upon the relative intensity measurements of the resulting emission when nitrogen or carbon dioxide (reactions 4.1) is added to the afterglow. At a given nitrogen flow rate, the particular vibrational level of the excited electronic state characteristically excited by a given active helium species is observed. After isolating the reaction favoring this excitation from competing reactions by the methods described in the previous sections, the reactant is then added upstream to the nitrogen input. The corresponding decrease in energetic helium concentration as a function of reactant flow rate can then be restated as the rate constant for the reaction.

Eq. (4.25) for the nitrogen emission intensity produced by reaction (4.1a) represents the detection method for He^m at an axial position z. It is assumed that the contribution to $I_{v'v''}$ by the reaction with He_2^+ is negligible when a low power microwave field is applied to the afterglow as was described in Section 4.2. The steady-state He^m concentration at z_1 has to be modified upon addition of the reactant X to account for the reaction.

$$He^m + X \xrightarrow{k_x} He + X^+ + e \qquad (4.30)$$

The rate equation (4.22) governing the He^m concentration now becomes

$$\bar{u}\,\frac{\partial[He^m]}{\partial z} = -K'[He^m] - k_a[He^m][N_2] - k_x[He^m][X] \qquad (4.31)$$

where the additional loss mechanism is represented by the rate

constant k_x. The secondary excitation of the nitrogen by energetic species of the reactant X according to the reaction (4.13) usually will be neglected because for most of the reactants studied, reactions (4.13) do not take place. This process will be one of the first to be investigated in attempting to explain any anomalous behavior in the rate measurements.

In general the nitrogen and reactant concentration will be greatly in excess of the He^m concentration such that [X] can be considered to be constant down the tube. To obtain the He^m concentration at the point of observing the nitrogen emission $[He^m]_{z_1}$, one must integrate Eq. (4.31). Since nitrogen is added at z_1, the loss term represented by k_a can be set equal to zero. Eq. (4.31) then becomes

$$\frac{d[He^m]}{[He^m]} = -\frac{1}{\bar{u}}\left[K' - k_x[X]\right] \tag{4.32}$$

where the integration is taken from z_o to z_1,

$$\ln[He^m]_{z_1} - \ln[He^m]_{z_o} = -\left[\tau K' + k_x[X]\right] \tag{4.33}$$

and

$$[He^m]_{z_1} = [He^m]_{z_o} \exp\left\{-\tau\left[K' + k_x[X]\right]\right\} \tag{4.34}$$

Now let $[He^m]_{z_1}{}^*$ represent the metastable helium concentration for the limit $[X] \to 0$. Eq. (4.34) becomes

$$[He^m]_{z_1} = [He^m]_{z_1}{}^* \exp\left[-\tau k_x[X]\right] \tag{4.35}$$

where again τ is the reaction time $\tau = \ell/\bar{u}$. Substituting Eq. (4.35) in Eq. (4.25)

$$I_{v'v''} = \frac{A_{v'v''}E_{v'v''}}{\sum_{v''} A_{v'v''}} k_a^{v'}[He^m]_{z_1}^{*} \exp -\left[\tau k_x[X]\right] \tag{4.36}$$

In the limit $[X] \rightarrow 0, \rightarrow I_{v'v''}$, and the integrated intensity becomes,

$$I^{o}_{v'v''} = \frac{A_{v'v''}E_{v'v''}}{\sum_{v''} A_{v'v''}} k_a^{v'}[He^m]_{z_1}^{*} \tag{4.37}$$

Dividing Eq. (4.36) by (4.37) and taking the natural logarithm of both sides, one obtains,

$$\ln\left(\frac{I_{v'v''}}{I^{o}_{v'v''}}\right) = -\tau k_x[X] \tag{4.38}$$

Now the slope of the curve $\ln\left(\frac{I_{v'v''}}{I^{o}_{v'v''}}\right)$ plotted against [X] divided by the reaction time, τ, gives a value for the absolute rate constant, k_x.

Reactions with the atomic ion, He^+ of the type,

$$He^+ + X \xrightarrow{k_x} He + X^+ \tag{4.39}$$

are studied by observing the (1,0) band of the $A^2\Pi$-$X^2\Sigma$ electronic transition of CO^+. In an otherwise analogous method to that for He^m reactions outlined above, a relation similar to Eq. (4.38) can be obtained. The integrated intensity for the CO^+ emission whose upper state is populated according to reaction (4.1e) can be written;

$$I_{v'v''} = \frac{A_{v'v''}E_{v'v''}}{\sum_{v''} A_{v'v''}} k_e^{v'}[He^+]_{z_1}[CO_2] \tag{4.40}$$

From Eq. (4.6) describing the rate of change of He^+ concentration in a pure helium afterglow, one can make the following

substitution for the combined loss mechanisms.

$$\bar{u}\,\frac{\partial[He^+]}{\partial z} = -\,K_a'[He^+] \tag{4.41}$$

where $K_a' = \alpha' n_e + D_a'/\Lambda^2 + k_5[He]^2$

Upon addition of the reactants X and CO_2, Eq. (4.41) becomes

$$\bar{u}\,\frac{\partial[He^+]}{\partial z} = -\,K_a'[He^+] - k_e[He^+][CO_2] - k_x'[He^+][X] \tag{4.42}$$

Since CO_2 is added at the point of observation, one can neglect the term represented by k_e and integrate (4.42) from z_o to z_1 yielding

$$[He^+]_{z_1} = [He^+]_{z_1}^{*}\ \exp\left[-\,\tau k_x'[X]\right] \tag{4.43}$$

where again $[He^+]_{z_1}^{*}$ is the ion concentration at z_1 for $[X] \to 0$.

Substituting (4.43) in (4.40), one obtains,

$$I_{v'v''} = \frac{A_{v'v''}E_{v'v''}}{\sum\limits_{v''} A_{v'v''}}\ k_e^{v'}[He^+]_{z_1}^{*}\ \exp\left[-\,\tau k_x'[X]\right] \tag{4.44}$$

Dividing Eq. (4.44) by the intensity when $(X) \to 0$ and taking the natural logarithm, one obtains the relation similar to Eq. (4.38),

$$\ln\left(\frac{I_{v'v''}}{I^{o}_{v'v''}}\right) = -\,\tau k_x'[X] \tag{4.45}$$

where k_x' represents the rate of reaction (4.39).

For charge transfer reactions with the molecular helium ion of the type,

$$He_2^+ + X \overset{k_x'}{\rightleftharpoons} 2He + X^+ \tag{4.46}$$

the He_2^+ concentration is monitored by measuring the relative intensity of bands in the $B^2\Sigma$-$X^2\Sigma$ transition of N_2^+ originating from

the $v' \geq 4$ levels populated according to reaction (4.1c). According to the discussion in Section 3.4, the $v' \geq 4$ levels are not expected to be popu' ed by inelastic collision with He^m and He_2^m species. Although being exothermic, the charge transfer reaction with He^+ is assumed to be negligible because of the large energy defect involved ($\Delta E \sim 4.7$eV).

In a method analogous to the one outlined in Eq.s (4.32 to 4.38), the logarithm of the emission intensity ratio $I_{v'v''}/I^o_{v'v''}$ expressed as a function of reactant concentration is found to be

$$\ln \left(\frac{I_{v'v''}}{I^o_{v'v''}}\right) = - \tau k'_y [X] \tag{4.47}$$

where k'_y is the rate constant to be measured for the reaction (4.46).

Finally, reactions of the type

$$He_2^m + X \xrightarrow{k_y} 2\ He + e \tag{4.48}$$

can be studied by observing the $A^2\Pi$ - $X^2\Sigma$ transition of N_2^+ as a function of reactant concentration where the upper levels are populated according to reaction (4.1d). As was pointed out in Section 3.4, there is some uncertainty about the populating mechanisms for the $A^2\Pi$ state of N_2^+ because of the uncertainty in available energy in He_2^m for the reaction. If reaction (4.1e) is the assumed dominant mechanism for populating the $A^2\Pi$ state, then in a manner similar to the methods outlined above, the dependence of emission intensity on reactant concentration is found to be

$$\ln \left(\frac{I_{v'v''}}{I^o_{v'v''}}\right) = - \tau k_y [X] \tag{4.49}$$

where k_y is the rate constant for reaction (4.48) involving He_2^m.

The search for reaction mechanisms causing selective excitation of added reactant gases has lead to consideration of atomic and molecular helium emission in the afterglow itself. Assuming that the dominant helium emission is produced by electron-ion recombination into radiating states[13], then this emission can be used to measure the atomic and molecular helium ion concentration. The kinetic equation describing the population of the ith excited level of the helium atom is

$$dN_i/dt = \alpha(i)[He^+]\, n_e - N_i \sum_j A_{ij} \tag{4.50}$$

In the steady-state approximation, the rate of formation is set equal to the decay rate,

$$dN_i/dt = 0$$

and

$$N_i = \frac{1}{\sum_j A_{ij}}\, \alpha(i)[He^+]n_e \tag{4.51}$$

The simple model described by Eq. (4.51) is based on the assumption that the ith level is populated by direct electron-positive ion recombination with rate $\alpha(i)$ and decay is by radiative transitions to all possible lower energy levels j. Substituting the steady state population into Eq. (4.15),

$$I_{ij} = \frac{A_{ij}E_{ij}}{\sum_j A_{ij}}\, \alpha(i)[He^+]n_e \tag{4.52}$$

By adding the reactant X to the afterglow and measuring the intensity in Eq. (4.52) as a function of [X], the rate for the following reaction can be obtained,

$$He^+ + X \xrightarrow{k'_x} He + X^+ \tag{4.39}$$

The results obtained from (4.52) should give a direct comparison to the rate measurements obtained from Eq. (4.45). The steady-state He^+ concentration at z_1 with the reactant gas added to the afterglow has been given in Eq. (4.43). Substituting the expression in (4.52),

$$I_{ij} = \frac{A_{ij}E_{ij}}{\sum_j A_{ij}} \alpha(i)[He^+]^*_{z_1} \exp\left[-\tau k'_x[X]\right] \tag{4.53}$$

Dividing Eq. (4.53) by the expression for the intensity with $[X] \to 0$, and taking the logarithm of both sides, gives

$$\ln\left(\frac{I_{ij}}{I^o_{ij}}\right) = -\tau k'_x[X] \tag{4.54}$$

where the rate constant from (4.54) is to be directly compared to the value obtained from Eq. (4.45) for the same reactant.

If the molecular helium emission is predominately due to electron-ion recombination

$$He_2^+ + e \xrightarrow{\alpha'} He_2^* \tag{4.55}$$

the method outlined for the atomic emission can be applied to the rate measurements for the reaction,

$$He_2^+ + X \xrightarrow{k'_y} 2He + X^+ \tag{4.46}$$

An expression analogous to Eq. (4.47) is obtained,

$$\ln\left(\frac{I_{v'v''}}{I^{o}_{v'v''}}\right) = -\tau k'_{y}[X] \tag{4.56}$$

where $I_{v'v''}$ is the intensity for the (v',v'') band of the molecular helium emission. Again the rate measured in (4.56) can be compared to k'_y obtained from Eq. (4.47). A favorable comparison of the two methods, both for atomic and molecular helium ions would give confidence to the choice of excitation mechanisms with nitrogen excited by the two ions respectively.

IV REFERENCES

1. Fehsenfeld, F. C., Schmeltekopf, A. L., Goldan, P. E., Schiff, H. I., and Ferguson, E. E., J. Chem. Phys. 44, 4087 (1966).
2. Goldan, P. D., Schmeltekopf, A. L., Fehsenfeld, F. C., Schiff, H. I., and Ferguson, E. E., J. Chem. Phys. 44, 4095 (1966).
3. Bates, D. R., Phys. Rev. 77, 718 (1950).
4. Collins, C. B. and Robertson, W. W., J. Chem. Phys. 40, 701 (1964).
5. McDaniel, E. W., Collision Phenomena in Ionized Gases, John Wiley and Sons, Inc., New York, 1964.
6. Bennett, W. R., Jr., Ann. Phys. 18, 367 (1962).
7. Tanaka, Y., Namioka, T., and Jursa, A. S., Can. J. Phys. 39, 1138 (1961).
8. Nicholls, R. W., Ann. de Geophys. 20, 144 (1964).
9. Robertson, W. W., J. Chem. Phys. 44, 2456 (1966).
10. See Section 3.4.
11. Gilmore, F. R., The Rand Corp., RM-4034-PR (1964).
12. Herzberg, G., Molecular Spectra and Molecular Structure I., D. van Nostrand Co., Inc., New York 1950, p. 241.

V. EXPERIMENTAL RATE COEFFICIENTS

The following thermal energy rate constants have been obtained according to the methods and theory presented in the preceeding chapter. The large number of reactions and their associated rate coefficients are divided into four catagories, each corresponding to a single energetic helium species. Rates of reaction of several reactant gases with energetic helium have been measured; these reactants are Ar, Kr, N_2, O_2, H_2, NO, CO, and CO_2. With neon, no measurable rates were obtained since in each reaction investigated the logarithm of the emission intensity plotted against the neon flow rate gave a complicated, non-linear curve.

It is necessary to point out here that in each reaction, the rate constant obtained for two reactants gives the loss rate of the energetic helium since no measurements have been made of the reaction products. When a definite reaction path is written down, it should be taken to mean the most probable or the rate determining step. In many cases, there will exist more than one reaction mechanism leading to the same excited state product occurring at different rates and with different concentrations of reactants. The complicated dependence of the product energy distribution on rates and reactant concentrations can cause the dependence of the logarithm of the emission intensity on the reactant to become nonlinear.

The range of reactant concentrations used in the rate measurements is primarily determined by the sensitivity of the optical spectrometer used to observe the emission intensity. Under favorable

conditions, a variation of approximately two orders of magnitude is obtained for the relative intensity. In other examples, overlapping radiation is suspected to occur at relatively high reactant concentrations causing a nonlinear dependence and thus limiting the range of variation of the emission intensity. For this reason, the rate constants have been calculated from the initial slope of the graph. Since the reaction under study as well as the reaction producing the emission had been chosen to be the dominate processes for a given set of conditions, the initial portion of the logarithm of the intensity for low reactant concentrations indicates the mechanism under study.

The reactions in each of the four catagories were studied under conditions favorable to the particular energetic helium species of that catagory. The validity of the method was checked by making rate measurements on selected reactions under a wide variation of the experimental parameters. The range of downstream pressure for which measurements were obtained was 0.3 to 0.7 torr, produced by varying the helium flow rate. Changing the helium flow produced changes in the average velocity in the afterglow which in turn varied the reaction time. The current maintaining the helium discharge was varied between 20 and 150 milliamps.

Uncertainities quoted for the measured rate constants in the remainder of the chapter are much larger than the reproducibility of measurements under varying experimental conditions. Systematic errors in measuring the average helium flow velocity are in greatest doubt and therefore dominate the quoted errors. Under conditions

of laminar flow, the average velocity can be calculated from the measured values of the helium volumetric flow rate. As was discussed in Section 2.2 the radial dependence of the average flow velocity is described by a parabolic distribution according to Eq. (2.5). Reactions occurring in a narrow cylindrical region along the axis of the tube are then associated with a flow velocity two times the calculated average. As the "effective diameter" of the emission region and hence the diameter defining the reaction region was observed to vary from 4.0 to 5.9 cm for different experimental conditions, the corresponding values for the corrected average velocity $\bar{u}$, ranged from 1.5 $\bar{u}_o$ to 1.0 $\bar{u}_o$ cm sec^{-1}. The rate constants are calculated from the slope of the curves according to the general method in Section 4.3, and the following expression,

$$\ln \left(\frac{I_{v'v''}}{I^{o}_{v'v''}}\right) = - \tau k_x [X] \qquad (4.38)$$

With diffusive mixing of the reactants, according to assumption (3) in Section 4.1, the steady state reactant concentration, [X], in units of cm^{-3} is calculated from the measured flow rate by the relation,

$$[X] = - \frac{1}{A\bar{u}_o} \frac{dX}{dt}$$

where dX/dt represents the reactant flow rate in units of sec^{-1}. In each of the following measurements, the effective diameter of the source has been measured along with an estimate of the uncertainty.

Values quoted for the rate constants are the average values measured under different experimental conditions such as pressure, helium flow rate, and discharge power. The particular conditions for which the curves are given will be noted. In practically all the following reactions, the reproducibility falls well within the quoted uncertainities. Only when there appears some anomalous behavior will a discussion of the individual measurements be made.

5.1 Reactions with He^m

In addition to the Penning ionization rate constants to be reported for the reactions of He^m with the several reactant gases, the particular reaction,

$$He^m + N_2 \xrightarrow{k_a} He + N_2^+ + e \qquad (5.1)$$

was studied and rate constants measured by three somewhat different methods. In the first method as outlined in Section 4.2, the relative intensity for the (0,1) band of the $B^2\Sigma$ transition in N_2^+ was measured and plotted as a function of the nitrogen flow rate in Fig. 5.1. As reaction (5.1) preferentially populates the v' = 0 level of the $B^2\Sigma$ state, the nitrogen steady state concentration at the turning point of the relative intensity curve can be interpreted in terms of the rate constant for the reaction according to the expression,

$$k_a = \frac{1}{\tau[N_2]_{max}} \; cm^3 \; sec^{-1} \qquad (4.29)$$

For this method as well as the remaining reactions involving He^m, the experimental conditions of flow and reactant mixing gave an

effective emission source diameter of $d \sim 4.0$ cm. With a downstream pressure of 0.6 torr and an average velocity of 1.35×10^4 cm sec^{-1}, the nitrogen concentration corresponding to a maximum $I_{v'v''}$ in Fig. 5.1 was $[N_2]_{max} = 7.9 \times 10^{12}$ cm^{-3}. Substituting in Eq. (4.29) with a reaction distance, $\ell = 14$ cm, the measured rate constant k_a for reaction (5.1) was found to be $1.2 \pm 0.4 \times 10^{-10}$ cm^3 sec^{-1}.

A second method for obtaining the rate constant for reaction (5.1) depended upon the measurement of He^m concentration as a function of nitrogen flow by optical absorption of the HeI 3889Å transition. The rate constant was observed to have the value $9 \pm 3 \times 10^{-11}$ cm^3 sec^{-1}. Because of the short path length (~ 4 cm) and the overall sensitivity of the monochrometer and detection system, the optical absorption method appeared to be the least reliable of the three although the agreement is within the quoted uncertainities.

The third method similarly interprets the He^m concentration dependence on the nitrogen reactant flow rate in terms of the rate constant for the reaction. Observation of the metastable helium is indirectly made by measuring the emission intensity of a second reactant known to be primarly excited by He^m. This is the general method, as outlined in Section 4.3, for measuring the rates for the various reactants denoted by X. Both nitrogen and neon emission spectra excited by the metastable helium were used to observe the helium concentration, namely, the (0,3) band of the $B^2\Sigma - X^2\Sigma$

transition in N_2^+ and the NeI 6402.3Å transition. Unless otherwise specified, the relative intensity data reproduced in Figs. 5.2 thru 5.4 is for the nitrogen detector. The relative contribution of the He_2^+ in exciting these bands in question was reduced by operating at 0.4 torr downstream pressure and with a low power microwave field incident on the afterglow region for the purpose of preferentially increasing the He_2^+ ion removal by ambipolar diffusion to the walls. The curve in Fig. 5.2 for nitrogen as the primary reactant yields a slope whereby the rate constant can be calculated according to Eq. (4.38). The calculations yielded a constant of $1.1 \pm 0.4 \times 10^{-10}$ cm^3 sec^{-1} for the third measurement of the rate of reaction (5.1). Both the neon and nitrogen detection schemes at 0.4 torr downstream pressure and an effective source diameter of 4.0 cm gave values for the rate well within the estimated errors.

It is the purpose of the following discussion to report the rate constants for the reactants other than nitrogen. Unless otherwise noted, the curves in Fig. 5.2 to 5.4 correspond to the conditions of 0.4 torr pressure, source diameter of $d \sim 4.0$ cm and a low power ($\sim$ 10 watt) microwave field applied to the afterglow region. The remaining Penning ionization rate constants measured are included in Table 5.1. Values for the rates reported by other authors have been added for a direct comparison. By considering the reactants as mixture of two gases, in thermal equilibrium, the rate constant can be expressed in terms of a cross section, σ,[1]

$$k = \bar{u}_r \sigma \tag{5.2}$$

where $\bar{u}_r$ is the mean relative velocity of the two reactants with a value of 1.3×10^5 cm/sec for He and N_2 at 300°K.

In Table 5.1, the rate constants and cross sections observed in the present work are listed in the second and third columns with the estimated uncertainities. In every reaction except a single instance for reactant Kr, the reproducibility in the measurements was better than 10%. Due to some question about the magnitude of the systematic errors introduced in the flow measurements and velocity determination, the quoted errors for the rates have been chosen to be significantly larger than the observed 10%. Rate constants measured by other authors are included in the fourth column for comparison. The good overall agreement indicates the soundness of the present method. In the next column, the particular method used in the measurements are indicated according to the following: FA - flowing afterglow; PD - pulsed discharge; AB - atomic beam; DE - direct emission method outlined in Sec. 5.2; SE - secondary emission method outlined in Sec. 4.3; OA - optical absorption; and LPMS - low pressure mass spectrometer.

A discussion of these reactions in terms of available energy and energy resonances has little meaning since the free electron in the product can carry off excess energy of the reaction. This has been observed in reaction (5.1) where the N_2^+ product was found to be populated according to the Franck-Condon principle and not direct energy resonance[2].

5.2 Reactions with He^+

To measure the charge transfer type reactions of He^+ with the added reactant, of the type,

$$He^+ + X \rightarrow He + X^+ \qquad (5.3)$$

the (1,0) band of the $A^2\Pi$ - $X^2\Sigma$ transition in CO^+ upon addition of CO_2 as well as the already present HeI 5875.6Å emission was observed and interpreted in terms of the relative concentration of He^+. Figures 5.5 and 5.6 give the relative intensity of the emission as a function of reactant concentration for the CO^+ and HeI detector respectively. The curves correspond to measurements taken at a downstream pressure of 0.6 torr. The effective source diameter was measured to be 4.0 cm and 5.9 cm for the CO^+ and HeI emission, respectively. As in the case of the He^m reactions, the measurements performed in this section were checked under different experimental conditions. The reproducibility of the present data agreed within ± 10%. The calculation of a rate constant from the slope of the curves were made according to Eq. (4.45) which is algebraically identical to that for He^m reactions, Eq. (4.38). Table 5.2 contains the measured rate constants as well as values published by other authors.

No reactions involving argon and hydrogen reactants were observed with He^+. Consequently for the present experimental conditions, only an upper limit to the rate constant can be given, being $< 10^{-13}$ cm^3 sec^{-1}. The remaining values measured are listed in the

second column with errors estimated to be approximately ± 30%. Again the data presented by other authors is included in the third column where the comparison is very good in all reactants except CO_2 which still agrees within a factor of two. The interesting aspect of the charge transfer reactions with the first four reactants is their relatively large rate constants which are comparable to the orbiting collision rate constant calculated from the expression[1],

$$k_c = 2e\pi\left(\frac{\alpha}{\mu}\right)^{\frac{1}{2}} \tag{5.4}$$

where α is the polarizability of the neutral reactant, and μ is reduced mass. In addition to the measured rate constants quoted in Table 5.2 for comparison, Ferguson, et.al. have compared the available experimental data with the various theoretical models for the low energy ion-molecule reactions[3,4].

5.3 Reactions with He_2^+

The following section is concerned with measuring the absolute rate constants for the reactions of the type,

$$He_2^+ + X \rightarrow 2He + X^+ \tag{5.5}$$

In reactions involving charge transfer with He_2^+, the He_2 molecular emission and the (4,6) band of the $B^2\Sigma - X^2\Sigma$ transition of N_2^+ upon addition of N_2 were observed and interpreted in terms of the relative concentration of He_2^+. The rate constants were calculated from the slopes of the curves in Figs. 5.7 thru 5.11 by the method developed in Section 4.3. Fig. 5.7 gives the relative emission intensity of the $4^3\Delta - 2^3\Pi$ transition of He_2 at 5730Å as a function

of reactant concentration at a pressure of 0.6 torr and an effective source diameter of 5.9 cm. The remaining curves for He_2^+ reactions in Figs. 5.8 thru 5.11 indicate the relative intensity dependence of the (4,6) band of the $B^2\Sigma - X^2\Sigma$ transition for N_2^+ at a pressure of 0.6 torr and an effective source diameter of 4.0 cm. The charge transfer reaction with hydrogen reactant yielded a nonlinear emission intensity curve as seen in Fig. 5.11. This anomalous behavior is most likely due to the presence of overlapping unidentified bands in the He_2 and N_2^+ spectrum upon the addition of hydrogen to the afterglow.

In Table 5.3 absolute reaction rate constants for the reaction (5.5) are listed in the second column. The only value for comparison reported by another author is indicated in the third column for nitrogen reactant where the agreement is within the estimated uncertainities. Again the reproducibility of the measured rates for a variety of experimental conditions including the comparison of the two "detectors" agreed within ± 10%. The overall uncertainity was quoted to be approximately ± 30%.

5.4 Reactions with He_2^m

The remaining section is devoted to the measurement of reaction rates involving the metastable helium molecule, He_2^m,

$$He_2^m + X \rightarrow 2He + X^+ + e \qquad (5.6)$$

The relative concentration of He_2^m as a function of reactant flow rate was measured by observing the (2,0) band intensity of the $A^2\Pi - X^2\Sigma$ transition in N_2^+ as a function of reactant flow rate

indicated in Figs. 5.12 and 5.13. The rate constants for reaction (5.6) were calculated from the slopes of the observed intensity curves according to Eq. (4.49). The measured rate constants with estimated uncertainities of ± 30% are listed in the second column in Table 5.4. No known measurements for the rates of reactions with He_2^m have been found in the literature.

It is of interest to note the similarity between the rate constants for a particular reactant with He_2^+ and He_2^m. This could possibly be due to a poor choice of the $A^2\Pi$ - $X^2\Sigma$ system of N_2^+ for the He_2^m concentration measurements. On the other hand, the arguments in Section 3.4 give confidence to the choice of excited-state products used for detecting the energetic helium. A natural extension of this method would be to investigate excited-state products producing emission of other reactants for detectors which would isolate the different energetic helium reactions.

TABLE 5.1

He^m Thermal Energy Penning Ionization Reactions

Reactant	$k \times 10^{10}$, $cm^3\ sec^{-1}$	σ, $Å^2$	Method	Ref
N_2	1.1 ± 0.4	8.0 ± 3	FA/SE	
	0.9 ± 0.3	6.5 ± 2.5	FA/OA	
	1.2 ± 0.4	9.0 ± 3	FA/DE	
		7.0	AB	5
		6.4	PD/OA	6
		6.1		7
O_2	4.3 ± 1.3	32 ± 14	FA/SE	
		14	AB	5
H_2	0.55 ± 0.2	2.5 ± 0.9	FA/SE	
		2.6	AB	5
		2.4		8
		1.7		7
		6.1	PD/OA	6
Kr	1.3 ± 0.4	10 ± [illegible]	FA/SE	
		9.0	AB	5
		10.3	PD/OA	6
		16.5		7
Ar	1.3 ± 0.4	10 ± 3	FA/SE	
		7.6	AB	5
		6.6	PD/OA	6
CO	2.9 ± 0.9	21 ± 7	FA/SE	
		7	AB	5
NO	6.3 ± 1.9	47 ± 14	FA/SE	
CO_2	7.7 ± 2.3	59 ± 17	FA/SE	

TABLE 5.2

He^+ Thermal Energy Ion-Molecule Reactions

Reactant	$k \times 10^{10} (cm^3\ sec^{-1})$		σ Å^2		Method	Ref
N_2	15 ± 5		115	35	FA/SE	
		17 +2, -8	~ 130		FA/MS	3
		14.5			SA	9
		16.9			LPMS	10
O_2	14 ± 4		100	35	FA/SE	
		15 +2, -7	~ 115		FA/MS	3
		10.5			SA	9
		.5			SA	11
		17.0			LPMS	10
NO	24 ± 7		175	50	FA/SE	
		15 +2, -7	~ 115		FA/MS	3
		20.7			LPMS	10
CO_2	21 ± 6		155	45	FA/SE	
		12 +2, -6	~ 90		FA/MS	3
Ar	$< 10^{-3}$		$< 10^{-2}$		FA/SE	
		$< 10^{-3}$	$< 10^{-2}$		FA/MS	3
H_2	$< 10^{-3}$		$< 10^{-2}$		FA/SE	
		$< 10^{-3}$	$< 10^{-2}$		FA/MS	3

TABLE 5.3

He_2^+ Thermal Energy Molecular Ion-Molecule Reactions

Reactant	$k \times 10^{10}$, $cm^3\ sec^{-1}$	σ, $Å^2$	Method	Ref
N_2	9.5 ± 3	95 ± 30	FA/SE	
	60	60	FA/MS	3
O_2	15 ± 5	150 ± 50	FA/SE	
NO	23 ± 7	230 ± 70	FA/SE	
CO	36 ± 10	360 ±100	FA/SE	
Kr	1.6 ± .5	17 ± 5	FA/SE	
Ar	.02 ± .006	~ .2	FA/SE	
H_2	No interpretable rate constant			

TABLE 5.4

He_2^m Thermal Energy Molecule-Molecule Reactions

Reactant	$k \times 10^{10}$, $cm^3\ sec^{-1}$	σ, $Å^2$	Method
O_2	15 ± 5	150 ± 50	FA/SE
CO_2	16 ± 5	160 ± 50	FA/SE
NO	22 ± 7	220 ± 70	FA/SE
H_2	0.25 ± .08	1 ± .5	FA/SE
Kr	1.4 ± 0.4	15 ± 4	FA/SE
Ar	10^{-3}	10^{-2}	FA/SE

V REFERENCES

1. Hasted, J. B., Physics of Atomic Collisions, Butterworth and Co., Washington (1964), p. 12.
2. Robertson, W. W., J. Chem. Phys. 44, 2456 (1966).
3. Fehsenfeld, F. C., Schmeltekopf, A. L., Goldan, P. D., Schiff, H. I , and Ferguson, E. E., J. Chem. Phys., 44 4087 (1966).
4. Ferguson, E. E., Fehsenfeld, F. C., and Schmeltekopf, A. L., to be published.
5. Sholette, W. P. and Muschlitz, E. E., Jr., J. Chem. Phys. 36, 3368 (1962).
6. Benton, E. E., Ferguson, E. E., Matsen, F. A., and Robertson, W. W., Phys. Rev., 128, 206 (1962).
7. Jesse, W. P. and Sadauskis, J., Phys. Rev., 88, 417 (1952).
8. Schut, T. B. and Smit, J. A., Physica (Eindhoven) 10, 440 440 (1943).
9. Sayers, J. and Smith D., Dis. Far. Soc., 37, 167 (1964).
10. Friedman, L. and Moran, T. F., J. Chem. Phys., 42, 2624 (1965).
11. Fite, W. L., Smith A. C. H., Stebbings, R. F , and Rutherford, J. A., J. Geophys. Res , 68, 3225 (1963).

V Figure Legend

5.1 Relative intensity of the (0,1) band of the $B\,^2\Sigma - X\,^2\Sigma$ system of N_2^+ as a function of N_2 flow rate.

5.2 Loss of He^m shown by the relative decrease of the (0,3) band intensity of the $B^2\Sigma - X^2\Sigma$ transition of N_2^+ plotted as a function of the reactant flow rate.

5.3 Loss of He^m shown by the relative decrease of the (0,3) band intensity of the $B^2\Sigma - X^2\Sigma$ transition of N_2^+ plotted as a function of the reactant flow rate.

5.4 Loss of He^m shown by the relative decrease of the (0,3) band intensity of the $B^2\Sigma - X^2\Sigma$ transition of N_2^+ plotted as a function of the reactant flow rate.

5.5 Loss of He^+ shown by the relative decrease of the (1,0) band intensity of the $A^2\Pi - X^2\Sigma$ transition of CO^+ plotted as a function of the reactant flow rate.

5.6 Loss of He^+ shown by the relative decrease of the HeI line intensity at 5875.6Å plotted as a function of the reactant flow rate.

5.7 Loss of He_2^+ shown by the relative decrease of the (0,0) band intensity of the $4\,^3\Delta - 2\,^3\Pi$ transition of He_2 plotted as a function of the reactant flow rate.

5.8 Loss of He_2^+ shown by the relative decrease of the (4,6) band intensity of the $B^2\Sigma$ - $X^2\Sigma$ system of N_2^+ plotted as a function of the reactant flow rate.

5.9 Loss of He_2^+ shown by the relative decrease of the (4,6) band intensity of the $B^2\Sigma$ - $X^2\Sigma$ system of N_2^+ plotted as a function of the reactant flow rate.

5.10 Loss of He_2^+ shown by the relative decrease of the (4,6) band intensity of the $B^2\Sigma$ - $X^2\Sigma$ system of N_2^+ plotted as a function of the reactant flow rate.

5.11 Loss of He_2^+ shown by the relative decrease of the (4,6) band intensity of the $B^2\Sigma$ - $X^2\Sigma$ system of N_2^+ plotted as a function of the reactant flow rate.

5.12 Loss of He_2^m shown by the relative decrease of the (2,0) band intensity of the $A^2\Pi$ - $X^2\Sigma$ transition of N_2^+ plotted as a function of the reactant flow rate.

5.13 Loss of He_2^m shown by the relative decrease of the (2,0) band intensity of the $A^2\Pi$ - $X^2\Sigma$ transition of N_2^+ plotted as a function of the reactant flow rate.

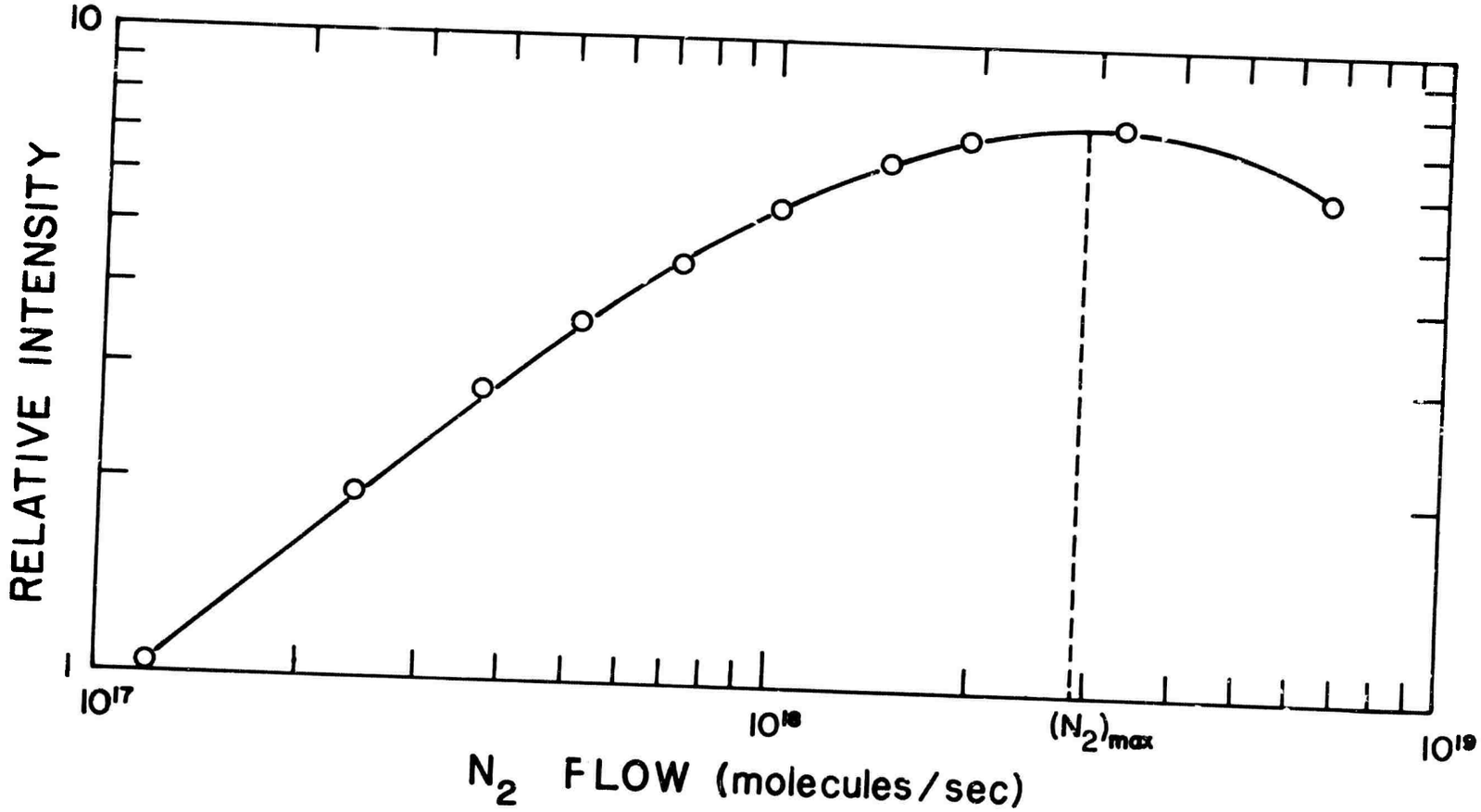
10
1
RELATIVE INTENSITY
10^{17}
10^{18}
$(N_2)_{max}$
10^{19}
N_2 FLOW (molecules/sec)

FIG 5.1

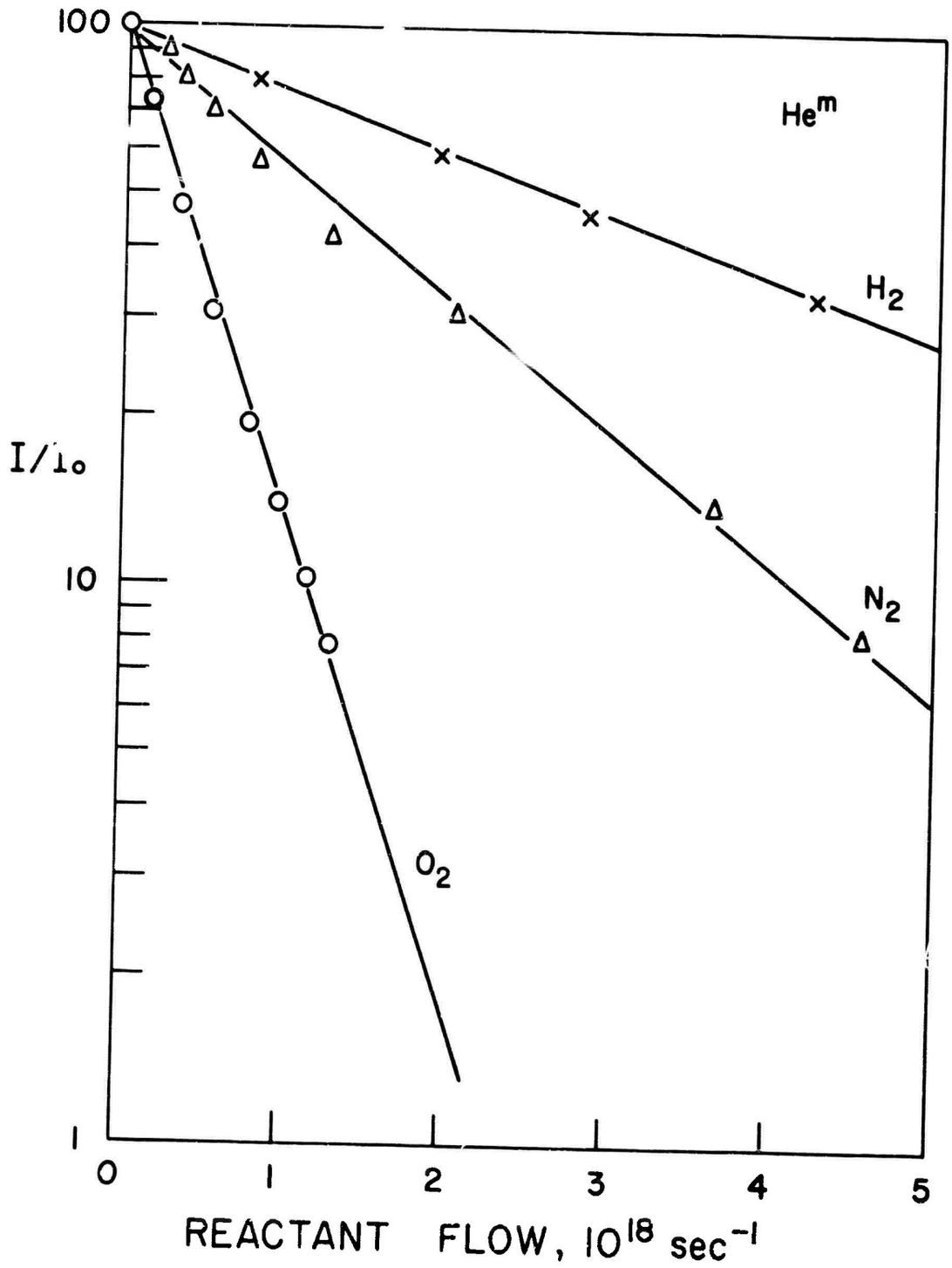

FIG 5.2

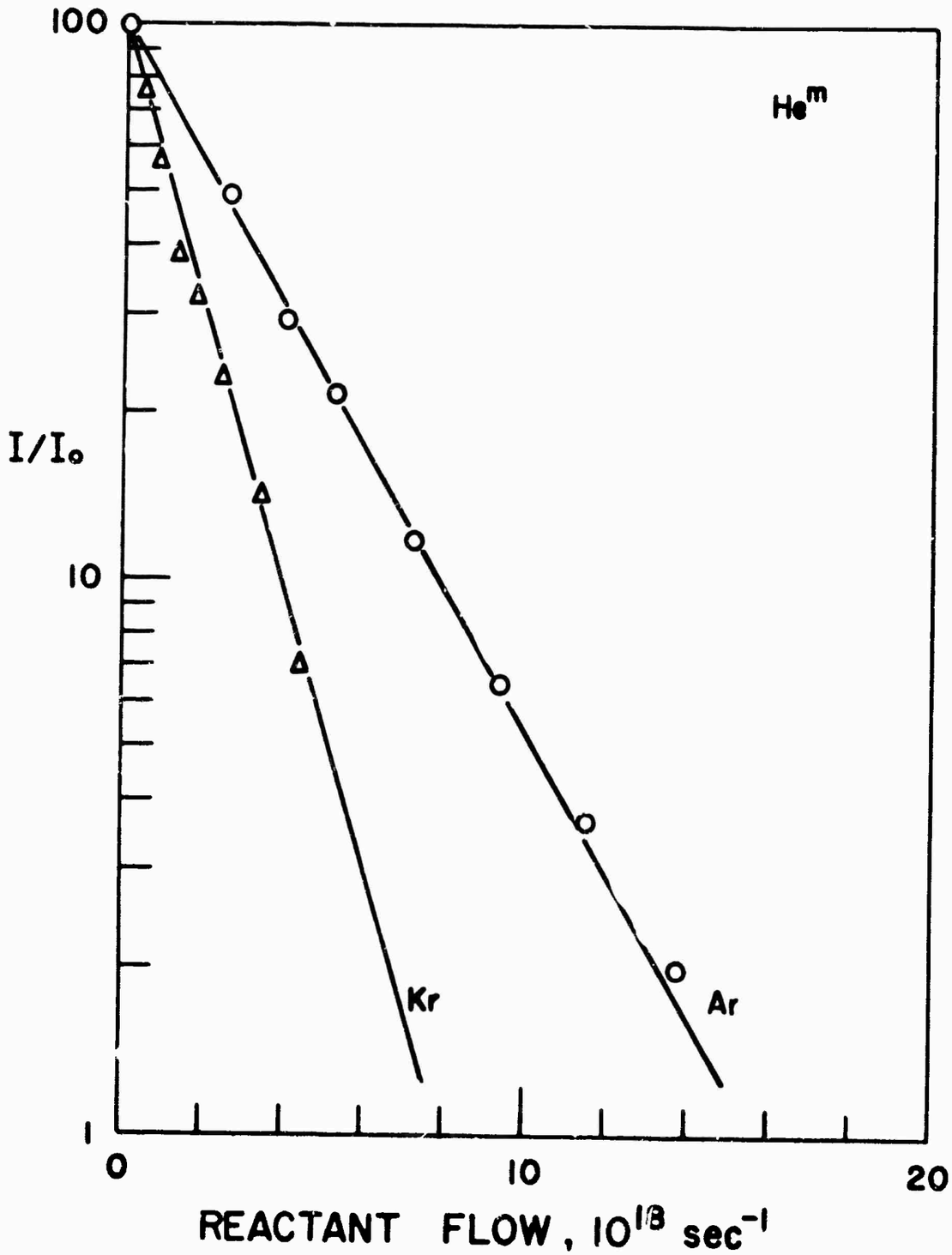

FIG 5.3

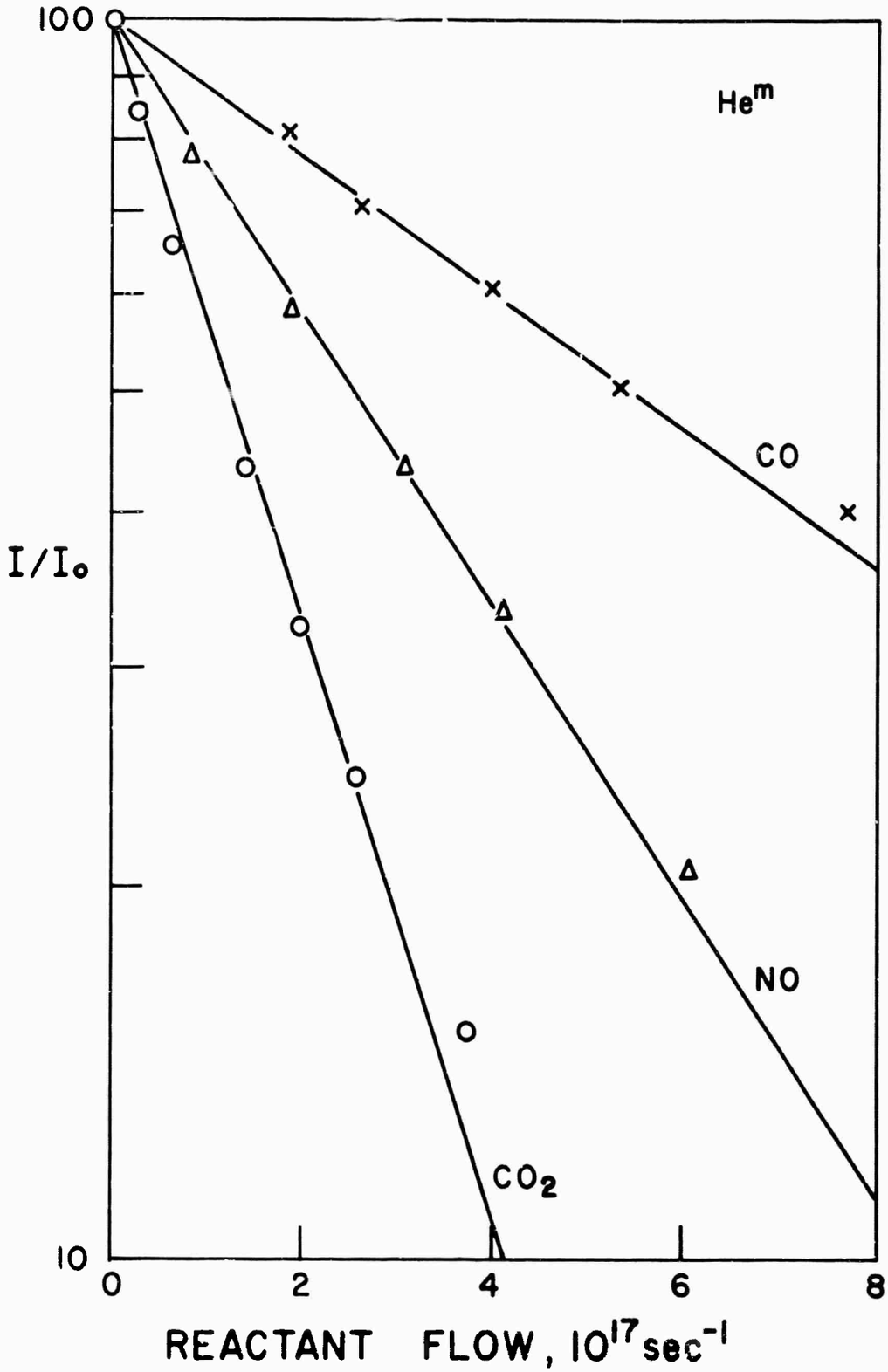

FIG 5.4

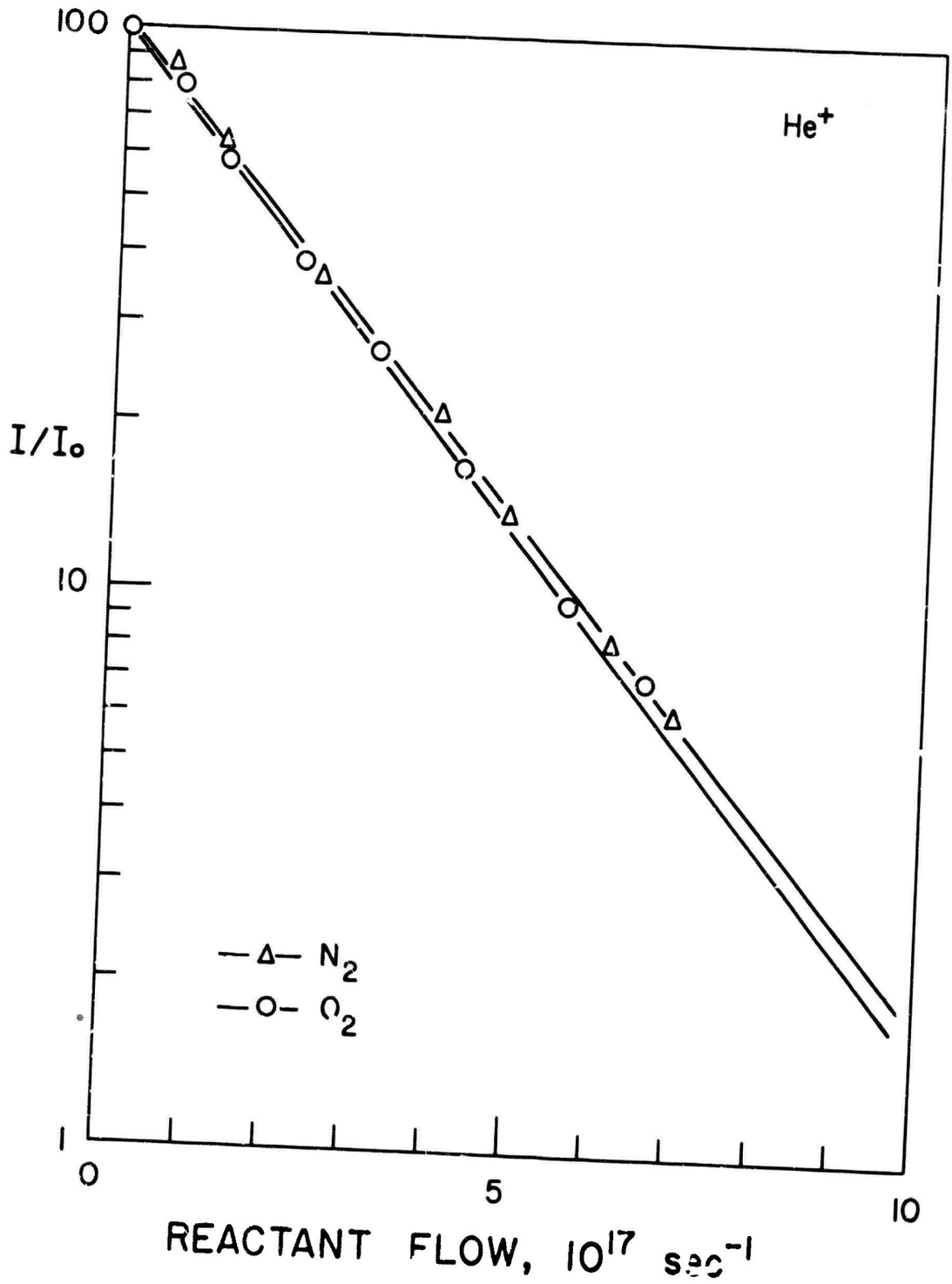

FIG 5.5

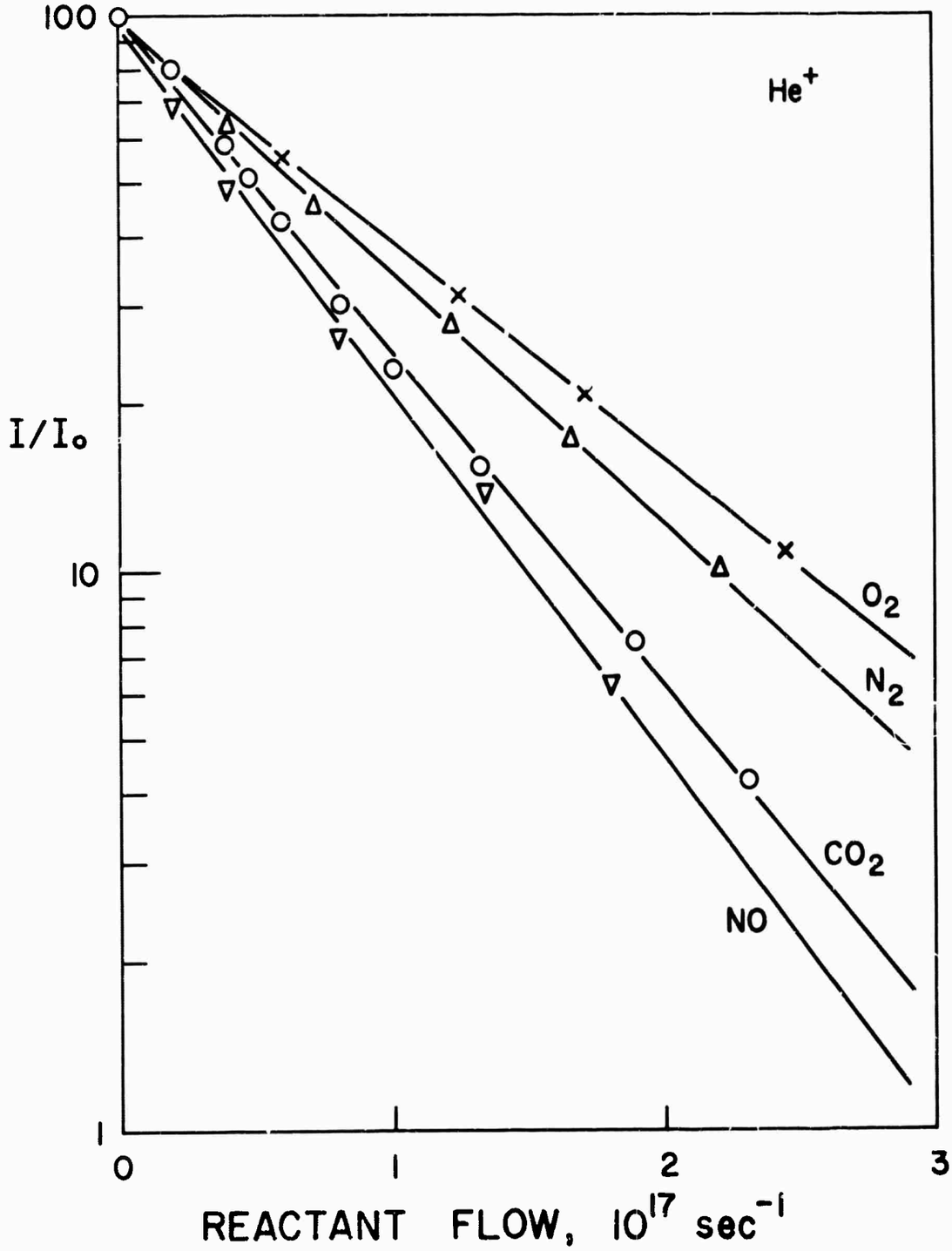

FIG 5.6

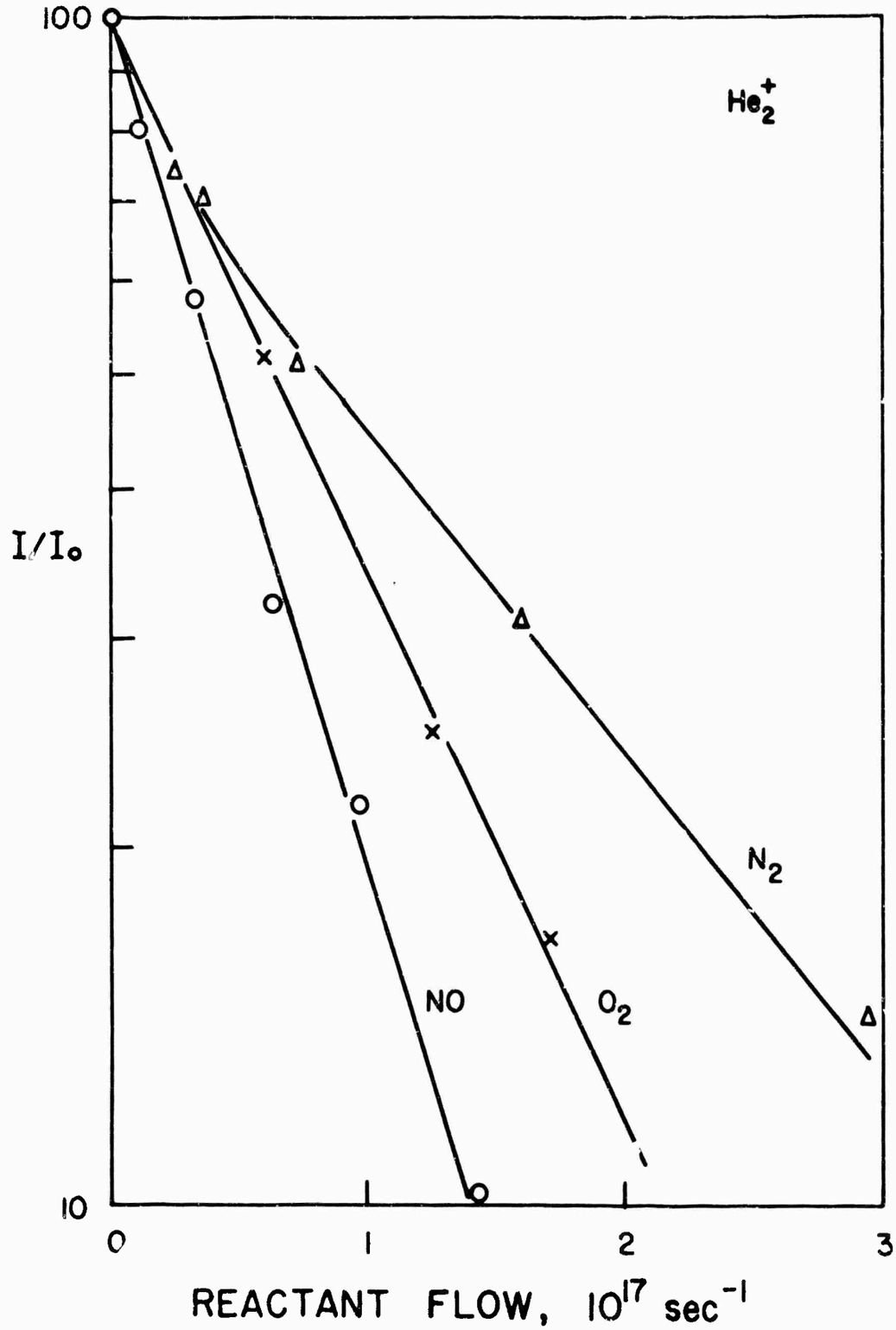

FIG 5.7

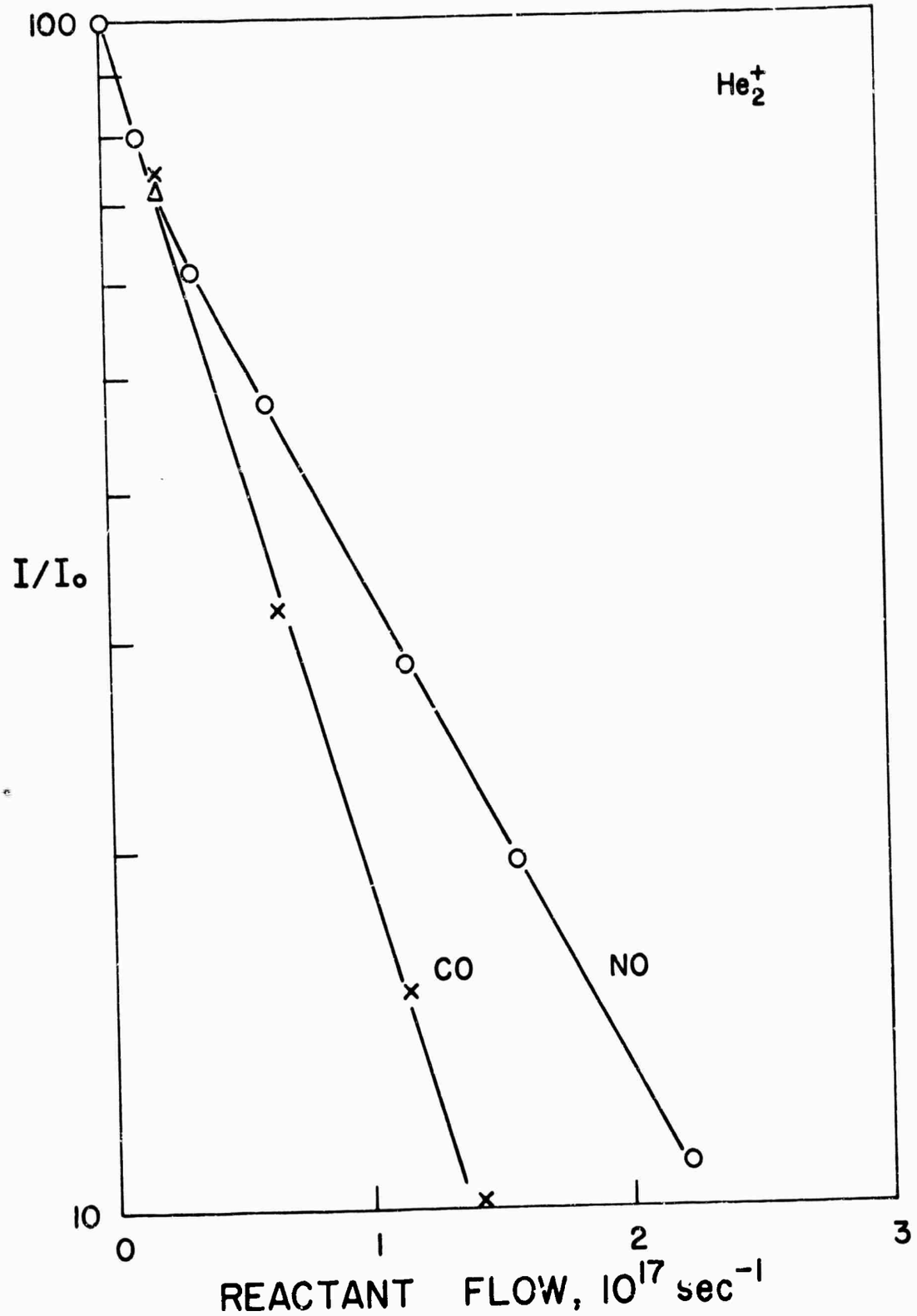

FIG 5.8

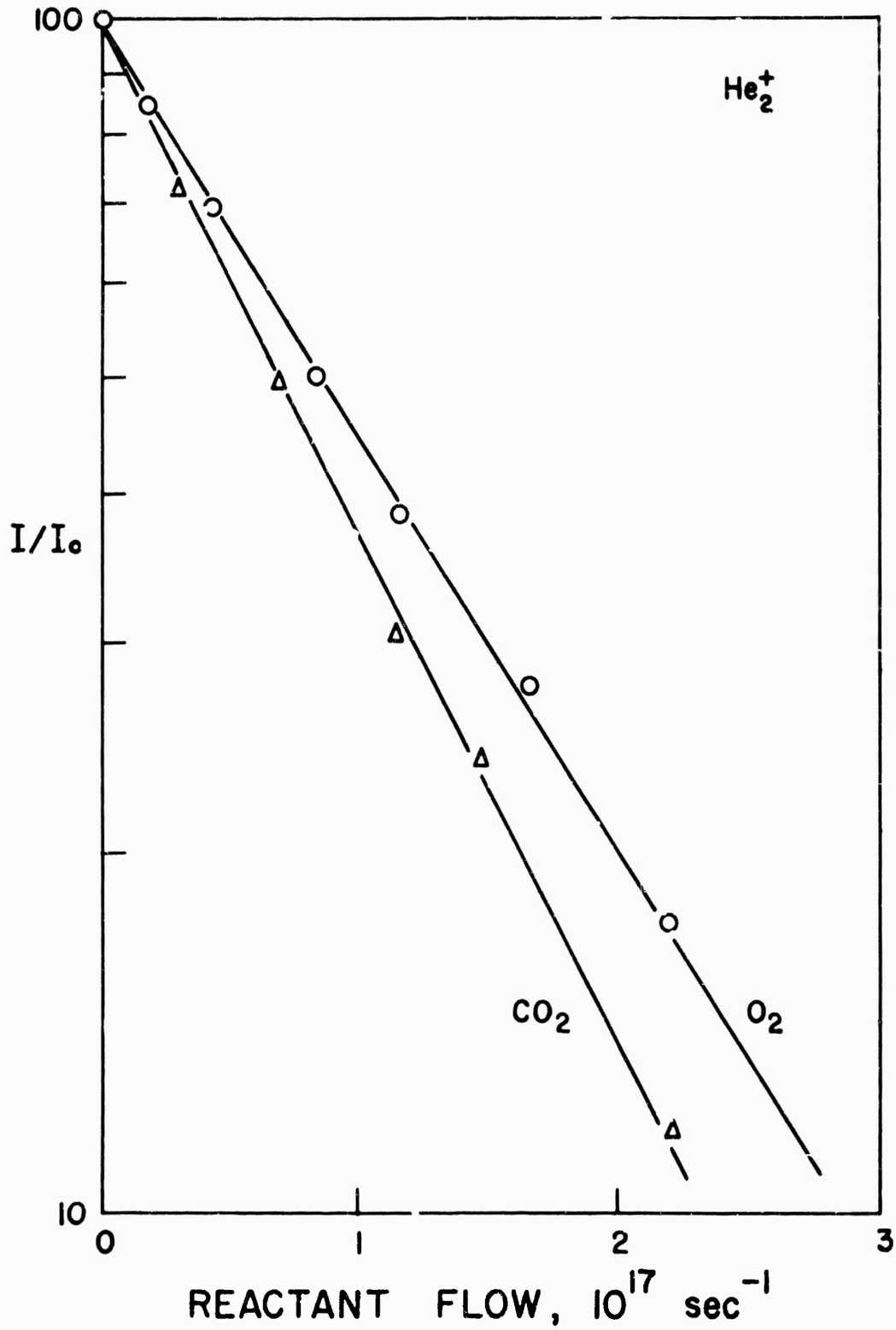

FIG 5.9

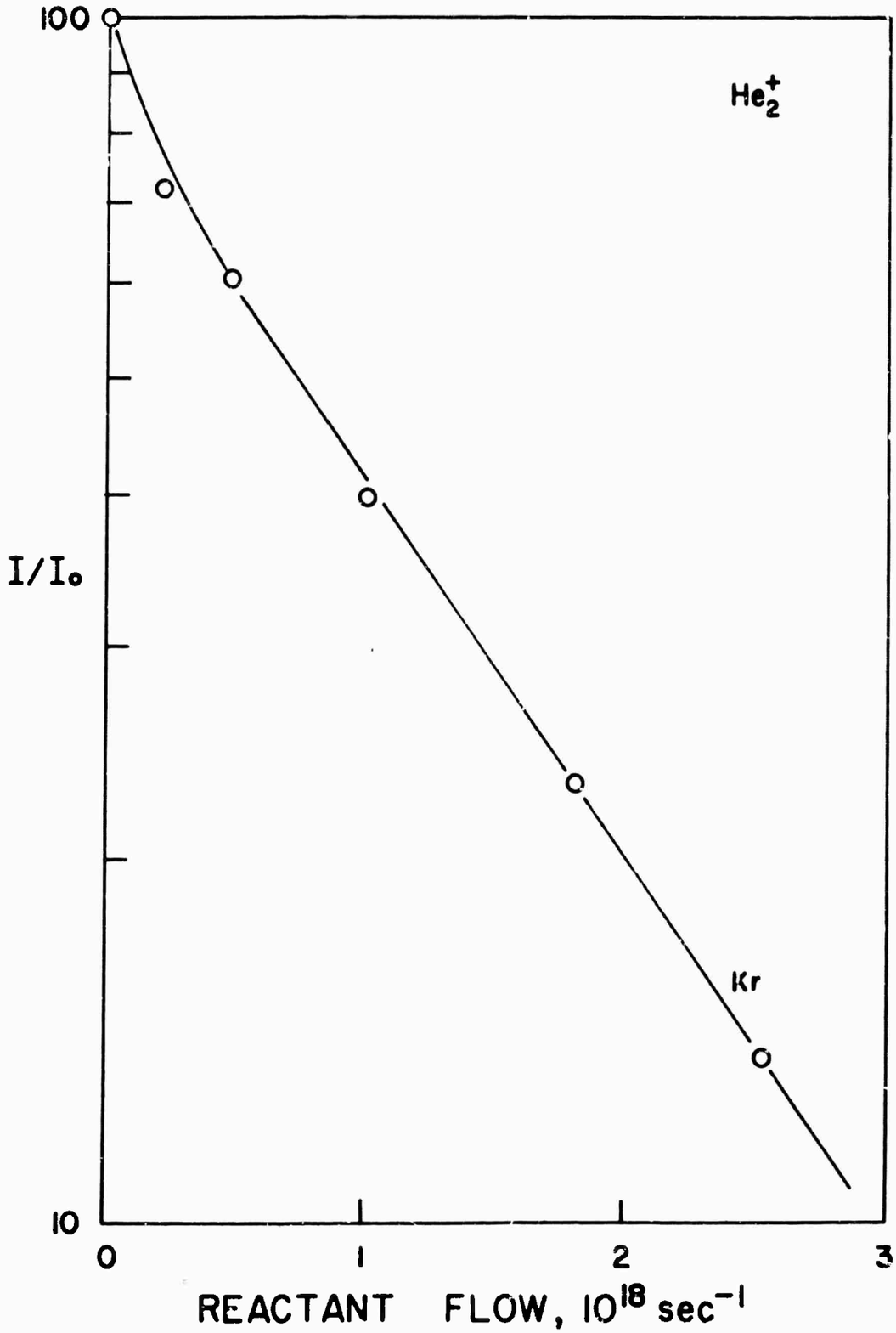

FIG 5.10

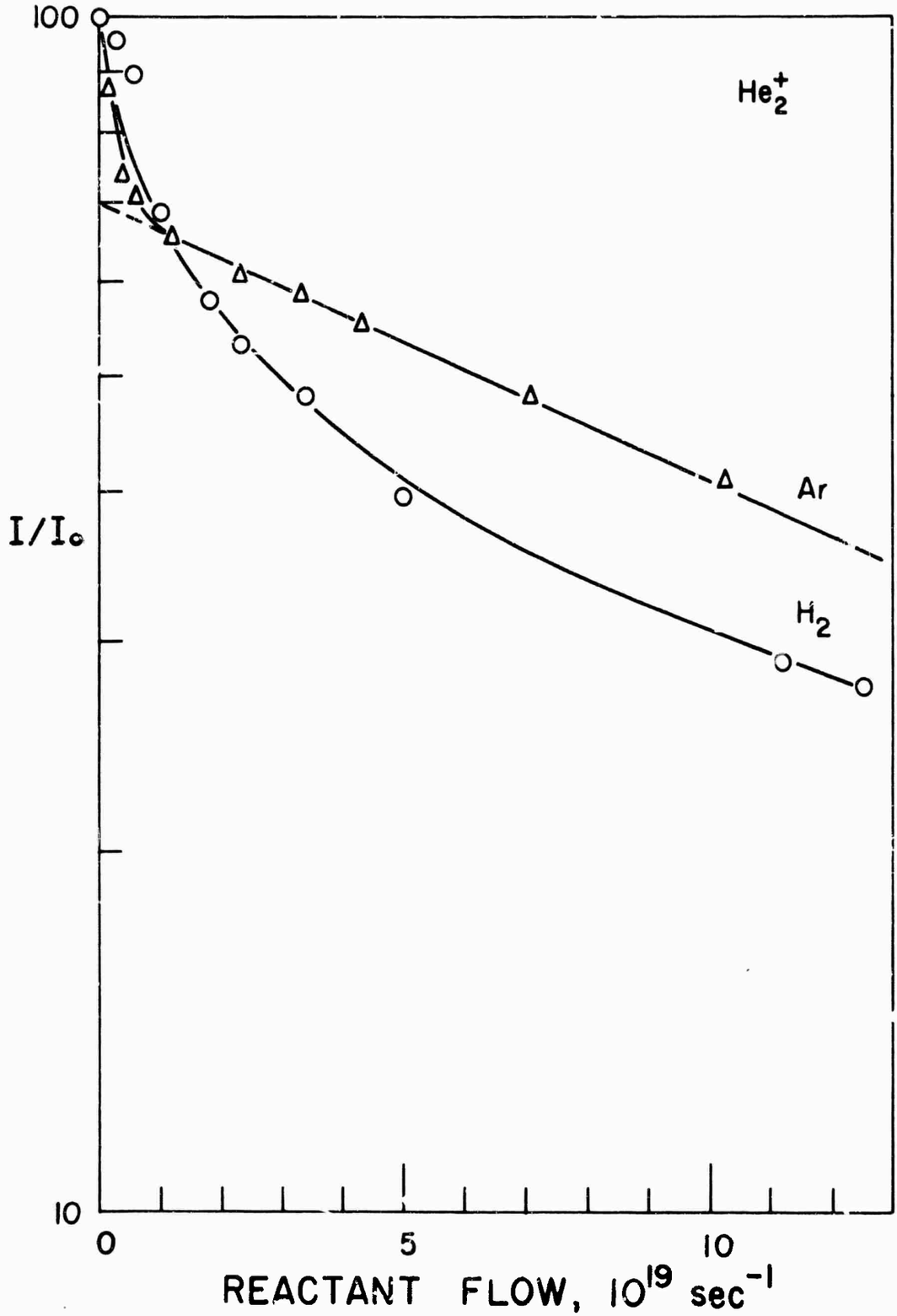

FIG 5.11

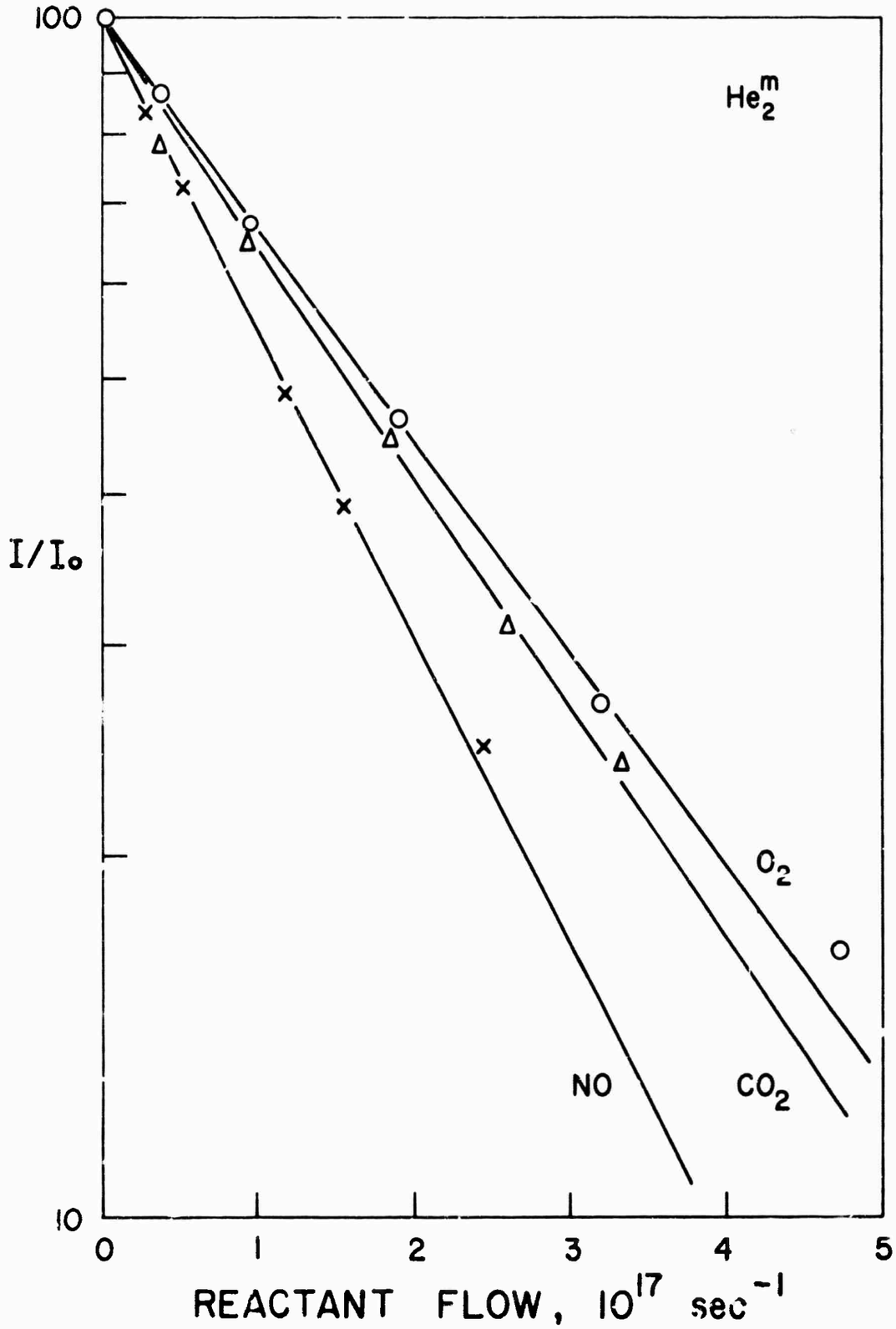

FIG 5.12

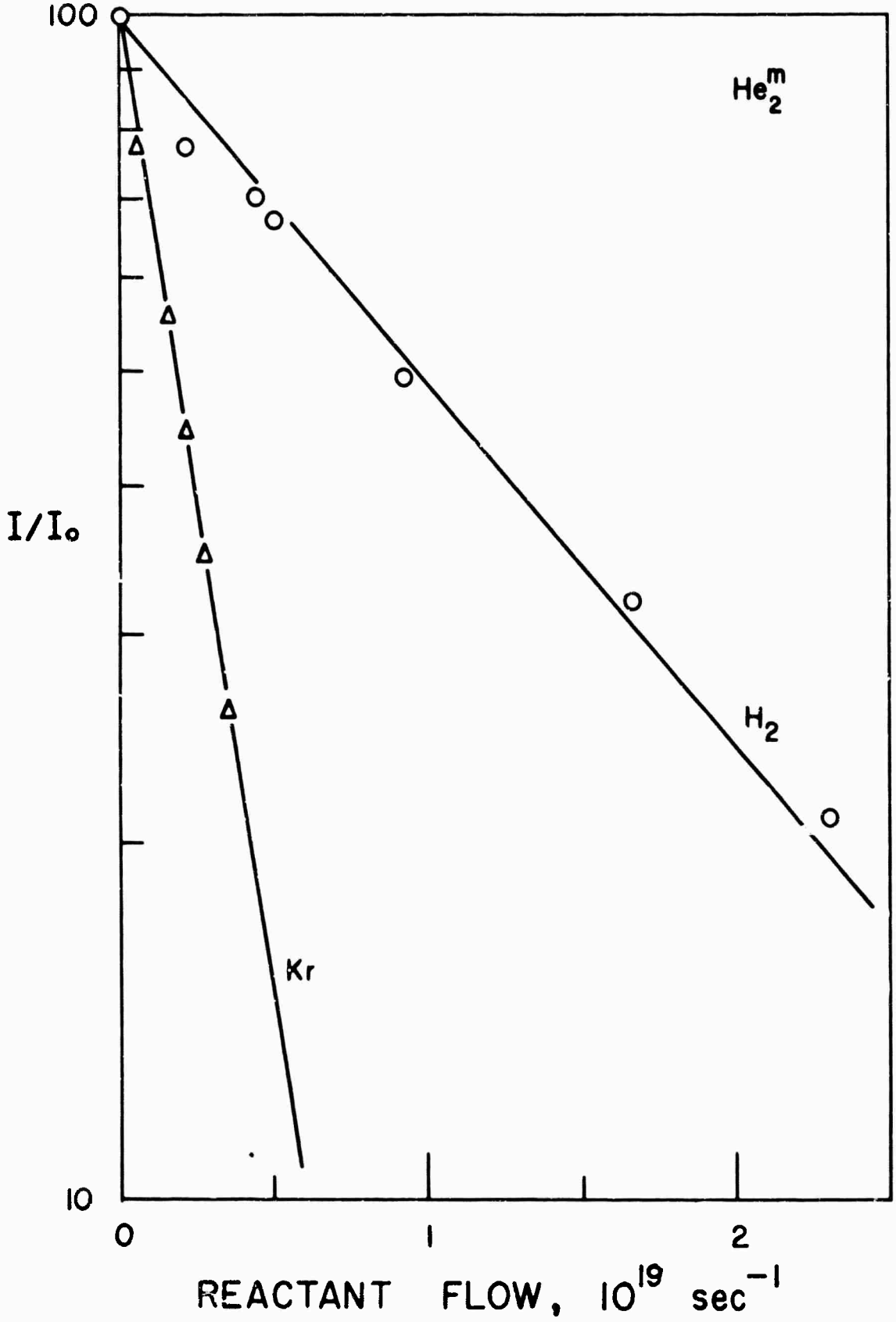

FIG 5.13